Centre for Catalysis Research

Department of Chemical Engineering

University of Cape Town

Platinum Nanoparticles to Study Metal Location in Shape-Selective Hydrocracking

Author: Dayle Nel

Supervisors: Dr. Roald Brosius, Prof. Patricia Kooyman and Prof. Jack Fletcher

Submitted in partial fulfilment of the requirements of the degree of Master of Science in Chemical Engineering

December 2017

PLAGIARISM DECLARATION

I know the meaning of plagiarism and declare that all the work in the document, save for that which is properly acknowledged, is my own. This thesis/dissertation has been submitted to the Turnitin module (or equivalent similarity and originality checking software) and I confirm that my supervisor has seen my report and any concerns revealed by such have been resolved with my supervisor.

Name: Dayle Nel

Date: December 2017

Signature: Signed by candidate

ETHICS CLEARANCE

Application for Approval of Ethics in Research (EiR) Projects
Faculty of Engineering and the Built Environment, University of Cape Town

APPLICATION FORM

Please Note:
Any person planning to undertake research in the Faculty of Engineering and the Built Environment (EBE) at the University of Cape Town is required to complete this form **before** collecting or analysing data.The objective of submitting this application *prior* to embarking on research is to ensure that the highest ethical standards in research, conducted under the auspices of the EBE Faculty, are met. Please ensure that you have read, and understood the **EBE Ethics in Research Handbook**(available from the UCT EBE, Research Ethics website) prior to completing this application form: http://www.ebe.uct.ac.za/usr/ebe/research/ethics.pdf

APPLICANT'S DETAILS		
Name of principal researcher, student or external applicant		Dayle Nel
Department		Engineering and the Built Environment
Preferred email address of applicant:		nlxday001@myuct.ac.za
If a Student	Your Degree: e.g., MSc, PhD, etc.,	MSc
	Name of Supervisor (if supervised):	Dr. Roald Brosius
If this is a researchcontract, indicate the source of funding/sponsorship		c*change (DST/NRF Centre of Excellence in Catalysis)
Project Title		Platinum Nanoparticle Synthesis on MFI Nanosheets for Hexadecane Hydrocracking

I hereby undertake to carry out my research in such a way that:

- there is no apparent legal objection to the nature or the method of research; and
- the research will not compromise staff or students or the other responsibilities of the University;
- the stated objective will be achieved, and the findings will have a high degree of validity;
- limitations and alternative interpretations will be considered;
- the findings could be subject to peer review and publicly available; and
- I will comply with the conventions of copyright and avoid any practice that would constitute plagiarism.

SIGNED BY	Full name	Signature	Date
Principal Researcher/ Student/External applicant	Dayle Nel	Signed by candidate	**07 Sep 2016**

APPLICATION APPROVED BY	Full name	Signature	Date
Supervisor (where applicable)	Dr. Roald Brosius		**07 Sep 2016**
HOD (or delegated nominee) Final authority for all applicants who have answered NO to all questions in Section1; and for all Undergraduateresearch (Including Honours).	J. Peters ~~Click here to enter text.~~		7-9-2016 ~~Click here to enter a date.~~
Chair : Faculty EIR Committee For applicants other than undergraduate students who have answered YES to any of the above questions.	Click here to enter text.		Click here to enter a date.

Page **1** of **1**

ACKNOWLEDGEMENTS

This work is based on the research supported by the DST-NRF Centre of Excellence in Catalysis (c*change) as well as in part by the National Research Foundation of South Africa (Grant number 94878).

I would like to acknowledge the following people and entities for their roles in the submission of this dissertation:

- Dr Roald Brosius for the continuous support and patience throughout my MSc. I hugely value the time and effort you invested in helping me become a better engineer and researcher. Thank you for always challenging me and having time to chat about hydrocracking, nanoparticles, and life.
- Prof Patricia Kooyman for keeping me going when times were tough - I would not have finished without your support and guidance and I will always be grateful to you for that. Secondly, a massive thank you for your training and assistance with the microscopy work.
- Prof J Fletcher for successfully sourcing funding to make this project a reality.
- The Department of Chemical Engineering and the Catalysis Research Centre at the University of Cape Town (UCT) for access to office and laboratory facilities.
- The UCT Analytics Laboratory for conducting ICP-OES characterisation and for their assistance and use of the CO chemisorption and NH_3-TPD facilities.
- The UCT Centre for Imaging Analysis for their assistance, training, and use of their facilities.
- The Centre for High Resolution Transmission Electron Microscopy, especially Dr. J.E. Olivier and Dr. J.H. O'Connell, at Nelson Mandela Metropolitan University in Port Elizabeth for their assistance and use of their facilities.
- Lastly, my friends, family and partner for their unwavering patience and support.

CONFERENCE CONTRIBUTIONS

2016

D. Nel, R. Brosius and P Kooyman and J Fletcher

"Using Platinum Nanoparticles to Investigate Nanoscale Intimacy in Primary Cracking of n-C_{16} over shape-selective MFI zeolites"

Oral presentation at the Annual c*change Workshop, Champagne Sports Resort, Drakensberg, South Africa

D. Nel, R. Brosius and P Kooyman and J Fletcher

"Using Platinum Nanoparticles to Investigate Nanoscale Intimacy in Primary Cracking of n-C_{16} over shape-selective MFI zeolites"

Oral presentation at the 27th Annual Conference of the Catalysis Society of South Africa (CATSA), Champagne Sports Resort, Drakensberg, South Africa

2017

D. Nel, R. Brosius, P Kooyman and J Fletcher

"Platinum Nanoparticles to study metal location in shape-selective hydrocracking"

Poster presentation at Catalysis for Fuels Faraday Discussion, Royal Society of Chemistry, Cape Town, South Africa

*This poster was presented with thanks to the CATSA 2017 travel award

ABSTRACT

In the petrochemical industry, bifunctional hydrocracking is used to further refine long chain hydrocarbon product molecules into smaller, more valuable fragments (such as diesel and aviation fuel). The current study is focused on using hydrocracking to increase diesel yield, as the preferred automotive fuel in terms of efficiency and environmental impact. However, even though conventional hydrocracking can significantly increase diesel yield, it is not selective to improving diesel quality. In a recent study by Brosius *et al.*, 2016, the use of a Pt/MFI bifunctional hydrocracking catalyst in the presence of H_2O has shown, for the first time, selective hydrocracking to produce not only a high yield but also high cetane number diesel product. The current study is a continuation of the work by Brosius *et al.*, 2016, with a focus on improving the catalyst design and, in particular, the metal function, as in this study the Pt metal was supported using wet impregnation which does not allow for control of metal size and location.

The hydrocracking mechanism consists of a (de)hydrogenation function at the metal sites and cracking/isomerisation steps at the acid sites. The reason a high yield of high cetane diesel is produced from hydrocracking over **Pt/MFI** in the presence of H_2O is twofold: firstly, hydrocracking inside the MFI micropores is selective to C-type β-scission which results in linear cracking products, and secondly, H_2O competes at the acid sites which allows for the desorption of the linear primary cracking products. From previous literature it is evident that metal location affects both activity and selectivity during hydrocracking over various catalyst types due to diffusion limitations. Furthermore, with hydrocracking over MFI, metal location is also expected to influence the amount of reactant molecules which crack inside the micropores. Therefore, the aim of this study was to quantify the extent that metal located inside or outside the micropores of MFI influences the cracking and isomerisation steps in the hydrocracking of n-C_{16} in the presence of H_2O.

Pt metal was selectively placed inside and outside the MFI micropores using different preparation techniques. To place the metal exclusively outside the micropores, monodisperse Pt NPs, which were bigger than the micropore diameter of 0.55 nm, were pre-synthesised and then contacted with the MFI support. To place the metal exclusively inside the micropores, a competitive ion exchange (CIE) method was used where Pt ions were chemically bonded within the MFI structure. Besides bulk MFI, the Pt NPs were also supported on MFI nanosheets (NS), which have been used in previous research to decrease diffusion limitations between metal and acid sites, to assess the effects of metal location. The prepared catalysts were characterised using TEM, ICP-OES, CO chemisorption, and NH_3-TPD to ensure metal location was the only varied parameter. The catalysts were then analysed by dry and wet hydrocracking of n-C_{16} in a fixed-bed, trickle reactor, where the product composition was determined using an online GC.

The performance of **PtNPs/MFI** and **Pt-CIE/MFI** were compared directly with **Pt/MFI** from Brosius *et al.*, 2016. Catalyst activity was first analysed using conversion versus temperature plots

and Arrhenius plots, primary hydrocracking was then assessed using C_4/C_{12} ratio and once achieved, branched versus linear product selectivity could be compared. Looking at activity, H_2O decreased the activity by ~30 °C, which is expected as H_2O blocks acid sites. Comparing the individual samples showed relatively similar results in wet and dry hydrocracking, showing metal location does not play a major role in overall activity. From the Arrhenius plots, the activation energies could be compared and showed that the difference between wet and dry hydrocracking was relatable to the isosteric heat of adsorption of H_2O on MFI. Primary hydrocracking was achieved for all three catalyst samples in the presence of H_2O, again showing that metal location does not largely influence the yield of primary cracking products. However, when comparing branched versus linear primary cracking products, a significant difference was observed based on metal location. At low conversion, the greatest differences are seen, with **Pt/MFI** and **Pt-CIE/MFI** achieving ~100 % n-alkanes in C_1-C_{15} cracked products, whereas PtNPs/MFI achieved only ~40 %. The reason for the vast differences is because having the metal inside the micropores, firstly, provides a non-diffusion hindered steady supply of reactant molecules to encourage desorption of the primary cracked products and, secondly, the cracking/isomerisation steps need to occur inside the MFI micropores which is more likely with internal metal. Furthermore, placing Pt NPs on NSs showed that even with thin NSs of 2 nm thickness, if the metal is placed outside, the hydrocracking products are just as branched as those from **PtNPs/MFI**. Post-mortem TEM characterisation of the catalyst samples revealed that no significant changes to the Pt metal sites were seen after ~10 days of reaction under varying hydrocracking conditions, ensuring that metal location was the only parameter varied in the study.

In conclusion, regardless of metal location, primary hydrocracking can be achieved in the presence of H_2O. Furthermore, placing metal exclusively inside the MFI micropores results in a significant increase in linear primary cracking products in comparison to placing metal completely outside the micropores, which results in mostly branched primary cracking products.

TABLE OF CONTENTS

LIST OF FIGURES

Chapter 1

Chapter 2

Chapter 4

Chapter 5

Chapter 6

Chapter 7

Appendix A

Appendix C

LIST OF TABLES

Chapter 2

Chapter 4

Chapter 5

Chapter 6

NOMENCLATURE

Abbreviations

AFS	Anderson-Flory-Schultz (polymerisation model)
CCD	Charge Coupled Device
CIE	Competitive Ion Exchange
EG	Ethylene Glycol
GC	Gas Chromatography
HAADF	High-Angle Annular Dark-Field
IE	Ion Exchange
IWI	Incipient Wetness Impregnation
LTFT	Low Temperature Fischer-Tropsch
NP	Nanoparticle
NS	Nanosheet
OA	Oleylamine
OMCVD	Organo-Metallic Chemical Vapour Deposition
PAMAM	Polyaminoamide
PNVIBA	Poly(N-vinylisobutyramide)
STEM-BF	Scanning Transmission Electron Microscopy – Bright Field
TEM	Transmission Electron Microscopy
TBR	Trickle Bed Reactor
TOF	Turn Over Frequency
TPD	Temperature Programmed Reduction
VGO	Vacuum gas oil

Chapter 1

Introduction

This thesis will attempt to quantify the effects of metal size and location in the hydrocracking of n-C_{16} over MFI zeolites in the presence of H_2O. This chapter will explain the context of how this research came about and then further define the problem being investigated within this context. The overall aim of the thesis will be stipulated along with the scope and limitations.

To provide some context to this work, hydrocracking denotes a stoichiometry in which one or more carbon-carbon bonds in a reactant (typically a hydrocarbon) are broken and the free valencies created are saturated with hydrogen. There are four distinct mechanisms by which hydrocracking can proceed, depending on the nature of the catalyst: bifunctional hydrocracking on a bifunctional catalyst (often with a metal and acid component), hydrogenolysis on a monodisperse metal catalyst, catalytic cracking on a monofunctional acidic catalyst, and thermal hydrocracking in the absence of a catalyst (Weitkamp, 2012).

Bifunctional hydrocracking is used in the petrochemical industry and is a highly flexible process that can be used to convert virtually any refinery stream into more valuable products – enabling refineries to respond efficiently to changes in market needs (Weitkamp, 2012). In the 1960s and 70s, the most common application for hydrocracking was to produce naptha for gasoline reforming. However, as the demand for gasoline has begun to level off and the demand for middle distillates (C_{10}-C_{20}) such as diesel and aviation fuel is increasing, the application for hydrocracking to maximise middle distillates has gained traction (Meyers, 2004). This is achieved by separating out the less valuable heavier fractions (C_{21+}) produced in crude oil refining or the Fischer-Tropsch process and sending them through a hydrocracking process which breaks down the long carbon chain fragments into smaller chains (Weitkamp, 2012).

An important application of bifunctional hydrocracking is its use in conjunction with the low temperature Fischer-Tropsch (LTFT) process, which will be the focus of this study. The main advantage of LTFT wax hydrocracking is that it is the only process which can produce diesel which is essentially free of S and N contaminants (Dry, 2002). In a LTFT process, syngas (which is a mixture of hydrogen and carbon monoxide) is converted to a range of different length hydrocarbons. However, regardless of the reactions or catalysts used, the Fischer-Tropsch reaction always produces a wide range of carbon numbers, as described by the Anderson-Flory-Schultz

(AFS) polymerisation model. The AFS model states that the carbon number distribution of the products is a function of chain growth probability at the surface of the catalyst (Bouchy *et al.*, 2009). Assuming ideal AFS kinetics, as seen in *Figure 1.1*, the maximum middle distillates yield (C_{10}-C_{20}) is only ~40 wt. % and there is still a large distribution of longer chain products. However, with the addition of a hydrocracking step a middle distillates yield of ~80 wt. % is actually achievable (Dry, 2002).

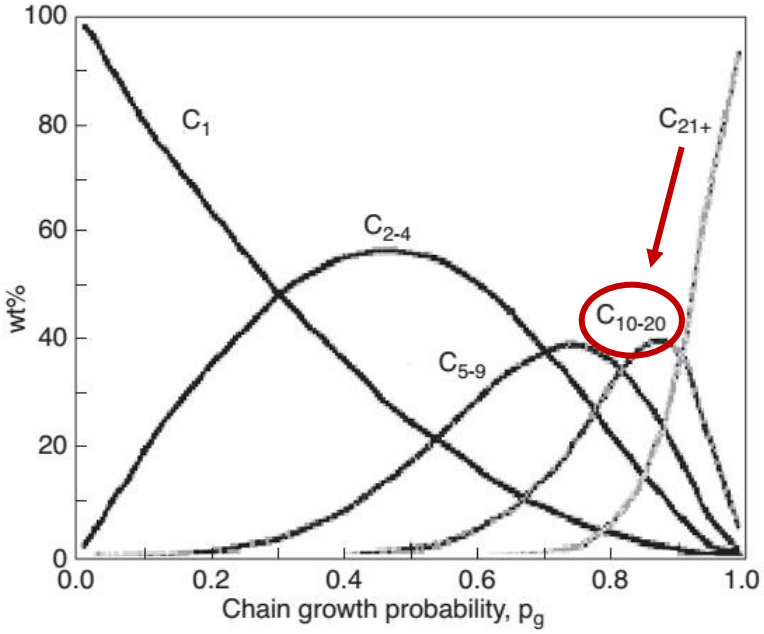

Figure 1.1: AFS model showing product composition of low temperature Fischer-Tropsch products against chain growth probability. Adapted from Bouchy et al., 2009.

This study is focused on the application of bifunctional hydrocracking to produce a high yield of diesel. Since, if synthetic automotive fuels are to be produced, diesel is the preferred option from an efficiency and environmental impact stand point. This is justified by the fact that the efficiency of a diesel-fuelled engine is higher than a gasoline-fuelled engine; meaning that more kilometres can be travelled per unit of diesel fuel. Furthermore, diesel fuel is further hydrogenated which when combusted produces relatively less CO_2 and more H_2O than gasoline fuel (Dry, 2002).

However, even though bifunctional hydrocracking can increase the yield of diesel significantly, it is not selective to improving diesel quality. There are three general methods which are used to reduce emissions from diesel fuelled internal combustion engines: alteration of the fuel, alteration of the combustion process, and exhaust after treatment (Dry, 2002). In this study, fuel alteration is pursued with a focus on increasing cetane number, since dramatic reductions in exhaust emissions are achieved via combustion of high cetane number diesel, as shown by a comparison of different diesel fuels by Lilik and Boehman, 2011:

Diesel fuel with a derived cetane number (DCN) of 51 was found to decrease total unburnt hydrocarbons (THC) and CO emissions by 32% and 31%, respectively, compared to a diesel fuel with a DCN of 45. Whereas, with a DCN of 81, an 80% reduction in THC emissions and a 74% reduction in CO emissions was seen in comparison to the DCN 45 fuel. In industry, diesel quality is currently improved through the hydrotreating of low cetane number molecules (such as

polyaromatics and napthalenes) to hydrogenated and ring-opened products. These molecules are then blended back into the conventional diesel stock to increase cetane number (Jacquin *et al.*, 2004).

In pursuit of a novel process to produce a high yield of high cetane diesel, Brosius *et al.*, 2016 showed for the first-time, primary hydrocracking (giving a high yield) and suppression of secondary isomerisation (allowing for high cetane number) over a shape selective MFI zeolite. It was shown in a study in the 80's, that the MFI zeolite has the unique ability to produce linear primary hydrocracking products, which is best interpreted in terms of a type C β-scission mechanism that occurs inside the pentasil channel system. The shape selective nature of the MFI could be hugely beneficial in selectively producing linear hydrocracking products but was not pursued in the past due to the unavoidable occurrence of secondary isomerisation and cracking steps (Weitkamp *et al.*, 1983). However, in the newly published work by Brosius *et al.*, 2016, H_2O is used to suppress secondary cracking allowing for primary cracking over MFI zeolites for the first time. The competitive adsorption of H_2O also facilitates the desorption of the primary cracking products to further prevent secondary isomerisation allowing for high yields of highly linear diesel.

This study will continue the research by Brosius *et al.*, 2016 using the existing process and catalyst design, with particular focus on the Pt metal component of the bifunctional catalyst. In *Figure 1.2*, TEM images show the Pt metal as the darker spots in *Figure 1.2* (a) and by the illuminated white areas in *Figure 1.2* (b).

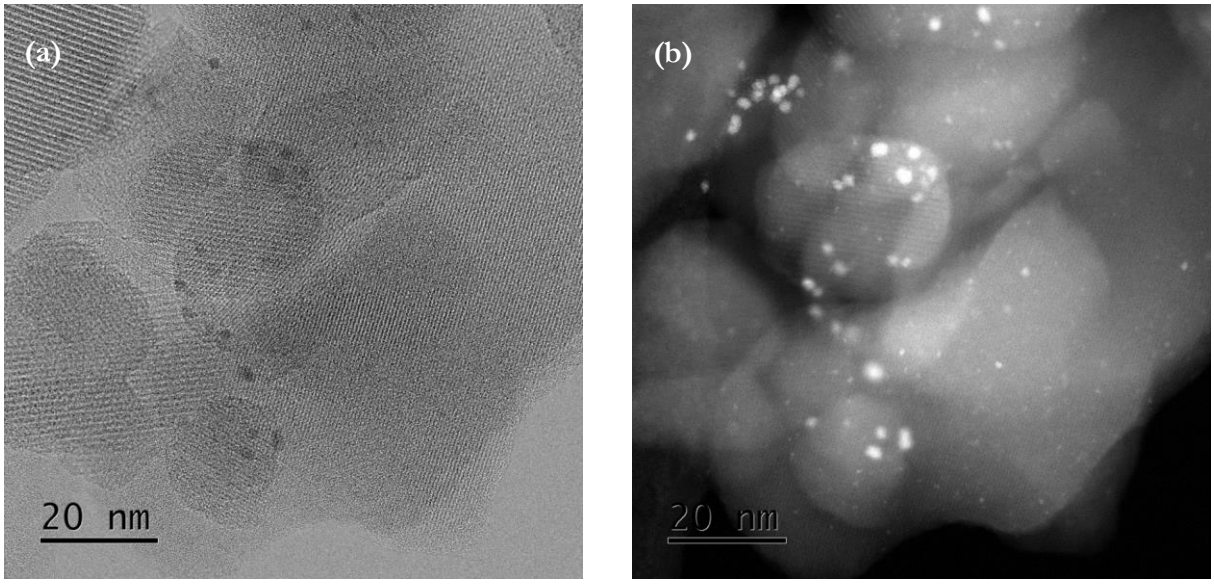

Figure 1.2: TEM images of Pt on MFI (a) BF-STEM mode and (b) HAADF-STEM mode

It is evident that the Pt NPs are varied in size with small clusters of Pt and then larger NPs up to 2-3 nm in diameter. This raises the first question which is: does the metal size play a role during the hydrocracking reactions? Furthermore, as the micropores of the MFI have a diameter of ~0.55 nm, the second question raised is related to metal location: is the metal inside or outside the micropores and does this matter in terms of activity or selectivity for the hydrocracking reactions?

The aim of the study is therefore to quantify the extent that metal size and location (inside or outside the micropores of MFI) influences the cracking and isomerisation steps in hydrocracking over **Pt/MFI** with H_2O. The study is limited to the hydrocracking of the test molecule n-C_{16} in a small-scale testing unit. The effects of a more complicated feed stream and process scale-up are not considered. The same reaction conditions are used as in Brosius *et al.*, 2016 without further optimisation to allow for a focus on the study of the effects of metal size and location on the existing hydrocracking process.

The significance of this study is the contribution to the understanding and improvement of the **Pt/MFI** catalyst design as presented in the study by Brosius *et al.*, 2016, with the long-term aspiration to industrialise the process to produce a high yield of high cetane diesel. Current research into fossil fuel technology is a controversial topic in light of global climate change agreements. However, market research still predicts that the global hydrocracking market is expected to witness significant growth from 2015 to 2022 owing to the growing demand for middle and light distillates, especially in the emerging economies of BRICS and South-East Asia (GrandViewResearch, 2015). Therefore, research into a hydrocracking process which can produce high yields of clean diesel has immense value in keeping the existing technology as clean as possible until alternative fuels enter the markets.

Chapter 2

Literature Review

The previous chapter introduced the aim of this research and the context behind shape selective bifunctional hydrocracking to produce high yields of high quality diesel. This chapter will critically review existing theory to allow for a logical experimental design and analysis of the results to follow. The chapter is broken down into theory and practice of bifunctional hydrocracking for middle distillate production and existing synthesis methods for selective metal placement on supports.

2.1 BIFUNCTIONAL HYDROCRACKING

Bifunctional hydrocracking which occurs on a catalyst with metal and acidic function is reviewed in detail with focus on process conditions, chemistry, and the role of different catalysts. There will also be an emphasis on how hydrocracking over **Pt/MFI** fits into the current hydrocracking landscape.

2.1.1 Comparing Process Conditions

Bifunctional hydrocracking has different operating conditions according to the feed and required products. Table 2.1 shows the typical conditions expected for the main hydrocracking types as well as the conditions used for **Pt/MFI** hydrocracking.

Table 2.1: Typical Process Conditions for Industrial Hydrocracking (Bouchy *et al.*, 2009)

Conditions	**Conventional Hydrocracking**	**Mild Hydrocracking**	**LTFT Wax Hydrocracking**	**n-C_{16} Hydro-cracking with H_2O (Brosius *et al.*, 2016)**
Pressure (bar)	100 – 200	50 – 80	35 – 70	20
Temperature (°C)	350 – 430	380 – 440	320 – 370	235 – 255
H_2/feedstock (m^3/m^3)	800 – 2000	400 – 800	500 – 1800	600 – 800
Conversion (%)	70 – 100	20 – 40	20 – 100	20 – 70
Reactor Type	Trickle bed			

In general, bifunctional hydrocracking takes place in a trickle bed reactor (TBR) which consists of a solid catalyst bed with co-current gas-liquid flow. One of the advantages of a three-phase reactor is that it can achieve ideal plug flow due to the motionless catalyst bed. However, a serious disadvantage is the impracticality of catalyst replacement for reactions with rapidly deactivating

catalysts – a design consideration which should be highlighted when testing catalyst suitability. Most commercial TBR's are operated adiabatically at high pressure. The pressure elevation is necessary to improve gas solubility and mass and heat transfer rates; handle large gas volumes with less capital expense; and to slow down catalyst deactivation which may be caused by H_2 starvation. Temperature is also elevated according to the reactant feed and catalyst requirements (Al-Dahhan *et al.*, 1997). In the hydrocracking process, the liquid hydrocarbon reactants are fed into the TBR with H_2 gas, since H_2 gas is required for proper functioning of the (de)hydrogenation function (Bouchy *et al.*, 2009).

Conventional hydrocracking is primarily operated for converting heavy vacuum oil with sulphur and nitrogen contaminants into diesel and jet fuel or gasoline. It is a flexible process which can be adjusted according to product need (Weitkamp, 2012). It operates at high pressure and high H_2/feed ratios. **Mild hydrocracking** operates at less severe conditions and can be used to convert vacuum gas oil (VGO) or distillation residues to high-quality feedstocks for fluid catalytic cracking or dewaxing of lube oils (Weitkamp, 2012). Mild hydrocracking came about when conventional hydrotreaters where retrofitted to perform hydrocracking when market demand changed. However, the retrofit process design limits the severity of the process conditions, which explains why the operating pressure is much lower (Scherzer and Gruia, 1996). **LTFT wax hydrocracking** is a specialised hydrocracking process which is used specifically for LTFT wax processing. This process can achieve high conversion at conditions close to mild hydrocracking due to the high chemical reactivity of heavy alkane molecules and the absence of strong catalyst contaminants such as sulphur and nitrogen compounds (Bouchy *et al.*, 2009).

Comparing the hydrocracking process conditions used in Brosius *et al.*, 2016, it is evident that they are even milder than those used in industrial LTFT hydrocracking. These mild conditions make the process financially competitive, as a process handling lower temperature, pressure, and volumes of H_2 gas requires less capital and operating costs.

2.1.2 Understanding the Chemistry

The commonly accepted mechanism for bifunctional hydrocracking of long chain alkane reactants (such as n-C_{16}, a common feed used in model hydrocracking) will be reviewed along with the concept of ideal hydrocracking.

2.1.2.1 Bifunctional Hydrocracking Reaction Mechanisms

The earliest work on alkane hydrocracking mechanisms was by Weisz, 1962 and Coonradt and Garwood, 1964. Since then the subject has been extensively studied by several different research groups. From these studies, it is evident that the most accepted reaction mechanism for alkane hydrocracking on a bifunctional catalyst can be seen depicted in *Figure 2.1*, where the bifunctional catalyst consists of metal and acid sites.

The mechanism starts with the adsorption of alkane feed molecules (**F**) onto metal sites where dehydrogenation takes place to generate alkene intermediates ($\mathbf{F}_{=}$). The alkene intermediates then diffuse onto nearby acid sites where they undergo acid-catalysed skeletal isomerisation followed by one or more cracking events to form lighter alkenes ($\mathbf{D}_{=}$ or $\mathbf{G}_{=}$). Deprotonation of the lighter

alkenes then take place before diffusion back to the metal site for final hydrogenation. The hydrogenated lighter alkanes are then released from the metal surface via desorption as products such as diesel and gas (**D** or **G**).

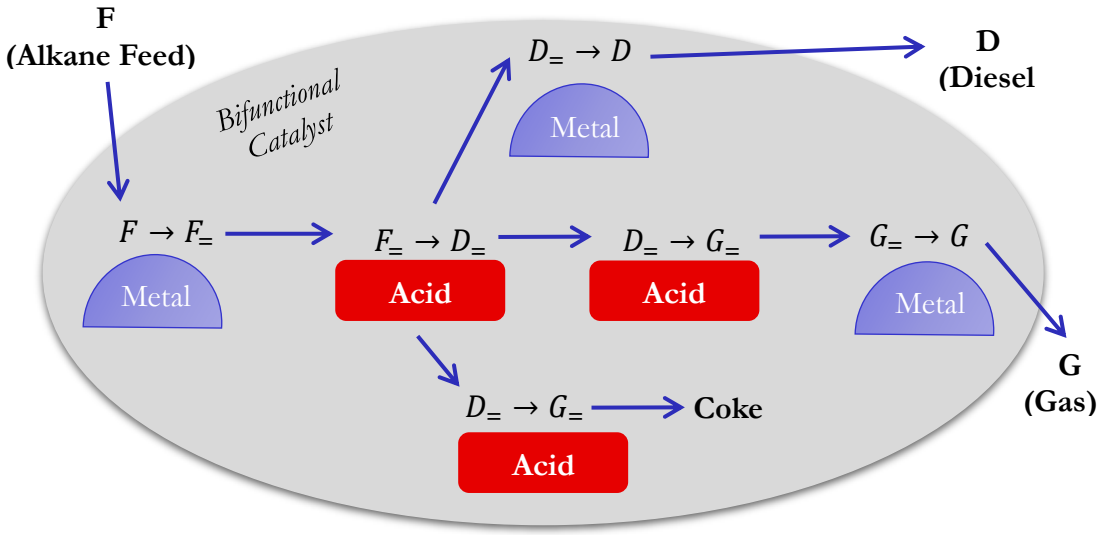

Figure 2.1: Schematic of hydrocracking reactions that use a bifunctional catalyst. Adapted from Zecevic et al., 2015.

In some cases, subsequent cracking on the acid sites can cause **coke** formation which leads to lower product yield and eventually catalyst deactivation (Bouchy *et al.*, 2009, Weitkamp, 2012, Zecevic *et al.*, 2015). Looking in more detail at the reactions which occur on the acid sites, an important distinction is made regarding the reaction sequence of isomerisation and cracking, as depicted in *Figure 2.2*.

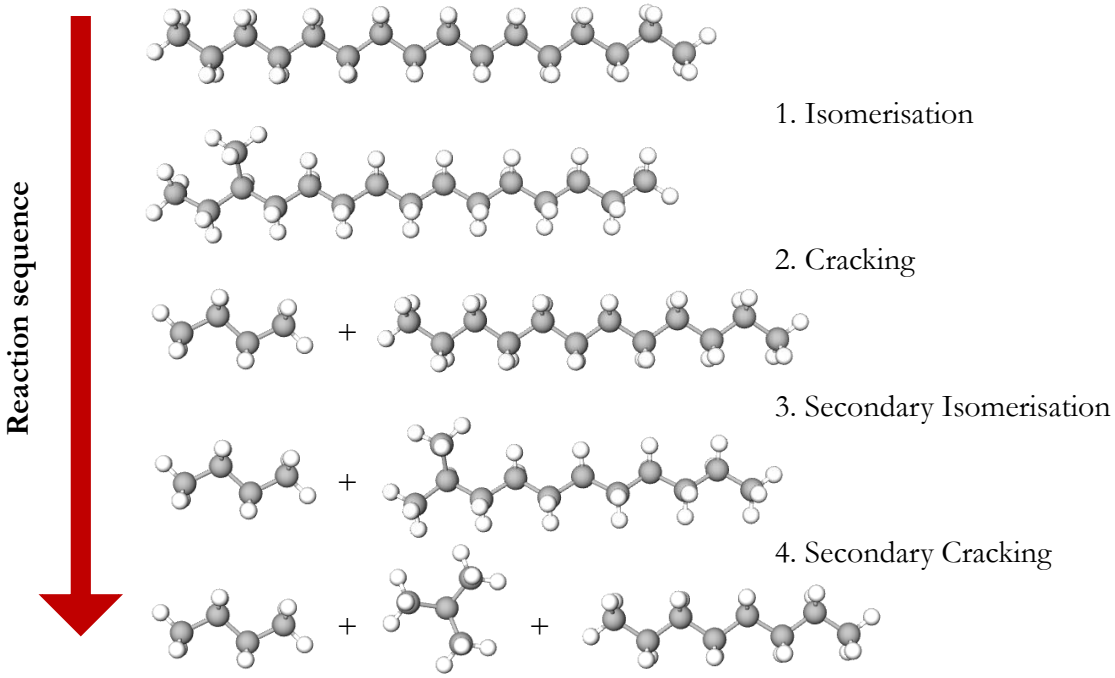

Figure 2.2: Schematic of the reaction sequence which takes place on the acid sites in bifunctional hydrocracking.

Using n-C_{16} as the reactant molecule, first isomerisation occurs followed by a cracking step and then secondary isomerisation and a further secondary cracking step, and so on. The isomerisation and cracking reactions always occur in this sequence (Weitkamp, 2012). Looking in more detail at the isomerisation steps, there are two possibilities which can occur (Bouchy *et al.*, 2009):

1) **Type A** isomerisation, which is significantly faster than Type B, where the degree of branching is not modified but positional changes are seen. For example:

2) **Type B** isomerisation, where the branching degree is increased or decreased by the formation of a cyclic carbenium ion intermediate. For example:

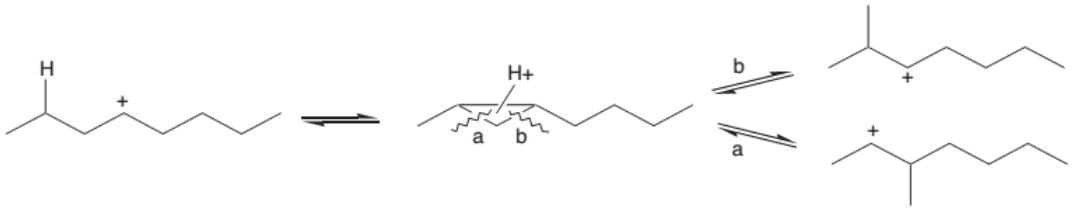

Furthermore, the cracking steps consist of a scission of a carbon-carbon bond in the β-position of the positively charged carbon atom of the carbocation intermediate. This is known as β-scission and *Figure 2.3* below shows the principal modes of β-scission which can occur (Weitkamp *et al.*, 1983).

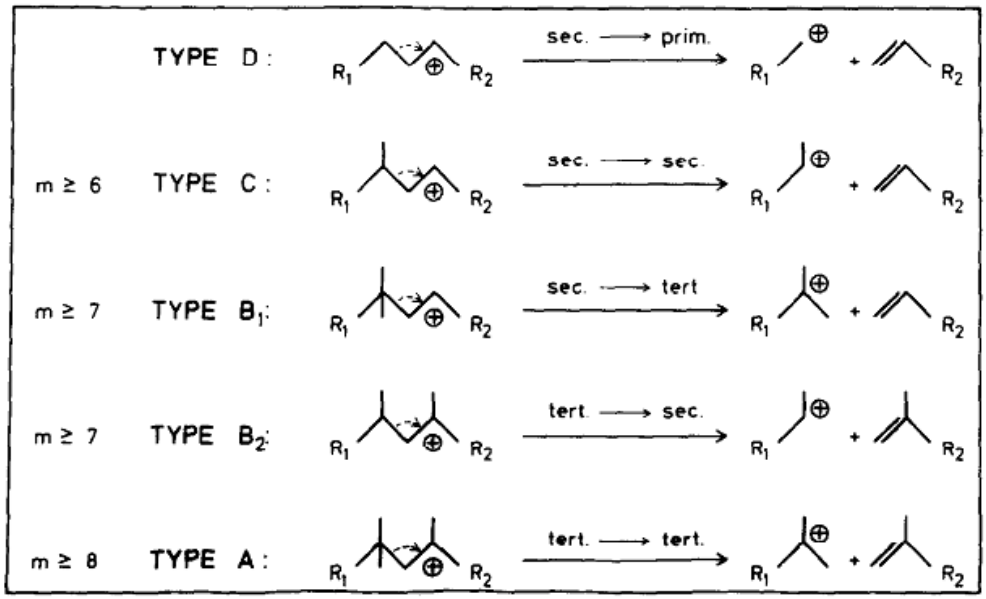

Figure 2.3: Principal β-scission modes where m is the number of carbon atoms in the reactant molecule. Taken from Weitkamp et al., 1983.

As you move from type D to type A β-scission, the degree of branching in the products increases. As will be discussed later when looking at hydrocracking over different zeolites, some catalysts can prevent certain types of β-scission to selectively produce certain degrees of branching products.

The relative rates of β-scission decrease from type A to type D and together with the two types of isomerisation arrangements, the following qualitative order of rates for alkylcarbenium ion chemistry was determined (Weitkamp, 2012):

$$Type\ A\ \beta scission > Type\ A\ isomerisation > Desorption > Type\ B\ isomerisation \approx Type\ B_1\ \beta scission \approx Type\ B_2\ \beta scission > Type\ C\ \beta scission \gg Type\ D\ \beta scission$$

Going forward, these mechanisms will be used in evaluating the hydrocracking results as they are widely accepted and have shown to hold in numerous explanations of hydrocracking results.

2.1.2.2 Ideal Hydrocracking

The concept of "ideal hydrocracking" is widely accepted and helps rationalise numerous features of bifunctional hydrocracking. The concept is well defined by Weitkamp, 2012 as a special case of bifunctional catalysis where there is rapid desorption of the primary cracking products at the acid sites. This rapid desorption only occurs with a sufficiently active (de)hydrogenation function which ensures a steady-state concentration of n-alkenes high enough to rapidly displace the alkyl-carbenium ions from the acid sites through competitive adsorption/desorption. Therefore, the chemical steps at the acid sites (isomerisation and cracking) are rate- and selectivity- controlling.

Ideal hydrocracking allows for pure primary hydrocracking selectivity of long-chain alkanes, where pure primary hydrocracking is defined as a special case of hydrocracking where every reactant molecule is only cracked once. An example of the product distribution of ideal and non-ideal hydrocracking is demonstrated in *Figure 2.4*.

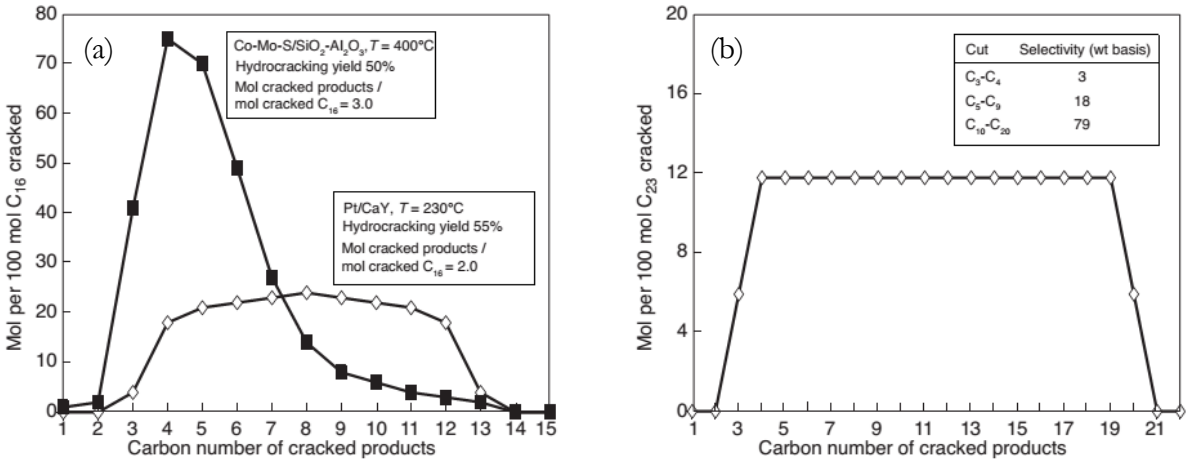

Figure 2.4: (a) Product distributions of primary (Pt/CAY) and secondary (Co-Mo-S/SiO_2-Al_2O_3) hydrocracking, (b) Theoretical primary cracking products from C_{23}. Adapted from Bouchy et al., 2009.

In *Figure 2.4 (a)*, the ideal **Pt/CaY** and non-ideal **Co-Mo-S/SiO_2-Al_2O_3** product distributions are shown as the number of moles of each carbon number of cracked products. The non-ideal catalyst shows a skewed distribution with most of the products between C_3 to C_6, suggesting extensive secondary cracking of the primary fragments. The reason for the skewed distribution is that the non-ideal catalyst has a weak (de)hydrogenation function – meaning that there is not a high enough concentration of n-alkenes to displace the primary cracking products. In the case of the ideal hydrocracking catalyst, the product distribution is fully symmetrical around carbon number = 8.

Since with breaking each reactant molecule only once and assuming an equal probability of the chain breaking at any location, the total product molecules should be equal for each carbon length. It is notable that there are no C_1 (and C_{15}) and C_2 (and C_{14}) products, suggesting that the reactant molecules do not break at these locations. C_3 (and C_{13}) do occur but at much lower amounts than the other length cracking products. The theoretical graph of primary hydrocracking of C_{23} (a more representative test molecule of wax) is represented in *Figure 2.4 (b)*. In this case, primary cracking achieves a final product with 79 % C_{10}-C_{20} cut, which is considered a high yield in industrial hydrocracking (Bouchy *et al.*, 2009).

The advantage of achieving ideal hydrocracking is that it allows for flexibility in the hydrocracking process. By changing the severity of the reaction it is possible to achieve products such as skeletal isomers, hydrocracked products with pure primary cracking selectivity, and hydrocracking products with a high yield of light fragments (Weitkamp, 2012). Furthermore, a 79 % cut of C_{10}-C_{20} can be achieved through the primary cracking of a common molecule found in wax, tricosane. Therefore, in evaluating the hydrocracking results of this study, ideal hydrocracking will be used to distinguish superior catalyst performance.

2.1.3 The Role of Catalyst Design

Different catalyst compositions are used in varying bifunctional hydrocracking scenarios depending on the feed composition and the required product. A summary of some of the main differences is given by looking at the metal and acid function separately.

2.1.3.1 Metal Function

Noble metals (such as Pt and Pd) and non-noble transition metals from group VIA (Mo, W) and VIIIA (Co, Ni) can be used for the (de)hydrogenation function in hydrocracking.

In the case of crude oil feedstocks, sulphur content is considerable (up to ~3%) and the metal function needs to be resistant. Therefore, the metal function is most commonly a transition metal applied as a sulphide (Ni-W, Ni-Mo, Co-Mo) (Bouchy *et al.*, 2009). Where sulphur usually poisons metallic function, sulphided metals use the sulphur impurities to increase activity (Weisser and Landa, 2013).

In the case of LTFT wax feedstocks, which contain negligible amounts of sulphur (below 500 ppm), the use of noble metals can be very effective; since in a low sulphur environment, the (de)hydrogenation activity of noble metals supersedes sulphided transition metals (Bouchy *et al.*, 2009). In comparing the strongest hydrogenating noble metals (Pt and Pd), Pt has consistently shown to be more active for (de)hydrogenation (Scherzer and Gruia, 1996). Brosius *et al.*, 2016 recently re-affirmed this by showing that Pd produced a more branched hydrocracking product, which indicates a lower hydrogenation function. However, it must be noted that noble metals are much more expensive and this must be considered when choosing an appropriate metal function. The replacement of noble metals by base metals has been attempted in literature, such as non-sulphided Ni (de Haan *et al.*, 2007) and non-sulphided Co and Mo oxides (Böhringer *et al.*, 2007). However, in both cases, significant amounts of C_1 and C_2 were produced which is attributed to hydrogenolysis – a reaction which proceeds much more slowly on Pd and Pt.

2.1.3.2 Acid Function

In an ideal hydrocracking catalyst, the rate determining step occurs at the acid sites, as discussed in **Section 2.1.2**. Therefore, the product selectivity is highly dependent on the shape and nature of the acid sites. For instance, the possibility of secondary cracking increases with increased residence time of intermediates near the acid sites. Therefore, diffusional limitations or confinement effect must be minimised to prevent secondary cracking. Furthermore, preferential cracking at the ends of the reactant molecules can cause unwanted product selectivity towards light gases. This has been seen on zeolites like ZSM-22 (TON morphology) where the long chain reactant molecule only penetrates with its end into the pore of the solid catalyst. Acid strength also plays an important role in reducing overcracking. The following are the main types of acid functions in order of acid strength which are used in hydrocracking catalysts (Scherzer and Gruia, 1996):

Zeolite > SiO_2-Al_2O_3 > Al_2O_3-halogen > Al_2O_3

Usually high middle distillate yields are obtained when using solid acids with weak and medium strength (SiO_2-Al_2O_3 and lower) as overcracking of the intermediates can be minimised. Some zeolites can produce high yields of middle distillates with strong acid function – such as zeolite Y which has a large-pore structure (which helps prevents diffusion limitations). Whereas, other zeolites such as MFI, have a very strong acid site function and micropore structure which results in considerable secondary cracking (Weitkamp *et al.*, 1983). In general, compared to amorphous catalysts, zeolite-based hydrocracking catalysts are advantageous for the following reasons (Scherzer and Gruia, 1996):

- Greater cracking activity due to increased acidity
- Better thermal/hydrothermal stability
- Stronger resistance to nitrogen and sulphur compounds
- Low coke-forming tendency
- Easily regenerable
- Potential shape-selectivity properties

Therefore, looking at the metal and acid site function alternatives, it is evident that Pt metal on a zeolite is a strong combination for a bifunctional hydrocracking catalyst when processing a feed stream with minimal impurities (such as S and N compounds).

2.1.3.3 Metal and Acid Intimacy Criterion

From the first studies on metal and acid site distance by Weisz., 1962, it was found that there is a maximum distance between acid and metal site before a loss in activity occurs, dubbed the 'intimacy criterion'. This occurs when diffusion limitations of the molecules between acid and metal site are high and concentration gradients develop causing a decrease in activity. Furthermore, selectivity may also be affected by intimacy such as when iso-alkanes experience secondary reactions when the metal sites aren't close enough to perform hydrogenation (Zecevic *et al.*, 2015).

The general belief for intimacy in bifunctional catalysts is that 'the closer the better' (Weitkamp and Ernst, 1990, Zecevic *et al.*, 2015) however, recently Zecevic *et al.*, 2015 showed that this is not the case for hydrocracking over a Y type zeolite. The study selectively placed Pt metal on zeolite

Y or the alumina binder of a mixed extrudate. It was seen in the hydrocracking of n-C_{19}, that Pt metal on the alumina binder minimised secondary cracking. It is suggested that Pt on the binder encourages the hydrocracking reactions to occur on the outer surfaces of the Y zeolite, which reduces diffusion limitations between the metal and acid sites. Therefore, diffusion limitations caused by distance between metal and acid sites will be considered in this study when testing bifunctional hydrocracking catalysts.

2.1.3.4 Metal Size Dependency under Ideal Hydrocracking

In nanoscience research, exceptional activity increases have been seen using small NPs. For example, with Au NPs it is suggested that the quantum confinement effects change the electronic structure leading to unusually high catalytic activity (Li and Somorjai, 2010). However, under ideal hydrocracking conditions the acid sites are rate limiting – as discussed in **Section 2.1.2**, meaning that the metal sites cannot be rate limiting (as long as there is a sufficient de(hydrogenation) function). Therefore, the metal particle size should not play a role in the activity of bifunctional hydrocracking but providing a sufficient de(hydrogenation) function is important when comparing hydrocracking catalysts.

2.1.4 A Focus on Zeolites for the Acid Function

Zeolites are crystalline aluminosilicates of group IA and group IIA elements (such as calcium, sodium and potassium). Chemically, a zeolite can be represented by the following equation (Jacobs *et al.*, 2001):

$$M_{\frac{2}{n}}O \cdot Al_2O_3 \cdot ySiO_2 \cdot wH_2O \qquad \text{Equation 2.1}$$

Where y is in the range of 2-10, n is the cation valence, and w represents the amount of H_2O in the voids of the zeolite. From a structural perspective, zeolites are complex, crystalline inorganic polymers which form a 3-dimensional framework. The building blocks are AlO_4 and SiO_4 which are linked by sharing oxygen ions. There are over 130 different framework types which all vary in the size of pore openings and the dimensionality of the channel systems (Jacobs *et al.*, 2001). Zeolite Y and ZSM-5 are the most important industrial catalysts in the refining sector and are used for a number of functions as seen in Table 2.2 (Vermeiren and Gilson, 2009).

Table 2.2: Refining Applications of Zeolite Y and MFI

Zeolite structure code **Zeolite name**	**FAU** **Y, USY**	**MFI** **HZSM-5, TS-1**
Iso-dewaxing		Bifunctional
Dewaxing		Monofunctional
Hydrocracking	Bifunctional	
Hydrodearomatization	Bifunctional	
FCC	Monofunctional	Monofunctional
Olefin oligomerization		Monofunctional

Zeolite Y is the only zeolite currently used in industry for hydrocracking as it can achieve ideal hydrocracking (Vermeiren and Gilson, 2009). Whereas, HZSM-5 is not currently used industrially in hydrocracking due to the nature of the catalyst to induce secondary cracking. A comparison of zeolite Y and HZSM-5 will be discussed below in relation to activity and ability to achieve primary

cracking as well as selectivity in hydrocracking. This analysis is conducted to compare a currently used zeolite in industry with the novel catalyst design investigated in this study (**Pt/MFI**). *Figure 2.5* shows a schematic of the zeolite pore structures for zeolite Y and HZSM-5.

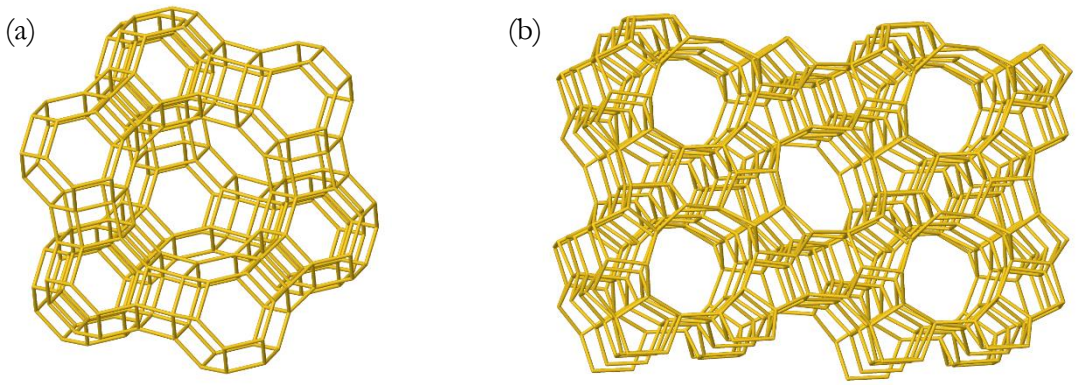

Figure 2.5: Schematic of zeolite structures for (a) Y and (b) HZSM-5. Adapted from Jacobs et al., 2001.

Zeolite Y has an FAU framework type which is made up of sodalite cages which are joined via double 6-rings, creating a supercage with four tetrahedrally-oriented, 12-ring pore openings and a 3-dimensional channel system. Zeolite HZSM-5 has an MFI framework type which is made up of pentasil units which from pentasil chains. Mirror images of these chains are connected together to form sheets with 10-ring holes. The sheets are then linked together to form the three-dimensional structure. The pore openings are 10-rings rather than 12-rings (as with FAU), which affects the shape selectivity during catalysis (Jacobs *et al.*, 2001).

2.1.4.1 Zeolite Acidic Activity in Relation to Ideal Hydrocracking

An investigation into different zeolite activity for n-C_4 hydrocracking was conducted by Rastelli *et al.*, 1982, as seen in *Figure 2.6*. From the investigation, it was determined that at high Al/(Al+Si) ratios, the zeolites have a high concentration of weak acid sites – which reflects an overall low acidity (including number of acid sites and individual acid strength). The low acidity is seen to reflect low activity in the cracking of n-C_4. Alternatively, at low Al/(Al+Si) ratios, the concentration of acid sites becomes lower but the individual acid site strength is higher – which results in an overall higher acidity. The high acidity zeolites show a high activity for cracking. It is important to note that as the overall acidity strength of the zeolite increases, the activity increases and subsequently more secondary cracking is observed (Bouchy *et al.*, 2009).

Zeolite HZSM-5 and Y (labelled in *Figure 2.6* as ZSM-5 and Faujasite, respectively) are on the opposite ends of the activity scale and this results in distinct differences in the hydrocracking products. For example, pure primary cracking is achieved in n-C_{15} and n-C_{16} hydrocracking over a large pore **Pt/Ca-Y** zeolite, whereas a high degree of secondary cracking is seen when using **Pt/HZSM-5**, as depicted in *Figure 2.7* (Weitkamp *et al.*, 1983). This is determined by the fact that the **Pt/Ca-Y** has a symmetrical distribution around C_8, which represents primary cracking, whereas **Pt/HZSM-5** shows an unsymmetrical distribution with high numbers of C_3-C_6,

indicating secondary cracking of the longest fragments has occurred (as discussed in **Section 2.2.1**).

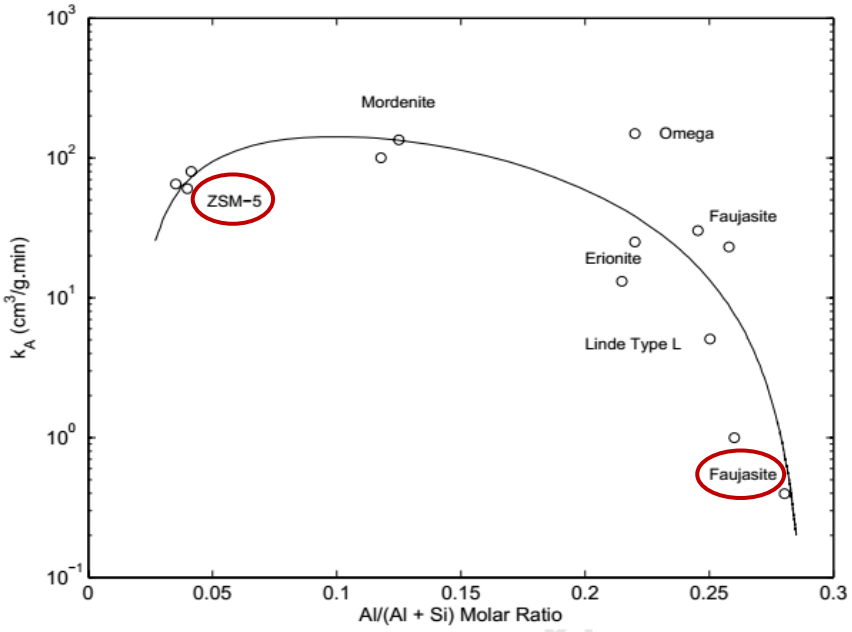

Figure 2.6: Zeolite activity as a function of Al/(Al+Si) ratio in n-butane cracking. Adapted from Kukard., 2008 and Rastelli et al., 1982.

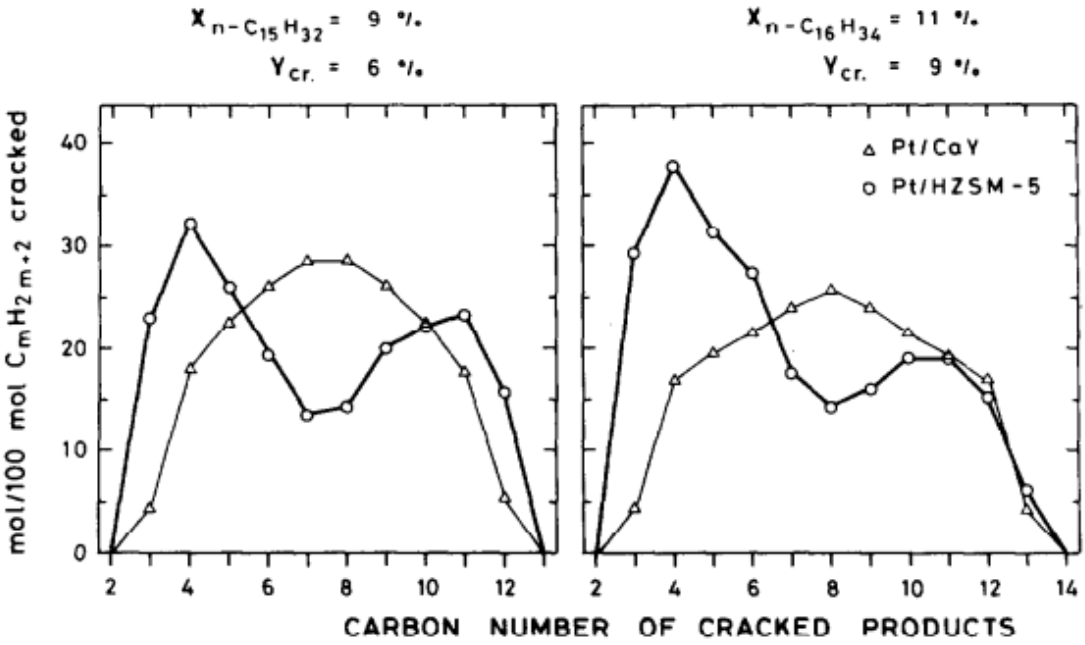

Figure 2.7: Primary versus secondary hydrocracking over Pt/CaY and Pt/HZSM-5. Taken from Weitkamp et al., 1983.

The high activity and subsequent high degree of secondary cracking seen with **Pt/HZSM-5** is attributed to both strong adsorption of the longest fragments on the acid sites and hindered diffusion of the same longest fragments out of the narrow HZSM-5 pores. Zeolite Y does not show signs of secondary cracking as it has a lower overall acidity (and activity) and an open pore structure (Weitkamp *et al.*, 1983).

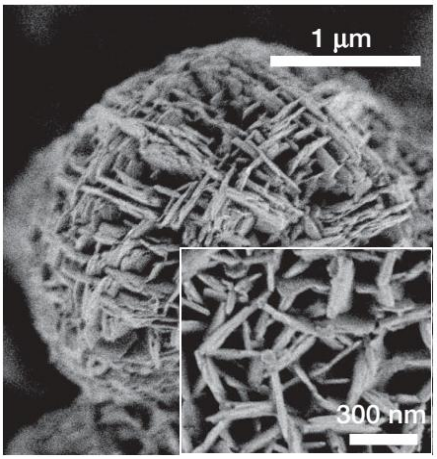

Figure 2.8: SEM image of MFI NSs with a multilamellar structure. Taken from Choi et al., 2009.

In a strategy to decrease the diffusion path between the acid and metal inside zeolite particles, MFI type zeolite nanosheets (NS) were synthesised by Choi *et al.*, 2009. The preparation includes designing a diquaternary ammonium surfactant which acts as a structure directing agent (SDA) for the MFI zeolite structure. The surfactant is composed of a long-chain alkyl group and two quaternary ammonium groups. The diquaternary ammonium head group acts as the SDA, whereas the hydrophobic interaction between the long-chain tails induces a micellar structure. Therefore, an ultrathin framework of NSs was formed at the hydrophilic part of the micelles and the hydrophobic part inhibited excessive growth of the zeolite (Choi *et al.*, 2009). *Figure 2.8* shows a SEM image of the zeolite which has a plate-like morphology that is made up of NSs in a 3-dimensional structure.

Verheyen *et al.*, 2013 reproduced the MFI NSs successfully for use in bifunctional hydrocracking. In n-C_{12} hydrocracking, the MFI NSs show a tendency to produce a more primary hydrocracking product in comparison to bulk MFI, as seen in *Figure 2.9*. This is demonstrated by comparing the number of product moles when 100 moles of n-C_{12} was cracked, where pure primary cracking produces 200 moles/100 moles cracked (as indicated in the graphs by the straight dotted lines).

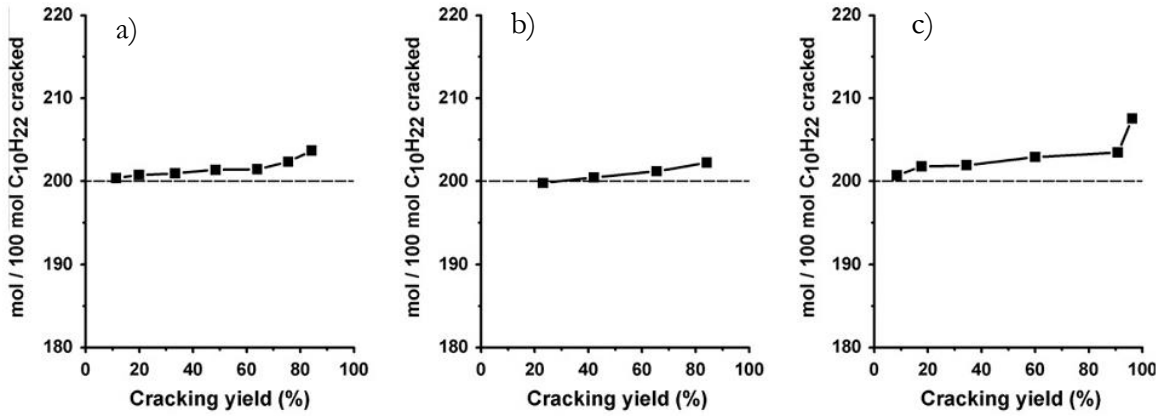

Figure 2.9: Primary vs secondary hydrocracking on (a) NSs 2 nm (b) NSs 8 nm, and (c) bulk MFI. Taken from Verheyen et al., 2013.

It is suggested that pure primary cracking is achieved up to higher cracking yields for NSs since there is a decrease in diffusion limitations (which usually cause further cracking of the reactants). However, it is known that the severity of secondary cracking increases with increasing reactant feed length (Weitkamp *et al.*, 1983) and n-C_{12} is not entirely representative of the usual feed length for wax hydrocracking. It is suspected that when cracking longer reactant molecules, the improvement seen by the NSs to achieve primary hydrocracking will lessen.

2.1.4.2 Hydrocracking Shape-Selectivity in Narrow Pore Zeolites

Due to their complex structures, it has been observed that certain zeolites exhibit shape selective behaviour for certain reactions. Three main types of shape selectivity have been identified as follows (Csicsery, 1984):

1. Reactant selectivity which occurs when only some of the reactant molecules are small enough to diffuse into the catalyst pores.
2. Product selectivity which occurs when some of the product molecules are too bulky to diffuse out of the pores. These products are either converted to less bulky molecules or eventually deactivate the catalyst by blocking the pores.
3. Restricted transition state selectivity which occurs when certain reactions are prevented because the transition state molecules do not fit in the pores.

In terms of hydrocracking, the most relevant zeolite which displays shape selectivity in cracking products is HZSM-5. This effect will be compared to conventional non-shape selective hydrocracking over zeolite Y as follows:

Returning to the study by Weitkamp *et al.*, 1983, **Pt/HZSM-5** hydrocracking products consist mainly of n- and i-alkanes with single methyl branching. Small amounts of dimethyl isomers occur but no products with ethyl side chains or more than two methyl branchings are detected. This is largely different from zeolite Y hydrocracking, which has no selectivity towards certain types of branching and sees a full range of branched products. The reason for this vast difference is because hydrocracking over HZSM-5 displays preferential C-type β-scission reactions (as depicted in *Figure 2.3)* because the formation of bulky tertiary carbenium ions is sterically hindered in the HZSM-5 micropores (showing restricted transition state selectivity). However, large pore zeolites (like zeolite Y) allow both type A, B and C β-scission reactions as they do not display shape selectivity.

Figure 2.10 displays the vast difference between **Pt/CaY** and **Pt/HZSM-5** overall content of branched isomers in the cracked products versus carbon number of the feed. Zeolite Y produces significantly more branched products, with a minimum of 60 % versus 20 % for HZSM-5. Another important observation from *Figure 2.10* is that the yield of isomers from long chain n-alkanes on **Pt/HZSM-5** hydrocracking is strongly dependent on chain length. Three explanations for the influence of chain length are presented by Weitkamp *et al.*, 1983: (i) an increase in the intrinsic rates of β-scission of monobranched carbenium ions (ii) a decrease in desorption rates from the acid sites (iii) a decrease in intracrystalline diffusivities of monobranched species.

Therefore, **Pt/HZSM-5** is an attractive opportunity for a shape-selective hydrocracking catalyst if the acid function activity can be controlled. This is where the recent work by Brosius *et al.*, 2016 comes in and will be discussed in detail.

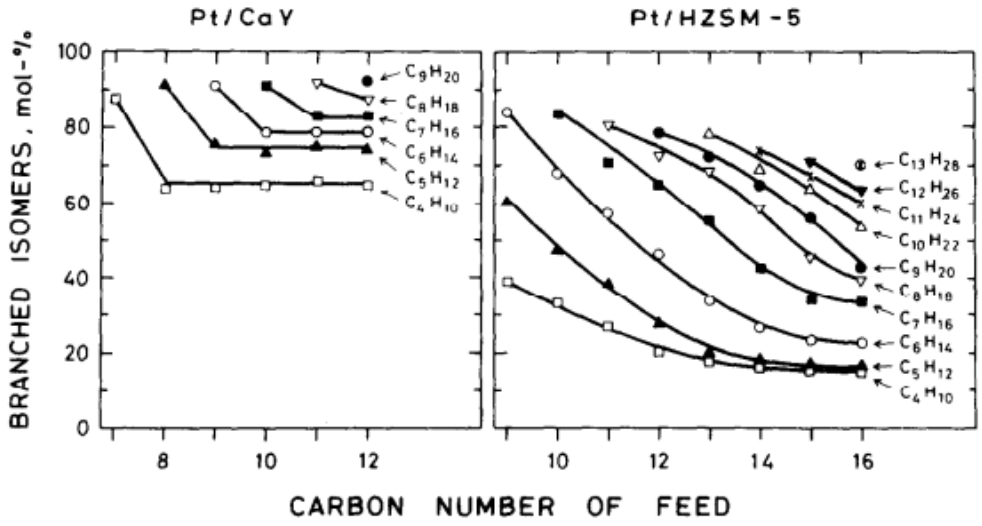

Figure 2.10: Product branching in hydrocracking of n-alkanes over Pt/CaY and Pt/HZSM-5 at ~50% yield of cracked products. Taken from Weitkamp et al., 1983.

2.1.4.3 Hydrocracking over Pt/MFI in the Presence of H_2O

Brosius *et al.*, 2016 showed for the first time a method to perform shape-selective hydrocracking on an MFI zeolite (also called HZSM-5) whilst still achieving primary cracking. *Figure 2.11* shows the C_4/C_{12} chain length products, which represent primary hydrocracking at a ratio of 0.33, across varying conversion. In the presence of H_2O, it is evident that primary cracking is achieved up to high conversion, whereas without H_2O all the **Pt/MFI** catalysts show severe secondary hydrocracking. It is suggested that primary hydrocracking occurs because H_2O competes for adsorption on the acid sites which encourages desorption of the primary cracked products. The NSs display a lower degree of secondary cracking in the absence and presence of H_2O most likely due to enhanced mass transport of the products out of the shorter micropores and mesopores. Lastly, it is evident that with **Pt-6/MFI** (Pt diameter 6 nm), the severity of secondary hydrocracking increased (with and without H_2O). This suggests the importance of high metal dispersion, which reduces diffusion limitations between metal and acid sites (Brosius *et al.*, 2016).

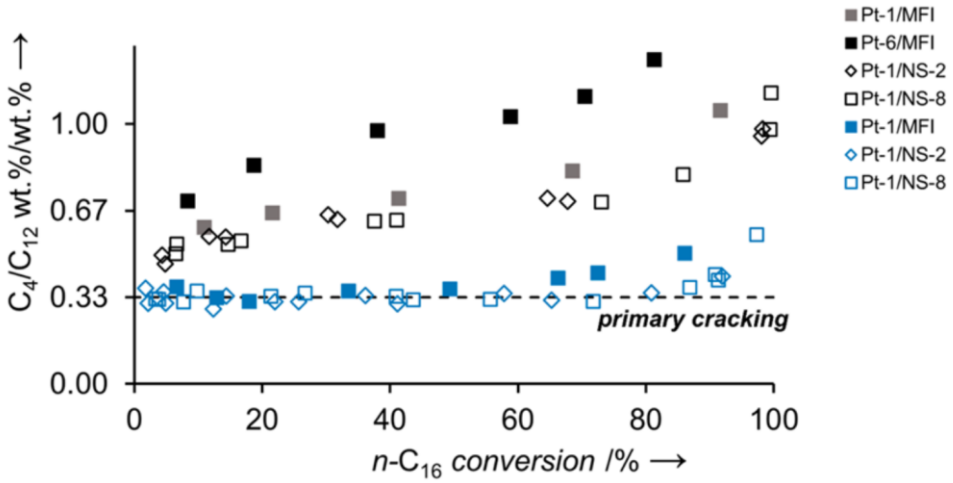

Figure 2.11: Primary vs. secondary hydrocracking in the absence (black) and presence (blue) of H_2O over Pt/MFI (Pt diameter 1 and 6 nm) and Pt-1/NS (thickness 2 and 8 nm). Taken from Brosius et al., 2016.

The shape-selectivity of MFI hydrocracking in the presence of H_2O is well represented by looking at the amount of linear, primary cracking products, as seen in *Figure 2.12*. From the primary cracking products, n-C_{12} gives the most insightful results, as this is the longest cracked product and therefore the most likely to stay adsorbed on the acid sites and experience secondary isomerisation. It is important to note that only once the first objective, achieving ideal hydrocracking (which produces primary cracking products), has been attained can the catalysts be compared for differences in branching selectivity.

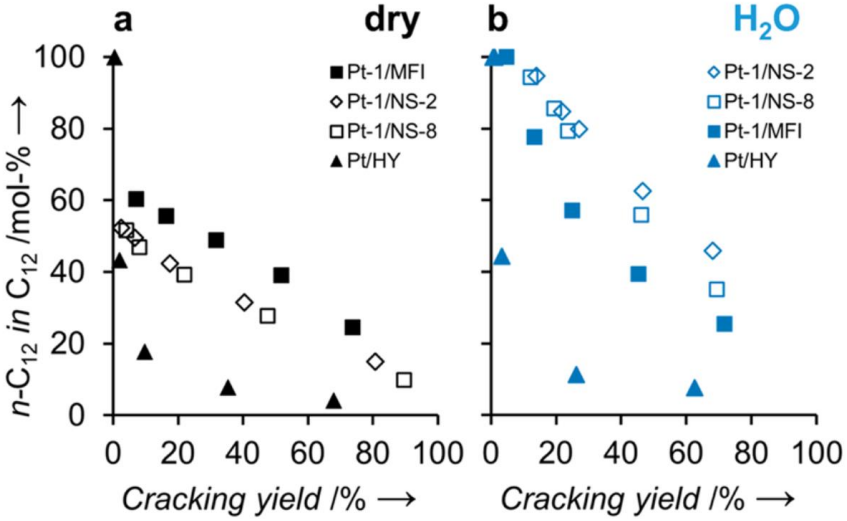

Figure 2.12: Amount of linear C_{12} in the C_{12} product fraction in the absence (black) and presence (blue) of water over Pt/MFI and NSs. Taken from Brosius et al., 2016.

Hydrocracking over **Pt/HY** shows almost exclusively branched alkane products in the presence and absence of H_2O. This type of hydrocracking is not shape selective and branched primary cracked products form from secondary isomerisation. Whereas over MFI zeolites, there is a much higher selectivity toward linear products due to preferential type C β-scission reactions. Furthermore, in the presence of H_2O, this effect is heightened as H_2O, not only prevents secondary cracking, but also reduces secondary isomerisation of the linear primary cracked products. Therefore, almost completely linear products are seen at low conversion. However, with increasing conversion, the probability of secondary isomerisation increases as i-C_{16} is consumed by hydrocracking. Looking at the NS samples, it is evident that in dry hydrocracking the NSs show more branched products than bulk MFI. It is suggested that, because competitive adsorption governs the probability of secondary isomerisation, branching increases as the shorter fragments are more easily removed from the short micropores of the NSs leaving the longer fragments to isomerise. Whereas, in the presence of H_2O, the NS samples produce less branched products than MFI as competitive adsorption is controlled and diffusion out of the shorter micropores encourages desorption of primary cracked products *(Brosius et al.*, 2016).

Sufficient Metal Loading

To investigate the effects of varying amounts of metal, Brosius *et al.*, 2016 made a series of catalysts with metal loadings from 0.1 to 0.9 wt. %. It was seen that in the presence of H_2O, metal loadings as low as 0.1 wt.% achieve primary hydrocracking. However, focusing on Pt, it is evident that the fraction of linear products increases steadily with Pt loading up until 0.9 wt. %. Therefore, a

minimum metal loading of 0.9 wt. % will be used in all catalyst preparation in this study to increase the yield of linear products.

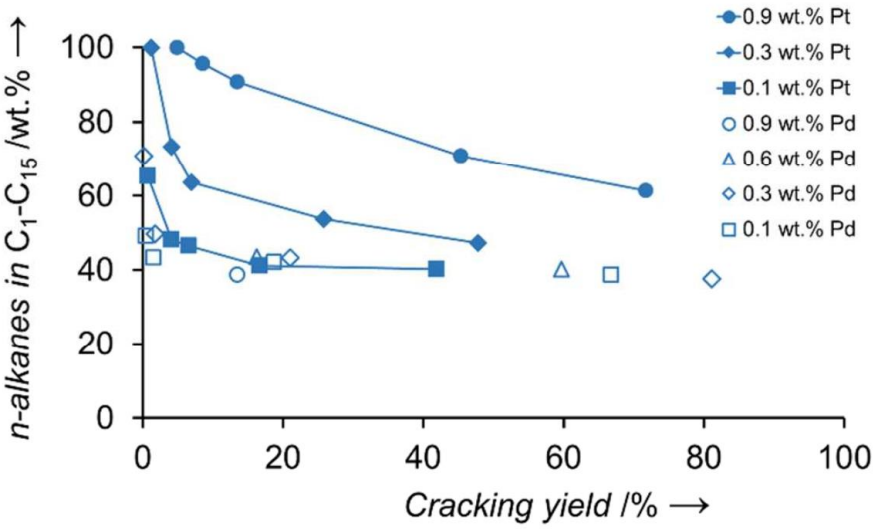

Figure 2.13: Linear cracking products against cracking yield over Pt/MFI and Pd/MFI with increasing metal loading at W/F: 875 – 3500 kgs/mol and 225 – 245 °C. Taken from Brosius et al., 2016.

Metal Location

The importance of metal location was established when studying varying pre-treatments after the wet impregnation of **Pt/MFI** (Brosius *et al.*, 2016). It was observed that varying heating rates of the oxidation/reduction steps affects the metal dispersion. At a higher heating rate, the average particle size determined by CO chemisorption was 6 nm, whereas at a lower heating rate, the average particle size was significantly reduced to 1 nm. It is assumed that at 6 nm, the metal is outside the micropores since they have a maximum diameter of ~0.55 nm. The significance of this difference is presented in *Figure 2.14*, which shows the percentage of linear alkane products versus the cracking yield.

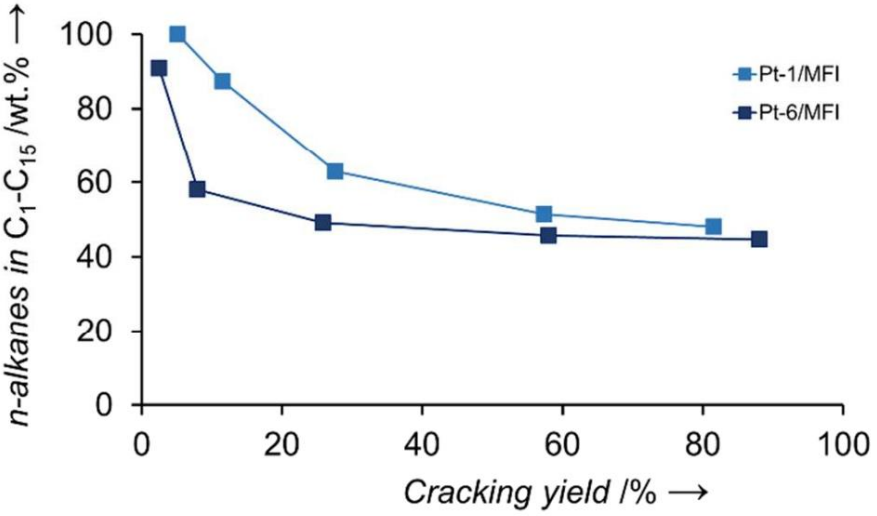

Figure 2.14: n-Alkane selectivity versus cracking yield in the presence of H_2O over Pt/MFI with 1 nm and 6 nm particle averages. Taken from Brosius et al., 2016.

Pt-6/MFI shows a much quicker decline in linear products at higher cracking yields. The result shows that by a decrease in metal dispersion and therefore, expected movement of metal outside the micropores, the tendency for secondary isomerisation is increased. It is expected that secondary isomerisation is affected by metal location, as internal metal encourages reaction inside the micropores which is necessary to achieve type C β-scission selectivity. Furthermore, when the metal sites are closer to the acid sites, a non-diffusion limited supply of dehydrogenated feed molecules become available to displace the primary cracked products preventing secondary isomerisation (Weitkamp *et al.*, 1983, Brosius *et al.*, 2016).

Therefore, it is evident from these results that metal dispersion and location directly affect the selectivity of hydrocracking over **Pt/MFI** in the presence of H_2O. To quantify the effects, this study will perform hydrocracking on catalysts with metal exclusively inside and outside the micropores, whilst keeping the overall active metal surface area as constant as possible (by keeping the same metal loading and average particle size).

2.2 PLACING METAL OUTSIDE MFI MICROPORES

Placing the metal exclusively outside the MFI micropores of diameter ~0.55 nm requires the formation of Pt NPs before supporting them. This will prevent any particles from forming inside the micropores which can occur during wet impregnation. There are four main categories for NP synthesis which are outlined as follows (Pachón and Rothenberg, 2008):

Reduction of Metal Salt Precursors

The most common method for making NPs was discovered ~150 years ago by Michael Faraday. The mechanism for the stepwise formation of NPs is based on nucleation, growth and agglomeration of the metal atoms as follows:

$$xM^{n+} + nxe^{-} + stabiliser \rightarrow M^{0}_{n(cluster)} \qquad \text{Equation 2.2}$$

A reducing agent (such as hydrogen, alcohol, hydrazine or borohydride) is mixed with the metal precursor salt in the presence of a stabilising agent (ligands, polymers or surfactants). This allows for nucleation and growth and then the stabilising agent prevents undesired agglomeration and formation of metal powders (Pachón and Rothenberg, 2008).

Electrochemical Synthesis

An electrochemical method was developed in the 1990s and includes five steps:

1. Oxidative dissolution of the metal bulk anode
2. Migration of the metal ions to the cathode
3. Reductive forming of zerovalent metal atoms at the cathode
4. Nucleation and growth of the metal particles
5. Stopping the growth process and stabilising with protecting agents

This method has been successfully applied in the preparation of monometallic NP organosols and hydrosols including Pd, Ni, Co, Fe, Ti, Ag and Au (Pachón and Rothenberg, 2008).

Reduction of Organic Ligands in Organometallic Precursors

Organometallic precursors can also be used to form NPs. From low-valency metal complexes, organic ligands are reduced (typically with H_2 or CO). The reduced ligands then leave the metal centre, which allows the clustering of metal atoms. This is represented in Equation 2.3 (Pachón and Rothenberg, 2008):

$$nM(L)_x + xH_2 + stabiliser \rightarrow M^0_{n(cluster)} + xLH_2 \qquad \text{Equation 2.3}$$

Metal Vapour Chemistry

Using metal vapour chemistry, the atomic vapour of a metal is condensed into a cold liquid which contains a stabiliser, upon heating the dissolved metal atoms will form NPs. When the liquid acts as a stabiliser it is possible that the metal vapour will condense with the solvent vapour giving a solid matrix.

2.2.1 Monodisperse Pt NP Colloid by Metal Salt Reduction

A detailed literature review on the most common method for Pt NP synthesis through metal salt reduction was undertaken to find a suitable method to place monodisperse Pt NPs on MFI.

2.2.1.1 Theory Behind Monodispersed Particle Formation

In the 1950s, LaMer and Dinegar re-investigated the preparation of colloidal dispersions by condensation from supersaturated solutions to include newer theories on phase transitions. The developed theory, which accounts for the production of monodisperse colloids, is now widely accepted. The theory is well summarised by a plot of precursor concentration over time, as depicted in *Figure 2.15*.

Rapid injection of reagents raises the precursor concentration above the nucleation threshold encouraging a short nucleation burst. After nucleation, the concentration drops back down below the nucleation threshold preventing any further nucleation. This step ensures that the final NPs will be of similar size and it is very important that a single, isolated nucleation step occurs. The length and speed of the nucleation step determines the initial size distribution of the NPs and is optimised in synthesis by adjusting concentration, temperature and other parameters (Murray *et al.*, 2000). Following nucleation, the already formed nuclei of similar size enter the growth phase. The particles grow by diffusion of the precursor species toward the surface of the particles and stepwise addition of atoms/ions. It has been observed that the particles grow at a similar rate therefore forming a colloidal dispersion of monodisperse NPs (Murray *et al.*, 2000, LaMer and Dinegar, 1950).

Furthermore, it is also well known that an extended controlled growth phase can make the NPs more uniform in size. This phenomenon is known as focusing the size distribution (Reiss, 1951). A system can then exhibit a second growth phase, known as Ostwald ripening, if left for extended time periods. In this process, the smaller NPs with high surface energy break down and the material is redeposited on the larger NPs. This results in an increased average particle size and variation in particle size with a compensating lower count of NPs (Murray *et al.*, 2000). Therefore, through a

controlled and separated nucleation and growth phase and prevention of Ostwald ripening it is possible to produce monodisperse NPs.

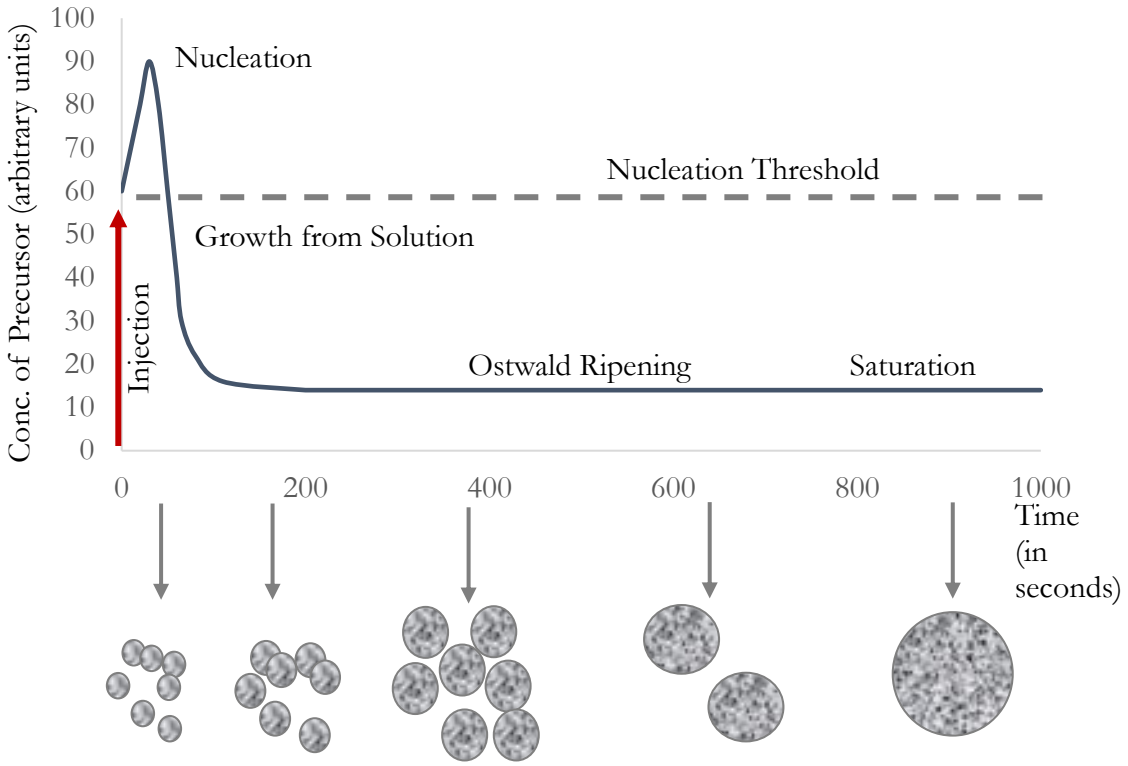

Figure 2.15: Schematic depicting stages of nucleation and growth for preparation of monodisperse NPs. Adapted from Murray et al., 2000.

2.2.1.2 Capping Agents to Prevent Agglomeration

During the preparation of NPs, stabilising agents or capping agents are introduced to prevent aggregation and precipitation of the NPs. Two modes of stabilisation have been distinguished (Bönnemann and Richards, 2001):

1. **Electrostatic stabilisation** which is based on Coulombic repulsion between ions adsorbed at the NP surface and the corresponding counterions. For example, gold sols prepared by the reduction of $[AuCl_4]^-$ with sodium citrate.
2. **Steric stabilisation** which is achieved by the coordination of sterically demanding organic molecules that form protective shields around the NPs. The main types of steric stabilisers are polymers; P, N, and S donors (e.g. amines); solvents such as MeOH and propylene carbonate; long-chain alcohols; surfactants; and organometallics.

For the metal sites to be active, the capping agent must be removed once the NPs are supported. As demonstrated in Kuhn *et al.*, 2009, PVP, TTAB and OA capping agents all decrease the metal surface for Pt activity in ethylene hydrogenation. Techniques for removing the capping agents depend on the individual catalyst design but in general high temperature calcination is used to break down the capping agent, leaving the active metal supported (Rioux, 2006, Li *et al.*, 2012, Niu and Li, 2014). More innovative techniques such as acetic acid washing and UV-Ozone irradiation

have also been recently investigated (Li *et al.*, 2012). Specific capping agent removal techniques will be discussed in **Section 2.2.1.4**.

2.2.1.3 Summary of Literature Resulting in Monodisperse Pt NPs between 1-3 nm

As the focus of this research is on producing monodisperse Pt NPs of small size (1-3 nm), only literature related to this goal is considered. Table 2.3 summarises some select examples of the available literature on Pt NPs synthesis. It is evident that there are several methods to synthesise Pt NPs of monodisperse size between 1-3 nm. Reduction of Pt salts such as H_2PtCl_6, $Pt(acac)_2$ and, K_2PtCl_4 in several solvents such as water, alcohols and ethylene glycol were seen. The capping agent is commonly added during synthesis, but some cases are seen where it is added after, such as in Wang *et al.*, 2000. Various capping agents can be used such as PVP, OCA, OA and more complicated structures such as dendrimers. It was clear that the major challenge in all synthesis procedures was the removal of the capping agent when supporting the Pt NPs for catalysis.

Table 2.3: Summary of Selected Literature Sources on Monodisperse Pt NPs between 1-3 nm

Reference	**Method**		**Product State**	**Average Size and Distribution (nm)**
(Teranishi *et al.*, 1999)	Reduction of H_2PtCl_6 in an alcohol and water solution refluxed for 3 hours in the presence of **PVP.**		Colloidal Pt NPs capped in PVP in aqueous solution.	Before PT: ~1.9; After PT: Not appplicable[1]
(Wang *et al.*, 2000) PVP: (Rioux *et al.*, 2006, Song *et al.*, 2006) OCA: (Kim *et al.*, 2013)	Reduction of H_2PtCl_6 in NaOH and EG at 160 °C for 3 hours.	Not capped.	Colloidal Pt NP solution in EG.	Average: 1.3; Range: 1-2
		Capped in **PVP**. Ox/red pre-treatment after supporting.	Pt NPs cleaned and supported on SBA-15 Silica.	Before PT: 1.73±0.26; After PT ~3 to 4
		Capped in **OCA**. Ox/red cyclic pre-treatment after supporting.	Pt NPs cleaned and supported on HZSM-5.	Before PT: 1.4±0.3; After PT: 3.2±0.7
(Liu *et al.*, 2007)	Reduction of $Pt(acac)_2$ in 1,2-hexadecanediol and diphenylether under reflux at 110 °C in the presence of **OA**.		PtNPs supported on XC-72 carbon powder.	After PT: 3.6±0.6
(Huang *et al.*, 2008, Kuhn *et al.,* 2008, Scott *et al.*, 2005)	K_2PtCl_4, methanol and water were mixed with **4th Gen PAMAM** dendrimer solution. $NaBH_4$ was then added with vigorous stirring at RT for 3 hours. Mild pre-treatment after supporting.		PtNPs supported on SBA-15.	Before PT: ~1.0±0.3 After PT: ~1 (dendrimer not removed) After Pt: ~ 3 to 4

[1] No pre-treatment conducted

In general, the NPs increase in size after high temperature pre-treatments are used to remove the capping agents. The increase in size is attributed to sintering, which can be described as crystal growth caused by the migration of nearby crystallites. The mobility of the metal phase is greatly

enhanced when in liquid state which occurs at elevated temperature. It should be highlighted that in some literature sources, especially those which compare particle size effects in reactions, the Pt NPs size before pre-treatment are stated for comparison (Rioux *et al.*, 2006). In this study, the NP sizes after pre-treatment will be investigated and reported to get a clearer indication of the actual NP size during catalysis.

Comparing capping agents, dendrimer synthesis methods produce smaller Pt NPs than other known capping agents, such as PVP. However, removal of the dendrimer template often causes NP aggregation. In some cases, it may be possible to keep the dendrimer template intact during reaction, as is seen in Haung *et al.*, 2008, which is made possible by supporting the dendrimers inside a SBA-15 structure. However, this is not suitable for supporting in MFI due to size constraints. Alternatively, PVP is a commonly used capping agent but has been documented as difficult to remove and high temperature pre-treatments cause the final Pt NPs to sinter (Rioux *et al.*, 2005). Otherwise, OCA and OA are both amine based capping agents which require a slightly less harsh pre-treatment but they were found to poison the Pt NPs and cause deactivation during catalysis if not properly removed (Kuhn *et al.*, 2009, Kim *et al.*, 2013). In general, it is seen that regardless of the capping agent, the pre-treatment results in NPs with an average diameter of at least ~3 nm. It is notable that the OCA final NPs (after pre-treatment) are closer to the required particle size than all other synthesis methods reviewed.

2.2.1.4 "Uncapped" Pt NPs via a Modified Polyol Process

From the numerous synthesis methods to produce monodisperse Pt NPs in the size range of 1-3 nm (as seen in Table 2.3), the method originating from Wang *et al.*, 2000 is chosen to refine this research. This method is the synthesis of "uncapped" Pt NPs in 1,2-ethanediol (EG) via a modified polyol process. This method is chosen, firstly, due to the simple nature of the synthesis procedure (basic glassware and available chemicals) and secondly, because the uncapped NPs can form various protected metal NPs with the same metal core. This is particularly important as placing NPs on MFI is a largely unexplored research area and a flexible synthesis procedure is preferable.

Chemistry Behind the Modified Polyol Process

In the work by Wang *et al.*, 2000, EG is used as the organic solvent in this polyol process. The polyol process is termed 'modified' since the metal salt is only reduced once it has been transformed into a hydroxide/oxide colloidal solution using NaOH. The following overall chemical equation describes the preparation procedure:

$$H_2PtCl_6 \xrightarrow[(2)\ 160\ ℃,\ inert\ gas\ flow]{(1)\ NaOH,\ pH>12\ in\ EG} "unprotected" Pt\ NPs \qquad \text{Equation 2.4}$$

In an inert environment, a glycol solution of NaOH (50 mL, 0.5M) was added into a glycol solution of $H_2PtCl_6.6H_2O$ (1.0 g, 1.93 mmol in 50 mL) with stirring. A transparent yellow Pt hydroxide or oxide colloidal solution is formed and then heated at 160 °C for 3 hours. A transparent dark-brown homogenous colloidal solution was obtained (Wang *et al.*, 2000).

Figure 2.16 shows a TEM image of the Pt hydroxide solution in EG before reduction. Clearly Pt hydroxide NPs are visible with an average size of 4 nm.

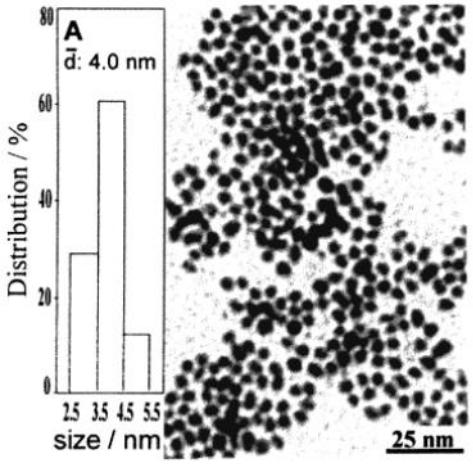

Figure 2.16: TEM image of a Pt hydroxide solution. Taken from Wang et al., 2000.

Further details on the chemical reaction steps after the Pt (hydr)oxide solution has formed are not given directly in the paper and were investigated to better understand the nature of the synthesis. Starting with polyol chemistry (Fiévet and Brayner, 2013):

The polyol process describes the synthesis of metal containing compounds in polyols such as polyhydric alcohols (e.g. ethylene glycol and propylene glycol) or etherglycols [e.g. di(ethylene glycol) or tri(ethylene glycol)]. Polyols are interesting among non-aqueous solvents due to their ability to act both as a solvent and a reducing agent. Like H_2O and monoalcohols, polyols are hydrogen-bonded liquids with a high relative permittivity (as seen in Table 2.4); therefore, to some extent they can dissolve ionic inorganic compounds (acting as the solvent). Polyols are also like monoalcohols, since they are mild reducing agents but with the added advantage of having high boiling points. This makes it possible to carry out reduction at temperatures up to 250 °C. Polyols are also coordinating solvents which form complexes with many metal cations. Therefore, the polyol can form reactive intermediates as well as adsorb onto the surface of the particles to prevent aggregation.

Table 2.4: Relative Permittivity and Boiling Point of some Polyols for Comparison with Water and Monoalcohols (Adapted from Fiévet and Brayner, 2013).

Solvents	**Water**	**Ethylene Glycol**	**Di(ethylene glycol)**	**Methanol**	**Ethanol**
ε_r	78.5	**38**	32	33	24
T_b (°C)	100	**198**	245	65	78.5

The formation of Pt NPs from EG has been assumed to follow the overall general scheme (Fievet *et al.*, 1989):

$$HOCH_2CH_2OH \rightarrow CH_3CHO + H_2O \qquad \text{Equation 2.5}$$

$$2CH_3CHO + M(OH)_2 \rightarrow CH_3 - CO - CO - CH_3 + 2H_2O + M \qquad \text{Equation 2.6}$$

First, dehydration of EG leads to the formation of acetaldehyde which is then oxidised to from Pt atoms and by-products. However, in more recent literature it has been suggested that the hydroxide ions take part in acetate ion formation which are said to stabilise the NPs in solution, as follows (Pomogailo and Dzhardimalieva, 2014):

$$2CH_3CHO + (PtCl_6)^{2-} + 6OH^- \rightarrow 2CH_3COO^- + Pt + 6Cl^- + 4H_2O \qquad \text{Equation 2.7}$$

This adjusted mechanism is in agreement with the descriptions by Fiévet and Brayner, 2013, which explains that the polyols can form reactive intermediates to prevent aggregation of the NPs. Therefore, this scheme is most likely a more accurate description of the actual chemistry.

Results for Pt NPs Synthesised by the Modified Polyol Process

The first NPs in EG were analysed using various characterisation techniques to assess the size and nature of the particles produced (Wang *et al.*, 2000). *Figure 2.17* (a) shows an edited TEM image with a particle size distribution histogram of 300 particles. *Figure 2.17* (b) shows the resultant XRD pattern of the same particles.

It is clear to see from the TEM results that the particles are relatively monodisperse, ranging from 0.8 – 2 nm, with an average diameter of 1.3 nm. The XRD pattern shows diffraction lines at (111), (200), (220), and (311) which corresponds with metallic Pt with a fcc crystal structure (McClune, 1980). The particle size from the half width of (111) gives ~2 nm which agrees with the TEM results. It is expected that the particle size from XRD is bigger than TEM because the larger Pt particles will dominate the contribution to the diffraction signals. X-ray photoelectron spectroscopic (XPS) analyses were carried out on dried Pt NPs once removed from EG and washed several times (Wang *et al.*, 2000). The spectrum is similar to pure Pt metal and signals from O 1s and Cl 2p levels cannot be detected. The binding energies pf Pt $4f_{7/2}$ and $4f_{5/2}$ are 70.9 and 74.2 eV, respectively. These results (along with the XRD diffraction patterns) prove that the NPs have a valence state of metallic Pt and no platinum oxide exists (Seah *et al.*, 1983). It is therefore assumed in the replication of this method, that pure Pt metal NPs are produced. Rioux *et al.*, 2005 showed consistent results in a reproduction of the method, with TEM results showing monodisperse NPs with an average diameter of 1.7±0.26 nm and an XRD pattern of free-standing Pt NPs showing metallic Pt and an average particle size of ~1.7 nm. Furthermore, other replications of the Wang *et al.*, 2000 method have all shown similar results of small Pt NPs that are metallic in nature, confirming the reproducibility of the method (Kim *et al.*, 2013, Kunz *et al.*, 2014, An *et al.*, 2014, Wand *et al.*, 2016).

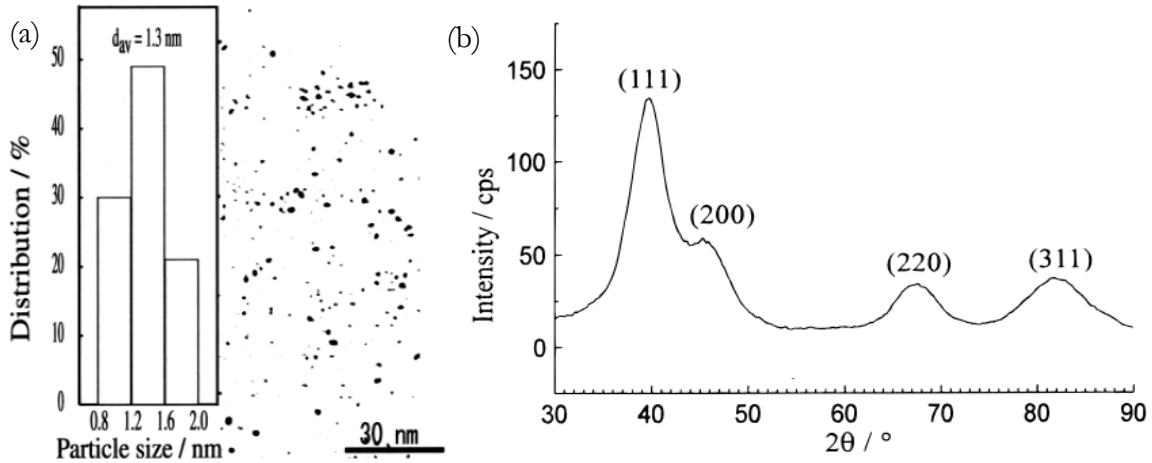

Figure 2.17: Uncapped NPs (a) TEM image and particle size distribution plot of NPs in EG (b) X-ray diffraction pattern of precipitated NPs. Taken from Wang et al., 2000.

Capping and Supporting Considerations for the "Uncapped" Pt NPs

As discussed in **Section 2.2.1.3**, many capping agents can be used and it was found after pre-treatment that some of the smallest NPs resulted from dendrimers, PVP and OCA capping agents. This study will explore PVP and OCA as potential capping agents for the purpose of placing NPs on MFI zeolites for two main reasons: (1) these methods are commonly used in literature and have shown numerous accounts of positive results (2) the chemicals are easily available and affordable. The molecular structures for the chosen capping agents are seen in *Figure 2.18*.

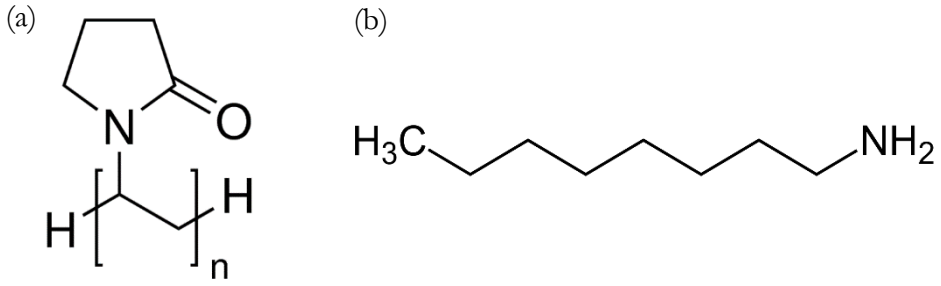

Figure 2.18: Molecular structure of (a) PVP and (b) OCA

PVP is a water-soluble polymer made from the monomer n-vinylpyrrolidone, as depicted in *Figure 2.18*. As mentioned earlier, it is a difficult capping agent to remove from the NPs and therefore, high temperature calcination is used to burn off the PVP. *Figure 2.19* shows an investigation into PVP decomposition by looking at varying temperature and gas flow pre-treatments (Rioux, 2006).

From *Figure 2.19* (a), it is evident that PVP decomposes in the presence of O_2 at elevated temperature (523 K). Furthermore, with a 10:1 mixture of PVP:Pt/SiO_2, ~90 % of the PVP decomposes within the first few hours. This shows that Pt, even as a physical mixture, catalyses the oxidative decomposition of PVP. However, in inert (He) and reducing (H_2) atmospheres the Pt does not have the same catalysing effect on PVP decomposition. In *Figure 2.19* (b), the PVP:Pt/SiO_2 sample shows a strong trend between temperature and PVP decomposition with the highest removal of ~90 % at 520 K. An NO_2 environment is also shown to be inappropriate for PVP decomposition, even though it has been shown to work for the removal of photoresist from Pt NPs. Therefore, this study shows that PVP decomposition should be conducted at high temperature in the presence of Pt and O_2 flow (Rioux, 2006). Furthermore, Rioux, 2006 found that the optimal pre-treatment conditions largely depend on PVP:Pt molar ratio and Pt particle size. In Rioux *et al.*, 2005, 1.7 nm Pt NPs in PVP supported on SBA-15 were calcined at 623 K for 12 hours with O_2 flow. The results showed high activation for ethylene hydrogenation suggesting adequate PVP removal. In synthesising Pt NPs, a series of pre-treatments will need to be conducted to find optimal conditions. The method by Rioux *et al.*, 2005 will be altered by increasing temperature and stay time.

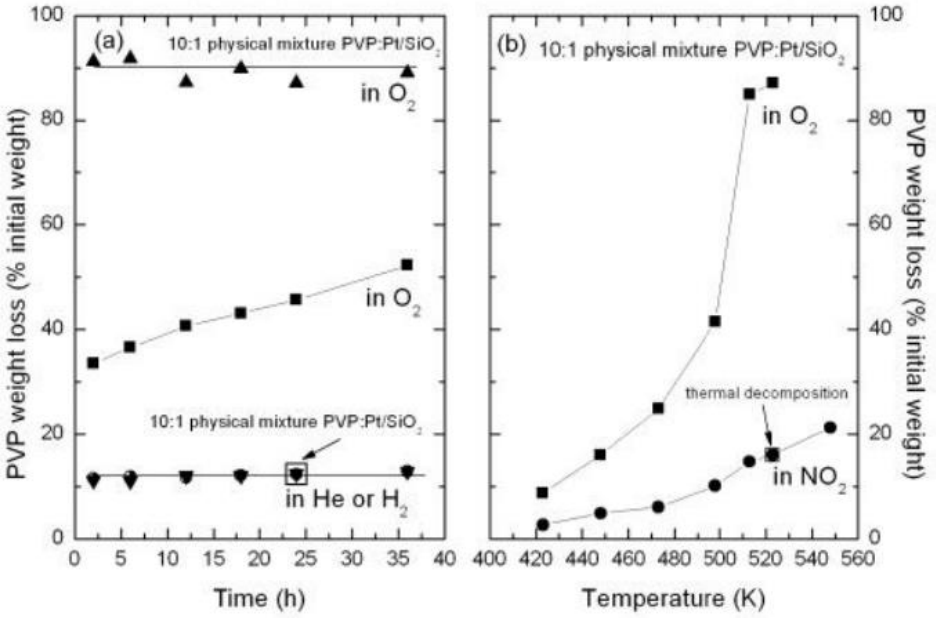

Figure 2.19: (a) Thermal decomposition at 523 K over time of free PVP (squares) and PVP:Pt/SiO2 mixtures (triangles) under O_2, He and H_2 (b) Influence of temperature on the thermal decomposition under O_2 (squares) and NO_2 (circles) flow. Taken from Rioux, 2006.

OCA is an amine-based capping agent as depicted in *Figure 2.18*. A standard oxidation/reduction pre-treatment is found to be inadequate to remove OCA, as depicted in *Figure 2.20* (Kuhn *et al.*, 2009). The effect of pre-treatment temperature was analysed by looking at ethylene hydrogenation activity. The pre-treatment consisted of an oxidation for 1 hour in 10% O_2/He and reduction for 1 hour in 10% H_2/He. It is evident that, regardless of pre-treatment temperature, catalyst deactivation was experienced after just three hours (dotted lines). It is suggested that this is caused by residual amine groups which are known poisons to Pt surfaces (Kuhn *et al.*, 2009).

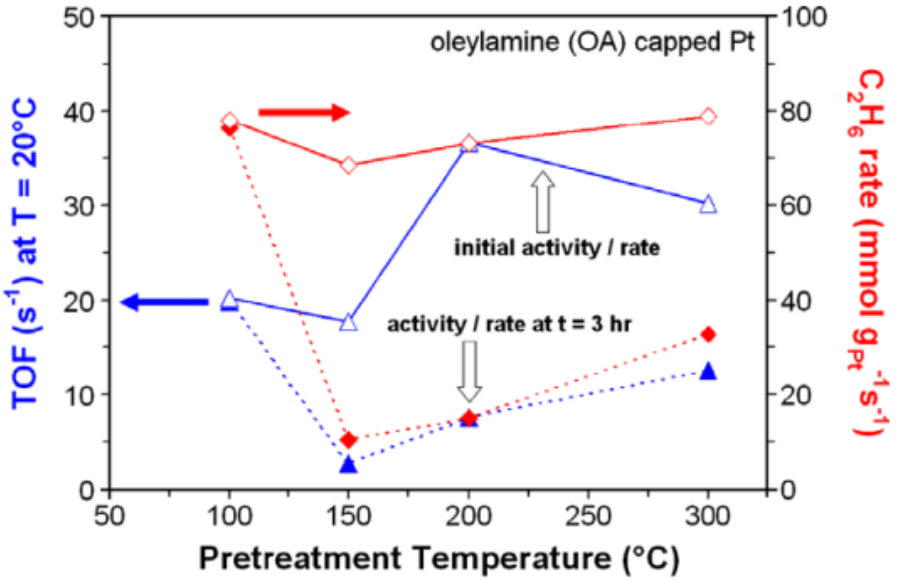

Figure 2.20: Ethylene hydrogenation activity over Pt/SBA-15 with OA capping. Reaction conditions: 10 Torr ethylene/100 Torr H_2/balance He at 1 atm, 20 °C. Taken from Kuhn et al., 2009.

However, after a cyclic pre-treatment by Kim *et al.*, 2013, The Pt NPs retained an average size below ~3 nm and the capping agent was successfully removed. The pre-treatment consisted of three cyclic oxidation and reduction steps at 573 K in O_2 and H_2 respectively. Successful removal of OCA is assumed as no loss in hydrocracking activity was observed. Furthermore, the chemisorption average particle diameter results (after pre-treatment) are consistent with the TEM particle size distributions, which confirms the removal of OCA. Since if the OCA had not been fully removed, the metal surface area from the chemisorption results would have skewed the average particle size result.

2.2.2 Organo-Metallic Chemical Vapour Deposition (OMCVD)

Another method explored to deposit Pt NPs on the outside of the support was OMCVD. This method has many advantages over wet synthesis methods as a 'one stage' process that avoids steps like pre-synthesis of NPs and catalyst pre-treatment. Furthermore, no capping agents are required which helps prevent contamination and active metal losses (Thurier and Doppelt, 2008).

2.2.2.1 Theory Behind OMCVD

The OMCVD method consists of vapourisation of the metal precursor at low temperature and reduced pressure to deposit a metal film on a substrate surface at higher temperature by adsorption and thermal decomposition of the precursor. The stages of the process are depicted in *Figure 2.21* (Thurier and Doppelt, 2008).

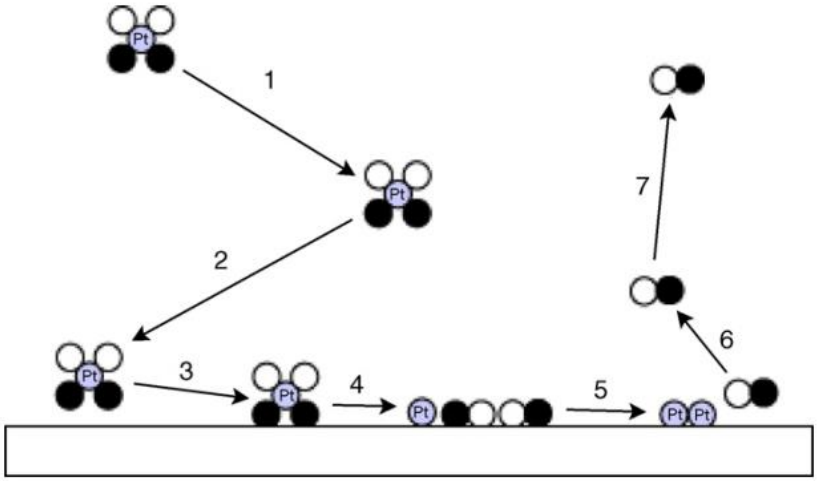

Figure 2.21: Stages of a traditional OMCVD process. Taken from Thurier and Doppelt, 2008.

Where,

1. Evaporation and convection of the gaseous reagents
2. Diffusion of reagents toward the substrate through the boundary layer
3. Adsorption of the reagents onto the substrate
4. Chemical reaction of the adsorbed species to produce a metal film of NPs
5. Desorption of by-products
6. Diffusion of the products through the boundary layer
7. Gas evacuation of the system to remove desorbed products

2.2.2.2 Choosing an Appropriate Precursor

In choosing an appropriate Pt precursor for the OMCVD synthesis several considerations must be addressed. The precursor needs to possess good volatility, an adequate stability window, low production cost, few impurities, fast nucleation, low risk handling (i.e. stability towards moisture exposure), and low toxicity. $Pt(acac)_2$ is one appropriate Pt precursor, with many advantages including: stability towards moisture and oxygen exposure and competitive pricing (Thurier and Doppelt, 2008). The molecular structure of $Pt(acac)_2$ can be seen in *Figure 2.22*. The Pt-O_{acac} bond (180 kJ/mol) is what decomposes to deposit the Pt metal NPs onto the substrate. It has been observed that the Pt-O_{acac} ligand decomposes without metal discoordination, giving a high metal purity (Thurier and Doppelt, 2008).

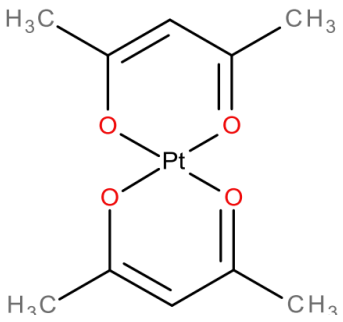

Figure 2.22: Molecular structure of $Pt(acac)_2$

2.2.2.3 Summary of Literature Results

Work at the University of Cape Town on OMCVD using $Pt(acac)_2$ has shown promising results of small Pt NPs which are well dispersed on carbon supports (Taylor, 2013, Jackson, 2014). *Figure 2.23* shows the particle size distributions of different Pt NP batches after OMCVD at varying reactor temperatures from Jackson., 2014.

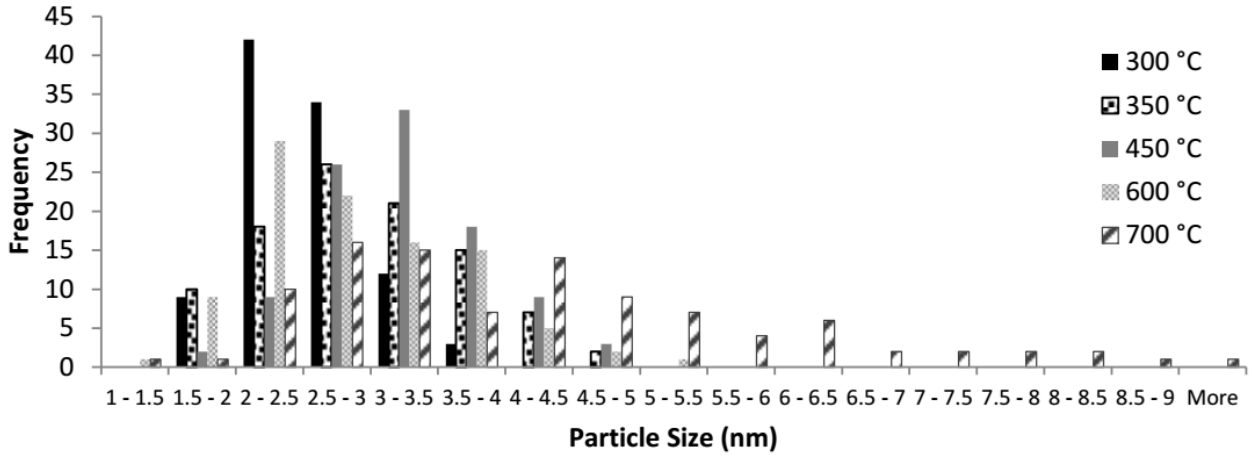

Figure 2.23: Particle size distributions from OMCVD with varying reactor temperatures. Taken from Jackson., 2014.

Evidently, at 300 ºC the smallest Pt NP particle size distribution is seen between 1-3 nm. The main advantage of OMCVD is that there is no capping agent to be removed so the particle size after synthesis will not change.

2.3 PLACING METAL INSIDE MFI MICROPORES

Placing metal inside the micropores was investigated and two common techniques can be used. The first is impregnation which achieves good overall dispersion but there is no control regarding

metal placement. Then second is ion exchange which uses a chemical reaction to selectively place the active component.

2.3.1 Incipient Wetness Impregnation

Impregnation is a commonly used method for placing metal on a support due to its simplicity. The main advantages of impregnation are simplicity of the method including basic equipment. This also makes scaling up easy as large volumes can be prepared with minimal additional effort. Impregnation can work with any porous material and metal salt combination, provided that the solvent is compatible. The disadvantages are that the technique does not allow control of the metal dispersion on the support. The calcination and activation step also often lead to particle agglomeration (Rioux, 2006).

2.3.1.1 Theory Behind IWI

The catalyst precursor in solution is contacted with the porous support by simply mixing them together. The solvent is then removed by evaporation leaving the catalyst precursor on the support. IWI uses a measured volume of precursor solution equivalent to the available pore volume. After impregnation, a calcination step is required where the newly formed catalyst is heated up to immobilise the catalyst precursor on the support. Followed by a catalyst activation step to get the metal into the catalytically active form (for example reduction in H_2) (van Steen., 2014).

2.3.1.2 Summary of Literature Results

IWI is the method used to disperse Pt NPs on MFI in Brosius *et al.*, 2016, as introduced in **Chapter 1**. $Pt(NH_3)_4(NO_3)_2$ in aqueous solution is used and the incipient wetness point is calculated to be 0.70 mL/g MFI. The pre-treatment consisted of slow calcination (0.3 °C/min) up to 350 °C in O_2 and reduction in H_2 at 225 °C for 8 hours. Pt NPs are found to be well dispersed, as seen in *Figure 1.2*, with an average size of 1.2 nm (calculated from CO chemisorption). However, metal location in the micropores is not easy to quantify as the Pt NPs after pre-treatment ranged from clusters to NPs up to 3 nm.

2.3.2 Competitive Ion Exchange

Competitive ion exchange (CIE) is a method used to ensure metal placement inside the pores through a chemical bond. The primary **advantage** of this method is greater control over the distribution of metal on the support with mostly molecular dispersion. The **disadvantage** is related to applicability, as only specific precursors and supports can be used (Rioux, 2006).

2.3.2.1 Theory Behind CIE

Ion exchange (IE) is a method where a chemical reaction between the surface of the support and the species in solution is used to disperse the active material. The chemical reaction can be induced by ligand exchange where the ligands surrounding the metal centre exchange with the support forming new support ligands. An example of the chemistry is seen in *Figure 2.24* were Au and Cu are exchanged on alumina (van Steen., 2014).

Competitive ion exchange (CIE) is a method where a competing ionic species in introduced to the system to encourage the exchange between the metal precursor and the support.

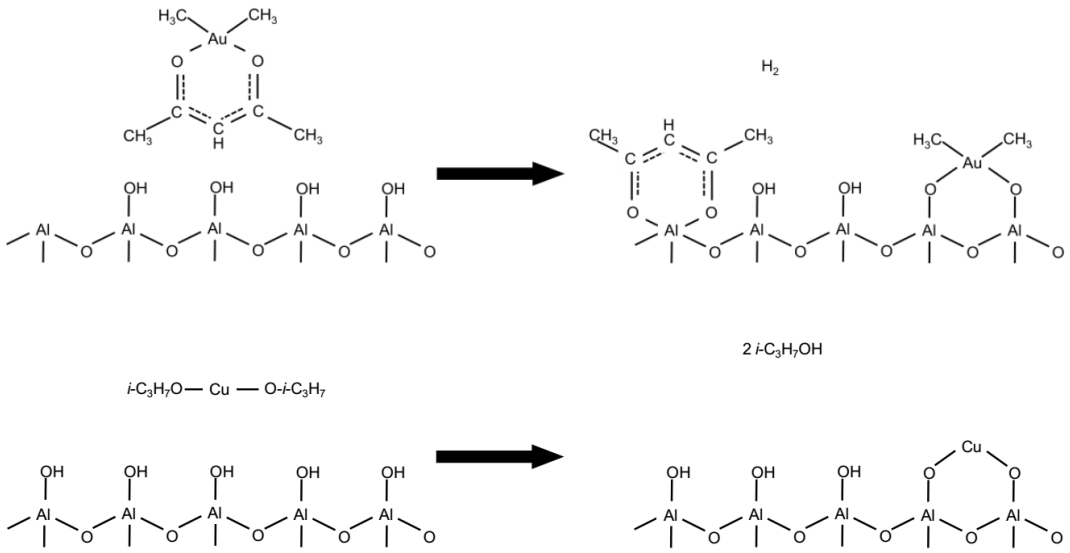

Figure 2.24: Ion exchange of metal complexes on an alumina support. Taken from van Steen., 2016.

2.3.2.2 Summary of Literature Results

Philippaerts *et al.*, 2010 investigated the influence of Pt addition by impregnation, IE and CIE on **Pt/MFI**. It is found that CIE followed by calcination (e.g. 0.2 °C/min) up to 350 °C under O_2 flow and reduction up to 500 °C under H_2, achieved **Pt/MFI** with the best Pt distribution and smallest Pt clusters occluded in the zeolite structure. The CIE method used MFI in the Na form (Na-MFI) and $Pt(NH_3)Cl_2$ with Na competitor ions from the addition of NaCl. *Figure 2.25* shows the results for the **Pt-CIE/MFI** where small Pt clusters and NPs between 0.5 – 2.5 nm are situated within the MFI micropores. Some evidence of Pt NPs located near or at the surface were seen but in general there is significant evidence of NPs within the micropores. Therefore, as a method to place Pt NPs mostly inside the MFI micropores, CIE was found to achieve the best results.

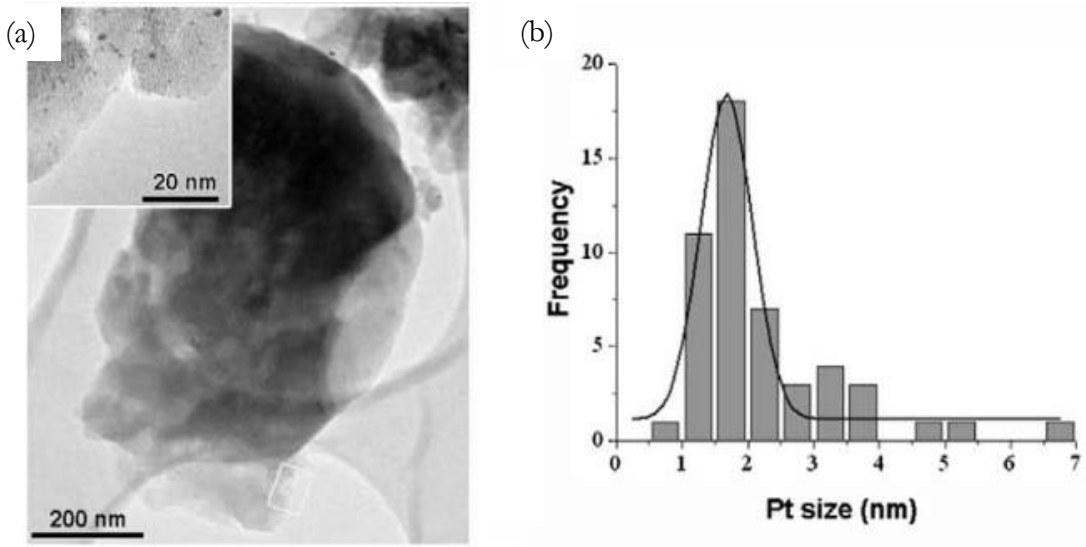

Figure 2.25: 0.5 wt.% Pt-CIE/HZSM-5 (a) BF-TEM images and (b) particle size distribution. Taken from Philippaerts et al., 2010.

Chapter 3

Research Approach

The previous chapter covered in detail how hydrocracking over Pt/MFI fits into the current hydrocracking landscape and investigated preparation methods to achieve exclusive metal placement inside and outside the micropores. This chapter will summarise the literature findings and then outline the refined aim which will be followed to conduct the research portion of this thesis.

3.1 SUMMARY OF FINDINGS FROM LITERATURE

The first part of the literature review compared MFI hydrocracking in the presence of H_2O with normal hydrocracking processes. Current hydrocracking theory and catalyst design were also reviewed:

In comparing the process conditions required for MFI hydrocracking with H_2O to other hydrocracking processes in industry, it is evident that the new process has the potential to reduce costs through milder process conditions. Looking in more detail at the mechanism behind bifunctional hydrocracking of long chain alkanes (such as n-C_{16}), it was found that the most accepted reaction mechanism consists of a (de)hydrogenation step and isomerisation/cracking steps. An important distinction is that the isomerisation and cracking steps are believed to occur in sequence. Ideal hydrocracking, which refers to a specific type of hydrocracking where the acid sites are limiting, is a good measure of hydrocracking which can achieve high middle distillate yields and process flexibility. Therefore, ideal hydrocracking will be pursued in this study as the optimal hydrocracking type to achieve high diesel yields. In choosing an optimal acid and metal function, it is evident that **Pt/ MFI** has many benefits in hydrocracking without impurities such as S and N. Pt has the most active (de)hydrogenation function and zeolites have strong acidic function. Focusing on the metal sites, the two main considerations are: metal and acid distance (metal location) and metal particle size. It was seen that diffusion limitations play a role depending on the acid/metal distance, but particle size should not affect ideal hydrocracking if there is a sufficient (de)hydrogenation function (as the acid sites are rate limiting).

Looking in more detail at hydrocracking over zeolites, zeolite Y (an industrially used hydrocracking catalyst) and zeolite HZSM-5 (not conventionally used) were compared. It was found that zeolite Y is less acidic (and therefore less active) but can achieve pure primary cracking, whereas zeolite

HZSM-5 is more acidic and produces over cracked products. Overcracking on HZSM-5 is attributed to strong adsorption of molecules on the acid sites and diffusion limitations of the longest fragments out of the narrow pores. MFI NSs were synthesised to reduce diffusion limitations and some improvements were seen in hydrocracking n-C_9 but the effects were marginal. Looking at product selectivity, zeolite Y is not shape selective but zeolite HZSM-5 only allows c-type β-scission inside the micropores (which produces linear primary cracking products). In the work by Brosius *et al.*, 2016, ideal hydrocracking over **Pt/MFI** was achieved for the first time by adding H_2O to the system, allowing for shape selective hydrocracking. It is important to note that only once ideal hydrocracking has been achieved can the catalysts be compared for differences in branching selectivity. Investigating the Pt metal sites in **Pt/MFI** in the presence of H_2O, it was found that metal location and dispersion affect the cracking steps and secondary isomerisation. This study will therefore attempt to quantify the metal location effects but keeping the overall active metal surface area as constant as possible (by controlling metal loading at >0.9 wt. % and keeping particle size consistent). Furthermore, metal location in relation to bulk MFI and NSs will also be explored.

The second part of the literature review deals directly with methods to place metal inside and outside the MFI micropores to investigate metal location effects:

Placing metal exclusively outside can be achieved by supporting pre-synthesised monodisperse Pt NPs on MFI. Through literature analysis it was found that a Pt salt reduction in EG is a suitable method to produce monodisperse Pt NPs between 1-3 nm through the careful control and separation of the nucleation and growth phase. This method also has the added benefit of being able to vary the capping agent which stabilises the NPs before contacting with the MFI support. Being able to vary the capping agent is advantageous as supporting Pt NPs on MFI is not widely researched and it is uncertain which capping agent will give the best results. PVP and OCA were chosen as suitable capping agents to be tested with varying pre-treatments to remove the capping agent after supporting. Another method for placing Pt NPs on MFI is through OMCVD which has the benefit of not needing a capping agent. However, it is expected that small Pt atoms and clusters might appear in the OMCVD method. In placing metal exclusively inside the micropores, a CIE method has shown to be effective where the Pt ions are exchanged into the MFI framework.

3.2 THE REFINED RESEARCH AIM

The revised aim of this study is therefore to quantify the extent that metal located inside or outside the micropores of MFI influences the cracking and isomerisation steps in the hydrocracking of n-C_{16} in the presence of H_2O.

It is hypothesised that placing metal inside the micropores will increase the yield of linear primary cracking products significantly in comparison to placing the metal outside the micropores. The two main reasons are that (1) the molecules need to react inside the micropores for type C β-scission selectivity and (2) when the metal sites are closer to the acid sites, a non-diffusion limited supply of dehydrogenated feed molecules are available to displace the primary cracked products preventing secondary isomerisation.

The objectives of this study are therefore to:

- Use varying metal addition techniques to place Pt NPs exclusively inside and outside the MFI micropores
- Characterise the catalysts to ensure Pt loading and size are consistent
- Subject the designed catalysts to hydrocracking in the absence and presence of H_2O to determine the effects of metal location on activity and selectivity
- Perform post-mortem characterisation on the catalysts to ensure no unexpected effects occurred during catalysis

Key questions:

1. Can primary cracking in the presence of H_2O be maintained when varying Pt location?
2. In placing Pt inside and outside, can the average particle size after pre-treatment be kept in the range of 1-3 nm?
3. Can the capping agent be properly removed when preparing pre-synthesised Pt NPs on MFI?

Chapter 4

Experimental

From the previous chapter, the research approach was structured in line with the overall research objectives. The approach is three-fold, including: catalyst preparation and characterisation with focus on metal site location (Pt NP synthesis, OMCVD and CIE are explored); catalytic performance determination, and post-mortem catalyst characterisation. In this chapter, the experimental methods used in the research will be described in detail including information on the chemicals and equipment used, the data collection processes, and the methods used to analyse the data.

4.1 PT NPS BY A WET COLLOIDAL SYNTHESIS

Small, monodisperse Pt NPs were synthesised using a simple reduction method of $H_2PtCl_6.6H_2O$ in EG, in the absence of a capping agent, which originates from Wang *et al.*, 2000. This method also allows for variation in the capping agent which is important in this research, as seen from the analysis in **Chapter 2**.

4.1.1 Apparatus and Chemicals

The simple apparatus used in the Pt NP colloidal solution synthesis was adapted from Murray *et al.*, 2000 and can be seen depicted in *Figure 4.1*.

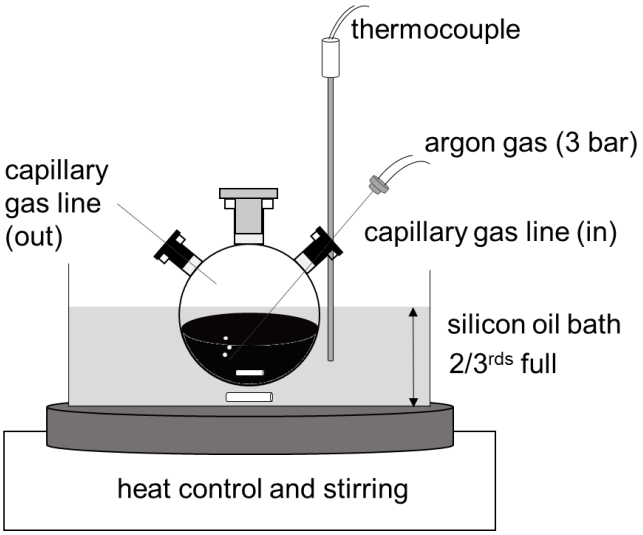

Figure 4.1: Diagram of experimental set-up for "uncapped" Pt NP by wet colloidal synthesis.

The reaction vessel was a three-necked round bottom flask, vertical, capacity 50 ml, joints: side necks 19/26 and centre neck 24/29, which was used consistently throughout all NP preparation. The centre neck was either blocked with a glass stopper or set-up for reflux (using a glass condenser) when using lighter boiling solvents. The side necks were fitted with rubber stoppers which were pierced with a syringe tip to insert the gas vent lines. A cut piece of GC column capillary (non-polar, CP-Sil, 5 CB, 0.15 mm ID, 2 μm thickness) was used for this purpose. The inlet capillary was connected to an Ar gas line which operates at 3 bar. The outlet capillary was open to the fume hood vent. The reaction vessel was lowered into a glass oil bath (filled up to $2/3^{rds}$ with silicon oil) which was heated and stirred by a Heidolph® (Mr Hei-End) magnetic stirring hotplate. The thermocouple was placed inside the oil bath as close as possible to the reaction solution without touching the round bottom flask wall. PTFE-coated polygon magnetic stir bars were used, a 10 mm x 6 mm inside the reaction vessel and a 30 mm x 6 mm under the reaction vessel in the oil bath, respectively. Stirring speed was set on the Heidolph® Mr Hei-End. A temperature calibration between the oil bath and the reacting EG solution showed that the oil bath had to be ~4 °C hotter than the required temperature in the reacting solution (See **Appendix A** for further details).

The following additional apparatus was used in the synthesis:

- Basic laboratory grade glassware, including beakers and sample vials
- Consumables, including weighing boats and transfer pipettes
- Pt NP colloidal solutions were stored in HDPE bottles and catalyst powders in glass vials
- Stainless steel spatulas and spoons
- PTFE-coated stir bars
- 50 ml glass separating funnel
- Glass graduated pipettes (1 ml and 5 ml) with a silicone bulb-type safety pipet filler
- Glass measuring cylinders (20 ml and 100 ml)
- Mettler Toledo® analytical balance (used for all solid weight measurements)
- Beckman Avanti® J-25 centrifuge with JA-20 rotor and JA-10 rotor and Beckmann centrifuge tubes (50 ml and 500 ml respectively)
- Grant® Ultrasonic bath
- n-C_{16} hydrocracking testing unit (as described in **Section 4.5.1**)

The chemicals used in the Pt NP synthesis are seen in Table 4.1, along with the supplier information.

Table 4.1: Pt NP Synthesis Chemicals Information

Chemical Name	**Linear Formula**	**Information**	**Supplier**
Chloroplatinic Acid Hydrate	$H_2PtCl_6.xH_2O$	Assay: ≥99.9% trace metals basis Composition: 37-40% Pt	Sigma-Aldrich Product Code: 520896
Ethylene Glycol	$HOCH_2CH_2OH$	Assay: 99%, Water: 0.2%, Acidity: 0.003%	Kimix Grade: AR
Silicon Oil	$[Si(CH_3)_2O]_n$	For oil baths Assay: min 99%	Kimix Code: M350

Sodium Hydroxide	NaOH	Assay: 97% Form: flakes	Kimix Grade: AR
Polyvinylpyrrolidone	$[C_6H_9NO]_n$	Form: powder Molecular weight: 40 000	Sigma-Aldrich Product Code: PVP40
Octylamine	$CH_3(CH_2)_7NH_2$	Assay: 99% Form: liquid	Sigma-Aldrich Product Code: O5802
H-MFI Zeolite (HZSM-5)	$Na_nAl_nSi_{96-n}O_{192}.16H_2O$	SiO_2/Al_2O_3 molar ratio: 90 Acid site density: 1.10E+20 sites/g Form: powder	Sud-Chemie (now Clariant)
Hydrochloric Acid	HCl	Concentration: 35-37%	Sigma-Aldrich Product Code: V800203 Grade: AR
Deionised Water	H_2O	Type 1 Water quality as described by ASTM®, ISO® 3696 and CLSI® norms, and to Purified Water as described in USP and EP	Merckmillipore
Ethanol	C_2H_5OH	Assay: 99.9% v/v Acidity: 9.18	Kimix Grade: Absolute
Silver Nitrate	$AgNO_3$	Assay≥99.0% Form: solid	Sigma-Aldrich Product Code:209139 Grade: ACS reagent
Argon	Ar	99.999% purity	Air Liquide

4.1.2 Typical Synthesis Procedure

In a typical preparation, 2.5 mL of 0.5 M NaOH in EG was added to the round bottom flask apparatus (seen in *Figure 4.1*) with Ar bubbling and stirring at 500 RPM. Keeping the stirring and bubbling conditions constant for the rest of the colloidal solution synthesis, 50 mg of $H_2PtCl_6.6H_2O$ in 2.5 mL of EG was then added (by briefly opening the glass stopper) and left for 10 minutes. A 5 mL graduated pipette was used for the volume measurements. The final mixture in the round bottom flask was lowered into the pre-heated oil bath at 160 °C (set to 164 °C on the Mr Hei-End hotplate) for 3 hours.

4.1.3 Capping, Supporting and Pre-treatment

The synthesised uncapped NPs stabilised in EG were then capped in PVP and OCA capping agents before being supported on MFI (bulk and NSs). Once supported, the capping agents were removed using a pre-treatment method to make the active metal surface available for catalysis, as discussed in detail in **Chapter 2**. The capping and pre-treatment procedures vary for the chosen capping agents as follows:

4.1.3.1 PVP Method

PVP protected NPs have been widely studied in many research groups and show excellent stability and catalytic properties for many organic reactions (Wang *et al.*, 2000). The method by Wang *et al.*, 2000 for PVP-capping was followed:

The 'unprotected' Pt NP colloidal solution in EG (5 mL) was precipitated by adding 0.83 mL of 2M HCl (measured with a 1 mL graduated pipette) and centrifuged for 20 minutes at 6000 RPM. The supernatant was discarded and the residue redispersed in ethanol with 10.2 mg of PVP. The solution was stirred for 10 minutes using a polygon magnetic stir bar (20 mm x 6 mm) at 300 RPM to allow for contact of the capping agent with the NPs.

The method by Rioux *et al.*, 2005 was followed for supporting the Pt NPs on MFI (**PtNPs-PVP/MFI**):

After ethanol evaporation, a Pt colloidal aqueous suspension was made by adding 32 ml of deionised water. The aqueous suspension was then further diluted with 80 ml ethanol and 48 ml of deionised water (all liquid measurements were done with a 100 mL measuring cylinder) before adding 1.2 g of MFI (to achieve 0.9 wt.% loading). The mixture was sonicated for 3 hours at room temperature and left overnight to stir using a polygon magnetic stir bar (20 mm x 6 mm) at 800 RPM. The resulting suspension was centrifuged at 7000 RPM for 15 minutes and the precipitate collected. Three washing steps were performed with a 1:1 mixture of water and ethanol with a total volume of ~50 mL. The cleaned product was then dried at room temperature overnight.

For complete PVP removal, an oxidation treatment was performed inside the trickle bed reactor. Various pre-treatments were tested to gauge the optimal conditions for PVP removal with a minimum sintering effect. Table 4.2 shows the pre-treatment methods tested.

Table 4.2: PtNPs-PVP/MFI Pre-Treatments

Oxidation	**Reduction**	**Reference**
120 ml/min O_2 at 0.2 °C/min to **350 °C**, hold for **60 mins**.	120 ml/min H_2 at 0.2 °C/min to 225 °C, hold for 480 mins.	Brosius *et al.*, 2016
120 ml/min O_2 at 0.2 °C/min to **350 °C**, hold for **720 mins**.		Brosius *et al.*, 2016 & Rioux *et al.*, 2005
120 ml/min O_2 at 0.2 °C/min to **250 °C**, hold for **720 mins**.		
120 ml/min **air** at 0.2 °C/min to **250 °C**, hold for **480 mins**.		

The pre-treatments were tested for their effect on particle size and ability to remove the capping agent, either in the reactor or using CO chemisorption with a replicated pre-treatment.

4.1.3.2 OCA Method

OCA capped Pt NPs have shown reduced sintering in the capping removal step when supported on MFI (**PtNPs-OCA/MFI**). The method by Kim *et al.*, 2013 was followed as described below:

The 'unprotected' Pt NP colloidal suspension in EG (5 mL) was mixed with 0.31 mL octylamine dissolved in 3.75 mL of toluene (measured using a 1 and 5 mL graduated pipette) using

a polygon magnetic stir bar (20 mm x 6 mm) at 300 RPM for 3 hours. In the separating funnel, 12.5 mL of ethanol was added to provide a homogenous colloidal suspension and then 12.5 mL of deionised water was added with shaking (measurements were done in a 20 mL measuring cylinder). The cloudy aqueous layer at the bottom was discarded by draining from the separating funnel, leaving the brown organic layer. 3.75 mL of ethanol was used to dilute 0.13 mL of 2 M HCl (measured using 1 and 5 mL graduated pipettes) before adding to the Pt NPs with shaking. The suspension was then washed with ~40 mL of deionised water. The washing step was repeated 3 times to remove excess OCA. 1.2 g of MFI was then added and stirred into the cleaned organic NP suspension with a Teflon coated spatula to achieve a Pt loading of 0.9 wt.%. The mixed catalyst powder was left overnight in a fume hood to evaporate the toluene.

The removal of OCA from **PtNPs-OCA/MFI** was attempted using a cyclic oxidation and reduction pre-treatment with inert gas flushing between each step at 300 °C, as seen in Kim *et al.*, 2013. The method was conducted before catalysis in the trickle bed reactor as follows:

1. Oxidation in 120 ml/min O_2 at 0.4 °C/min to 300 °C, hold for 60 mins
2. Reduction in 120 ml/min H_2 at 0.4 °C/min to 300 °C, hold for 30 mins
3. Oxidation in 120 ml/min O_2 at 0.4 °C/min to 300 °C, hold for 30 mins
4. Repeat Steps 2 and 3, three times in total

4.2 ORGANO-METALLIC CHEMICAL VAPOUR DEPOSITION

Another option for the synthesis of Pt NPs is through OMCVD of a Pt salt at temperature in an inert environment. The method by Jackson, 2015 was followed.

4.2.1 Apparatus and Chemicals

The synthesis was conducted in an experimental set-up developed by the HySA research group at the University of Cape Town. The set-up included a tubular furnace which housed a Haynes alloy reactor which is depicted in *Figure 4.2*.

Figure 4.2: Photograph of tubular reactor used for OMCVD. Taken from Jackson, 2015.

The catalyst sits in the middle tubing piece during reaction and is secured by fittings sealed with O-rings. The reactor was connected at one end to an Ar gas line. Additional apparatus used in this synthesis was as follows:

- Basic laboratory grade glassware, including beakers and sample vials
- Mettler Toledo® analytical balance (used for all solid weight measurements)
- Catalyst powders stored in glass vials
- Consumables, including weighing boats
- Stainless steel spatulas
- Grant® Ultrasonic bath

The chemicals used in the synthesis are listed in Table 4.3 with product and supplier information.

Table 4.3: Chemical Information for OMCVD Pt NP Synthesis

Chemical Name	**Linear Formula**	**Information**	**Supplier**
Platinum (II) acetylacetonate	$Pt(C_5H_7O_2)_2$	Assay: 97% Form: powder	Sigma-Aldrich
MFI Zeolite (ZSM-5)	$Na_nAl_nSi_{96-n}O_{192}.16H_2O$	SiO_2/Al_2O_3 molar ratio: 90 Acid site density: 1.10E+20 Form: powder	Sud-Chemie (now Clariant)
Argon	Ar	99.999% purity	Air Liquide

4.2.2 Typical Synthesis Procedure

A typical procedure for the preparation of Pt NPs on MFI by OMCVD (**PtNPs-OMCVD/MFI**) is described as follows (Jackson, 2015):

To achieve a metal loading of 0.9 wt%, 1.0 g of MFI was physically mixed with 18.3 mg of $Pt(acac)_2$. The physical solid mixture was sonicated for 30 minutes by clamping the sample (inside a sealed glass vial) in the ultrasonic bath. The catalyst powder was then funnelled into the reactor tube and the reactor was assembled using o-rings to seal either end. After tightening each side of the gas lines to the reactor tube with the appropriate spanners, the reactor assembly was placed into the tubular furnace and aligned so that the reactor tube was in the centre. The Ar gas line was connected to either end of the reactor assembly with the one end connected to the Ar gas bottle and the other end placed into a beaker of water. The Ar gas was opened and the flow checked by observing bubbles in the beaker of water. After insulating the reactor assembly (by fastening thick discs of insulation to the ends of the furnace openings) the temperature programme was set to heat to 100 °C with a ramp time of 30 minutes and a hold time of 30 minutes. Thereafter, the Ar gas flow was terminated and the temperature ramped to 320 °C in 60 minutes with a stay time of 60 minutes. After reaction, the reactor assembly was removed from the furnace to cool down for 12 hours before the catalyst was removed and stored in a glass vial.

4.2.3 Pre-treatment

Once the synthesis was completed, the Pt NPs are supported on MFI with no capping agent – meaning an oxidation pre-treatment is not needed. However, the standard reduction pre-treatment was conducted as follows: reduction in 120 ml/min H_2 at 0.4 °C/min to 300 °C, hold for 30 mins (Brosius *et al.*, 2016).

4.3 COMPETITIVE ION EXCHANGE

The ion exchange (IE) method uses a chemical interaction between the surface of the support and the metal species to achieve molecular dispersion inside the support. In the case of the Pt/MFI, competitive ion exchange (CIE) is used whereby a competing ionic species is introduced into the system to facilitate the exchange between the metal and support. The method from Philippaerts *et al.*, 2010 was reproduced as follows.

4.3.1 Apparatus and Chemicals

All IE's where done in a 500 mL Erlenmeyer flask. The solutions were mixed using a PTFE-coated egg-shaped magnetic stir bar (40 mm x 19 mm) and a Heidolph (Mr Hei-End) magnetic stirring hotplate. For washing cycles after synthesis, a pressurised filter press was used with Ar gas flow and filter paper. Plastic weighing boats and stainless-steel spatulas were used. A Mettler Toledo® analytical balance and glass measuring cylinders (100 and 500 mL) were used for solid and liquid measurement, respectively.

The chemicals used in this synthesis are summarised in Table 4.4 with supplier information.

Table 4.4: Competitive Ion Exchange Chemical Inventory

Chemical Name	**Linear Formula**	**Information**	**Supplier**
Tetrammine Platinum (II) Nitrate Solution	$Pt(NH_3)_4Cl_2$	Assay: 2.79% Form: liquid	Alfa Aesar Product Code: 180244
MFI Zeolite (H-MFI-90)	$Na_nAl_nSi_{96-n}O_{192}.16H_2O$	SiO_2/Al_2O_3 molar ratio: 90 Acid site density: 1.10E+20 Form: powder	Sud-Chemie (now Clariant)
Deionised Water	H_2O	Type 1 Water quality as described by ASTM®, ISO® 3696 and CLSI® norms, and to Purified Water as described in USP and EP	Merckmillipore
Silver Nitrate	$AgNO_3$	Assay≥99.0% Form: solid	Sigma-Aldrich Product Code:209139 Grade: ACS reagent

4.3.2 Typical Synthesis Procedure

Prior to loading the metal onto MFI, the zeolite was brought into the Na-form.

4.3.2.1 Transfer of H-MFI to Na-MFI

First, 5 g of MFI sample, was placed into an Erlenmeyer flask with a 500 mL aqueous ammonia solution (measured with a 500 mL measuring cylinder) of pH 10. After 1 hour, the MFI was recovered through filtration and washed until a pH of 10 was achieved in the washing liquid. The product formed was **NH_4-MFI**.

Secondly, 200 mL of 1 M NaCl solution per gram of NH_4-MFI was added to an Erlenmeyer flask. Therefore for 5 g of MFI, 1000 ml of 1 M NaCl was used (measured with a 500 mL measuring cylinder). The mixture was stirred overnight for 8 hours before being filtered and washed until chloride free (using 0.1 M $AgNO_3$ solution to check for chloride in the washing liquid). The recovered **Na-MFI** was placed back into the Erlenmeyer flask and the IE method repeated to ensure complete exchange, assuming no MFI losses occurred.

4.3.2.2 Competitive Ion Exchange

The Na-MFI was placed into an Erlenmeyer flask for the final exchange to **Pt-MFI**. The Pt ion-exchange was done in the presence of Na ions (as NaCl) using a Na/Pt atomic ratio of 25 and a total solution volume of 1 L (measurements were conducted with a 500 mL measuring cylinder). The recovered Pt ion exchanged into MFI (**Pt-CIE/MFI**) was filtered and washed until chloride free and then left to dry at room temperature.

4.3.3 Pre-treatment

The following pre-treatment was used (Brosius *et al.*, 2016):

1. Oxidation in 120 ml/min O_2 at 0.4 °C/min to 300 °C, hold for 60 mins
2. Reduction in 120 ml/min H_2 at 0.4 °C/min to 300 °C, hold for 30 mins

4.4 CHARACTERISATION TECHNIQUES

Various ex-situ characterisation techniques were used at each step in the catalyst synthesis and testing. To follow is a description of all the characterisation techniques (including descriptions of the equipment and procedures) used in this study.

4.4.1 Transmission Electron Microscopy

TEM imaging was primarily needed in this work for collecting information about Pt NP shape, size, and distribution on the support. The NPs were analysed before and after supporting, after pre-treatment, and after catalyst performance determination. Furthermore, synthesised MFI-nanosheets (NSs) were also imaged to assess size and structure of the individual sheets. Two microscopes at the University of Cape Town Centre for Imaging and Analysis were used: FEI/Tecnai F20 CRYO FEGTEM, operating at 200 kV and fitted with a Gatan Ultrascan 4000 CCD camera and FEI/Tecnai T20 TEM, operating at 200 kV (LaB6 emitter) and fitted with an embedded CCD camera.

A transmission electron microscope makes use of a high energy electron beam with uniform intensity which illuminates a thin specimen to obtain a two-dimensional projection of a three-dimensional structure. As the electrons travel through the specimen they are scattered by a variety of processes and *Figure 4.3* shows the different signals which are generated.

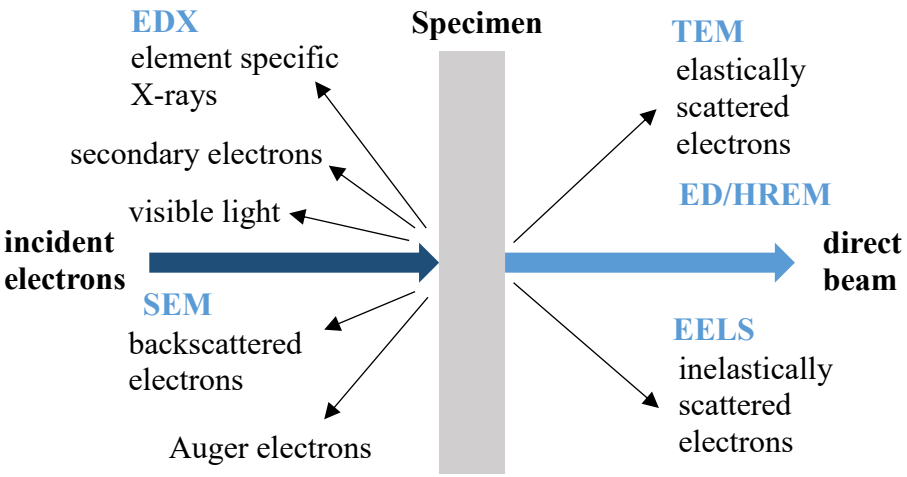

Figure 4.3: Signals generated from a high-energy beam of electrons when interacting with a specimen. Adapted from Williams and Carter, 2009.

The non-uniform distribution of electrons which emerge from the surface of the specimen is analysed during TEM and contains information about the structural and chemical properties. The conventional TEM image is a 'shadow image' of the scattered electrons which exit the specimen which will be varied in darkness depending on the density of the specimen (Williams and Carter, 2009).

4.4.1.1 Additional TEM Techniques Used

High-Angle Annular Dark-Field (HAADF) imaging was used to detect Pt clusters and atoms which can be masked in conventional TEM. The analysis was conducted at the Nelson Mandela Metropolitan University in Port Elizabeth by Prof. Patricia J Kooyman on a JEOL JEM-ARM200F double Cs-corrected TEM equipped with a FEG, a STEM unit and an HAADF detector, operated at 200 kV.

Annular apertures are used to select electrons which pass through a given symmetric zone within the objective lens of the microscope. In HAADF imaging, zones are selected where Rutherford scattering dominates the electron scattering. The electron scattering cross sections for this mechanism are proportional to atomic number (Z) and therefore the recorded signal amplifies chemical differences (Bals *et al.*, 2004).

Scanning Transmission Electron Microscopy – Bright Field (STEM-BF) was used in conjunction with the HAADF imaging to show a bright field contrast image. This analysis was conducted on the same apparatus as the HAADF imaging at NMMU by Prof. Patricia J Kooyman.

STEM combines the principles of TEM and SEM. Like TEM, STEM requires very thin samples and looks mostly at beam electrons transmitted by the sample. However, its main advantage over TEM is the use of other signals which cannot be spatially correlated in TEM (such as secondary electrons, scattered beam electrons, characteristic X-rays and electron energy loss). Like SEM, STEM scans a finely focused beam of electrons across the sample. Interactions between beam electrons and sample atoms generate a signal stream which is correlated with beam position to

build a virtual image. Its primary advantage over conventional SEM is improvement in spatial resolution (ThermoFischerScientific, 2017).

4.4.1.2 TEM Sample Preparation

Powder samples (wet grid): a small amount of sample on a spatula tip was added to a 1.5 mL Eppendorf® microtube with pure ethanol (~1 ml) and sonicated for 5 minutes. A plastic transfer pipette was then used to place 2 to 3 small drops of the sonicated suspension directly on the sample grid. The sample grids used for powder samples are copper grids with QUANTIFOIL® microgrid carbon film.

Powder samples (dry grid): A small amount of sample was ground down using a pestle and mortar to remove any visible clumps. The sample grid was then directly contacted with the powder sample and shaken off. A copper grid with QUANTIFOIL® microgrid carbon film was used.

Pt NPs in colloidal solution: the same method was followed as for powders except that the samples are not diluted with ethanol but rather directly dropped onto the sample grids. Copper grids with carbon film prepared at the UCT Electron Microscopy Unit were used.

4.4.1.3 TEM Image Analysis

ImageJ software (see **Appendix A** for more details) was used for measuring particle sizes from the TEM images. The particle diameters are collected by first measuring the scale bar (using the measuring tool) in each image and then inputting this distance into the 'set a scale' function. Thereafter, you can zoom in to areas of the TEM image and determine particle diameters using the set scale. 300 particle diameters were determined for each sample.

The particle diameter measurements for different particle synthesis batches were compared visually by plotting particle size distribution histograms. Two calculation methods can be used when plotting these: number-based and volume-based. A number-based technique uses the number of particles measured in different specified bin ranges, whereas a volume-based technique uses the calculated volume of particles in specific bin ranges (Bergeret *et al.*, 1997). For consistency, the number-based technique was used throughout this research as it is the most commonly encountered in literature. For a more quantitative comparison, statistical analysis was also used. Hypothesis testing, average and sample standard deviations calculations, and size distribution graphs were all determined from Microsoft Excel functions.

4.4.2 Inductively Coupled Plasma Optical Emission Spectrometry (ICP-OES)

ICP-OES was used in this research for the detection of Pt in the synthesised hydrocracking catalysts. The analysis was conducted by the UCT analytics lab with a Varian ICP-OES 730 Series with Spectra ICP 730 software.

The technique is based on the spontaneous emission of photons from atoms and ions which have been excited in a radiofrequency discharge. Liquid and gas samples are injected directly into the instrument where they are converted to an aerosol. This aerosol is directed into the central channel of the plasma, which is at very high temperature, where it is quickly vapourised. The sample

elements are liberated as free atoms and further collisional excitation promotes them to excited states (ionisation). *Figure 4.4* shows the states which the sample undergoes in the plasma.

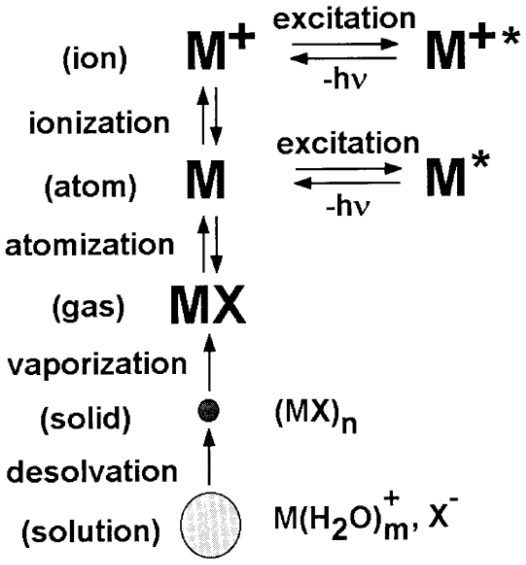

Figure 4.4: Process of sample droplet changing after contact with ICP discharge. Taken from Boss and Fredeen, 1999.

The atomic and ionic state species then relax by releasing a photon back to the ground state. The wavelengths of these photons are recorded and can be used to determine the elements in the sample, since photons have characteristic energies for each element. The total number of photons are also directly proportional to the concentration of the sample elements, allowing weight percentages to be determined after calibration (Hou and Jones, 2006).

4.4.2.1 ICP-OES Method

Solid samples (dried at room temperature in air) were first digested before analysis. 50 mg of a sample was weighed in an Xpress Teflon tube, before acids were added in the following order in the following quantities: 6 ml concentrated hydrochloric acid (12.1 M), 2 ml concentrated hydrofluoric acid (28.9 M), and 2 ml concentrated nitric acid (15.9 M). After 15 minutes of reaction time, the sample was placed inside a MARS-5 microwave digester for acid digestion. The digestion was conducted with a ramp time of 15 minutes to 180 °C and a hold time of 15 minutes.

For the analysis, a five-point calibration curve was used with standards as follows: 200 ppb, 500 ppb, 1000 ppb, 2000 ppb, and 5000 ppb. The standards were prepared from certified standards and are made up with 2% HNO_3. An internal standard solution of 10 ppm Yttrium solution from a certified standard was also prepared and made up with 2% HNO_3.

4.4.2.2 Data Analysis

To identify an element, the presence of characteristic wavelengths is investigated. In general, at least three spectral lines of the element must be confirmed. Obtaining quantitative data, for example the element concentration, is accomplished by using calibration curves – plots of emission

intensity versus concentration. Standard solutions are introduced into the ICP instrument and the intensity of the characteristic emission for the known element is measured. As different standards have different concentrations, it is possible to plot a straight-line graph of emission intensity versus known concentration. Therefore, when the emission intensity of a sample with unknown concentration is measured, the concentration can be calculated from the straight line calibration curve (Boss and Fredeen, 1999).

4.4.3 CO Chemisorption

CO chemisorption was used to determine the available metallic surface area for reaction of a supported catalyst. The instrument also allows for a simulated pre-treatment of the catalyst. This is important in the case of supported Pt NPs as the particle size can be determined after pre-treatment. This gives an indication of the degree of sintering and how successfully the capping agent has been removed with a pre-treatment by comparing the determined particle size from CO chemisorption and from TEM analysis. The analysis was conducted on a Micromeritics ASAP 2020C V2.01 G with oxygen, hydrogen, and helium gas flows.

In this CO chemisorption experiment, the dual isotherm method of Boudart and Benson., 1965 was implemented (where an isotherm refers to the plot of the gas adsorbed versus increasing pressure at a constant temperature). The method uses both physisorption and chemisorption to determine the irreversible gas uptake on the metal surface only, in a supported catalyst system such as **PtNPs/MFI**. The method works as follows:

First, a physisorption & chemisorption isotherm is recorded which amounts to adsorption on the metal and support. This is because physisorption is based on the weak interaction due to van der Waals forces which is experienced by all types of solids. The process is similar to a condensation process however, only a thin film (as indicated in *Figure 4.5)* can be formed as continuous growth of a liquid film is thermodynamically unfavourable. During an evacuation step the second isotherm is recorded and is a measure of the reversibly bound adsorbate which leaves the system (physisorption only isotherm). The third isotherm is then calculated as the difference of the two isotherms and is a measure of the chemisorbed gas which is left behind during the evacuation process. Chemisorption requires the formation of a chemical bond and is strongly dependent on the characteristics of the chemical reaction. Since chemisorption is a chemical reaction, only monolayer formation is allowed as seen in *Figure 4.5*. It is important to note that extrapolating the difference isotherm to zero pressure gives the most accurate volume of chemisorbed gas in the sample.

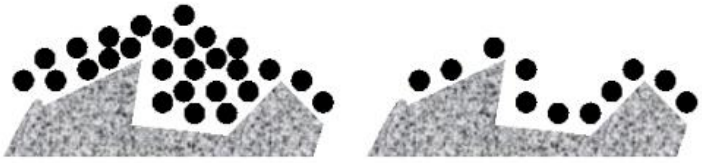

Physisorption **Chemisorption**

Figure 4.5: Schematic representation of physisorption and chemisorption. Taken from van Steen., 2014.

In a comparison between H_2, O_2 and CO chemisorption for Pt metal, CO is the most sensitive probe (Rioux, 2006). Therefore, only CO chemisorption is explored in this research. The reaction between CO and $Pt_{(solid)}$ has been assumed as seen in Equation 4.1 and is expected to hold for all particle sizes at sufficiently high pressure (Torr range) (Boudart and Djéga-Mariadassou, 2014, Rioux, 2006).

$$Pt_{solid} + CO \leftrightarrow CO - Pt_{solid} \qquad \text{Equation 4.1}$$

The stoichiometry is therefore 1:1 and was assumed in all calculations for dispersion and particle size as described in the data analysis section to follow.

4.4.3.1 Experimental Method

In a typical analysis, 0.25 g of the desired powder sample was weighed into a quartz U-tube with a plug of glass wool on either side. The U-tube was inserted into the apparatus. The sample was initially evacuated with helium backflow before starting the pre-treatment. Various oxidation and reduction pre-treatments were tested as outlined in the catalyst preparation sections (**Section 4.1 – 4.3**). The CO chemisorption conditions remained constant for every analysis. Table 4.5 shows a typical task summary of the full CO chemisorption experiment.

Table 4.5: CO Chemisorption Typical Task Summary

Step	Task	Gas	Temperature (°C)	Rate (°C/min)	Time (min)
Pre-treatment for PtNPs-PVP	Flow	O_2	350	0.4	60
	Evacuation	He	35	10	15
	Flow	H_2	225	0.4	60
	Evacuation	He	35	10	15
Analysis	Leak Test	He	35	10	-
	Evacuation	He	35	10	40
	Analysis	CO	35	10	-

4.4.3.2 Data Analysis

The difference isotherm is used to extrapolate the gas chemisorbed at zero pressure. This value is converted to a number of accessible surface atoms and this can be related to metal dispersion (the number of atoms at the surface over the total number of atoms). From metal dispersion, it is possible to determine an average hemispherical particle size. The dispersion (**D**) is calculated per 1 gram of catalyst sample as follows:

$$D = \frac{number\ of\ metal\ atoms\ at\ surface}{total\ number\ of\ metal\ atoms} = \frac{N_S}{N_T} \qquad \text{Equation 4.2}$$

Where,

$$N_S = V_{monolayer} \cdot \frac{N_A}{V_{mole}} \cdot F_S \qquad \text{Equation 4.3}$$

$$N_T = \frac{M_{\%}}{100 \cdot M_{Pt}} \cdot N_A \qquad \text{Equation 4.4}$$

The difference volume of gas adsorbed ($\mathbf{V_{monolayer}}$) is converted into metal surface atoms per gram catalyst to get $\mathbf{N_s}$, by using Avogadro's number ($\mathbf{N_A}$) of 6.022E+23 atoms/mole, the molar volume

of gas at STP ($\mathbf{V_{mole}}$) of 2.24E-02 m^3/mole, and the stoichiometry factor ($\mathbf{F_s}$) of 1:1. The total metal atoms per gram catalyst ($\mathbf{N_T}$) is calculated from the platinum loading ($\mathbf{M_{\%}}$) as wt.%/gram catalyst determined from ICP-OES, the molecular weight of Pt ($\mathbf{M_{Pt}}$) of 195.08 g/mole, and $\mathbf{N_A}$. The particle diameter can then be determined as follows:

$$d_p = \frac{f}{A_{Sm} \cdot \rho_{Pt}} \qquad \text{Equation 4.5}$$

Where,

$$A_{Sm} = \frac{\frac{A_{CS} \cdot N_S}{Pt\ wt.\%}}{100} \qquad \text{Equation 4.6}$$

A shape factor (**f**) of 6 is used for spherical particles and is related to the particle diameter through the overall surface metal area ($\mathbf{A_{Sm}}$) and Pt density, $\boldsymbol{\rho_{Pt}}$ (21.45 g/cm^3). $\mathbf{A_{Sm}}$ is calculated from the atomic cross-sectional area $\mathbf{A_{cs}}$ (0.0787 nm^2), $\mathbf{N_s}$ and $\mathbf{M_{\%}}$.

4.4.4 Ammonia Temperature Programmed Desorption (NH_3-TPD)

Zeolite acidity was quantified using NH_3-TPD. In the case of the **PtNPs-OCA/MFI**, this is particularly important as it is known that organic amines are a strong poison to acid sites (Kim *et al.*, 2013). Therefore, after supporting the **PtNPs-OCA** and simulating the pre-treatment in the instrument, NH_3-TPD was used to determine if the MFI acid sites have been compromised. The analysis was conducted on a MicroMeritics Autochem 2950 instrument. The instrument was used with He, O_2-He, NH_3-He and H_2-Ar gas flows.

TPD is a technique which studies gas desorption from a solid sample during programmed heating. A gas is first adsorbed onto the catalyst surface (in this case NH_3) and then the system is flushed before starting the TPD. As the catalyst is heated, the adsorbate is desorbed into the carrier gas stream and measured through a thermal conductivity detector. As the catalyst is heated, the rate of desorption increases, initially at an exponential rate before hitting a maximum point and then the desorption slows down to zero as all the gas is desorbed. The TPD spectrum obtained depends on several parameters, including the nature of the catalyst and surface coverage. Several peaks may occur if more than one desorption mechanism occurs or if there are different binding sites for a given species (Fadoni and Lucarelli, 1999). In the case of NH_3-TPD on MFI, information about the acidity can be determined as the ammonia reacts with the MFI support.

4.4.4.1 Experimental Method

A quartz U-tube was used to hold 0.3 g of zeolite sample. First a plug of quartz wool was inserted at the bottom of the tube followed by the powder sample. The U-tube was then inserted into the apparatus with the tip of the temperature probe sitting inside the sample. An example task summary can be seen detailed in Table 4.6.

Table 4.6: NH_3-TPD Task Summary

Step	Task	Gas	Temperature (°C)	Rate (°C/min)	Time (min)
Initial	Temperature Ramp	-	300	0.4	~ 720
	Evacuation	He	300	-	30
Pre-treatment for PtNPs-OCA	Flow	O_2-He	300	-	60
	Evacuation	He	300	-	30
	Flow	H_2-Ar	300	-	30
	Evacuation	He	300	-	30
	Flow	O_2-He	300	-	30
	Evacuation	He	300	-	30
	Flow	H_2-Ar	300	-	30
	Evacuation	He	300	-	30
	Flow	O_2-He	300	-	30
	Evacuation	He	300	-	30
	Flow	H_2-Ar	300	-	30
	Evacuation	He	300	-	30
Analysis	Temperature Ramp	-	100	25	~ 30
	Analysis	NH_3-He	100	-	30
	Evacuation	He	100	-	120
	Temperature Ramp	He	600	5	~ 100
	Evacuation & Cool	He	RT	-	-

4.4.4.2 Data Analysis

The NH_3-TPD results are compared against the tested samples to determine if the acid sites are affected. However, before this can be done a series of steps must be undergone to standardise the raw data set:

First the signal versus time data for the NH_3-TPD is split from the adsorption of NH_3 and desorption of physiosorbed NH_3 data. The signal data is then set back to start at zero by subtracting the average difference at the start of the TPD from all the data. The new data is then plotted and the baseline corrected so that the TPD starts and ends at zero. This is done by plotting a baseline curve and then using the equation to manipulate the data to have a baseline of $y = 0$. Lastly, the new signal data is plotted against temperature and then normalised per gram of sample by dividing by the sample mass.

4.5 CATALYST PERFORMANCE IN N-C_{16} HYDROCRACKING

The activity and selectivity of the synthesised catalysts will be assessed in the test reaction: n-C_{16} hydrocracking in the absence and presence of H_2O.

4.5.1 Apparatus

The n-C_{16} testing rig is made up of 4 trickle bed reactors which are configured into 2 identical testing units with 2 reactors in each unit. The annotated photograph (*Figure 4.6*) shows one of the testing units from the front and back view.

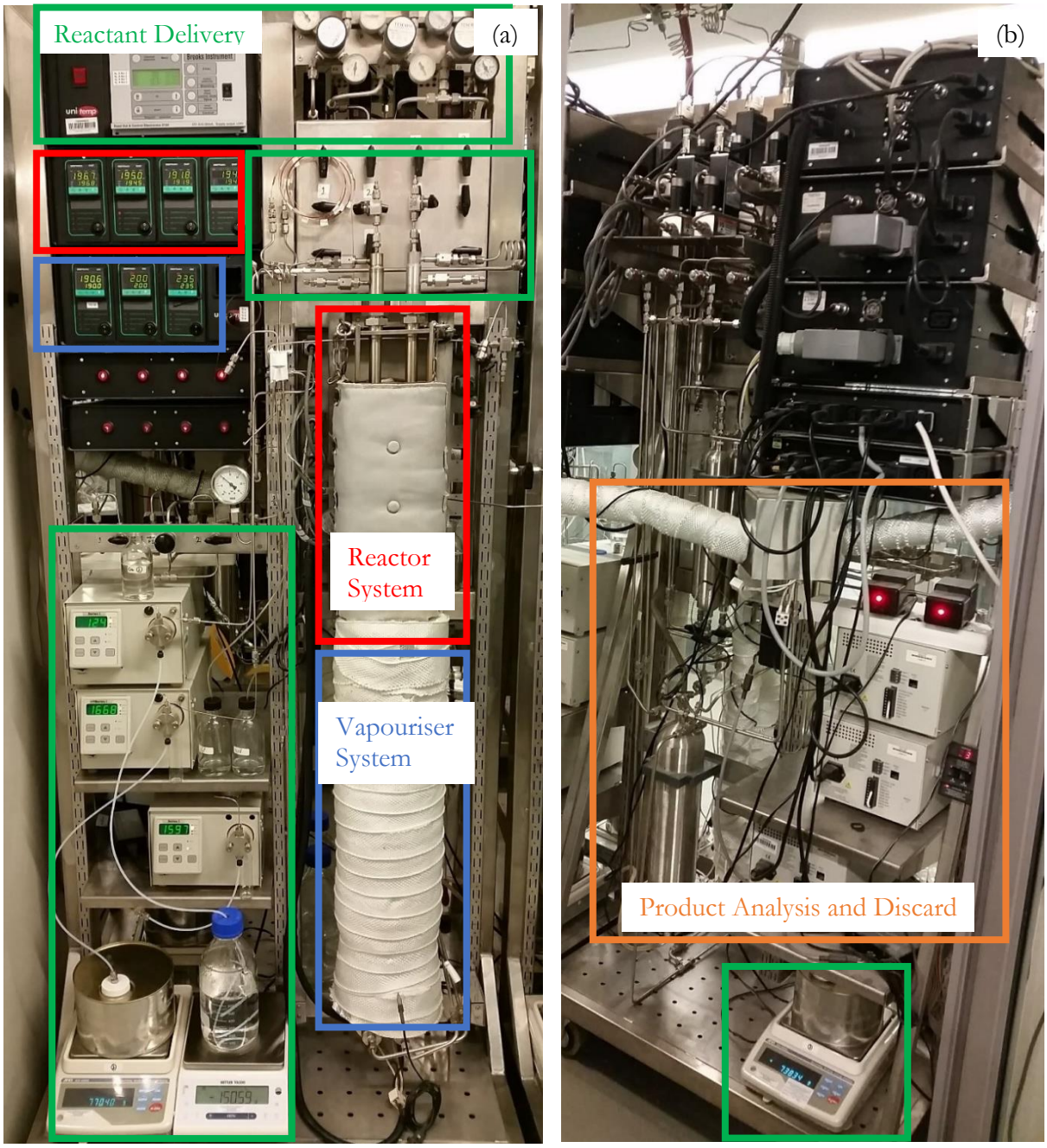

Figure 4.6: Photographs of n-C_{16} hydrocracking test unit (a) front view (b) back view.

Each testing unit can be broken down into 5 key areas: reactant delivery, reactor system, vapouriser system, product analysis and discard, and back pressure regulator. A process flow diagram showing the main streams and equipment is seen in *Figure 4.7* with the corresponding equipment list (Table 4.7). To follow is a description of how each key area operates.

Table 4.7: Equipment List for the n-C_{16} Hydrocracking Test Unit

Code	Name	Description
SV-101	Water Storage Vessel	Glass Schott bottle with plastic tube feed line
SV-102/3	n-C_{16} Storage Vessel	Metal drum with plastic tube feed line
MB-101 /2/3	Feed Vessel Mass Balance	4-digit open balance: METTLER TOLEDO ME Precision for H_2O feed and A&D GX-4000 for n-C_{16} feed
PX-101 /2/3	Feed Pump	LabAlliance™ Series I Pump
PR-101/2	Gas Pressure Regulator	TESCOM™ Pressure Regulator
CV-101/ 2/3/4	Mass Flow Control Valve	Brooks Mass Flow Controller
VX-101	2-Way Valve	Stainless steel
TV-101	3-Way Valve	Stainless steel
TR-101/2	Trickle-Flow Packed-Bed Reactor	> ¾ in. stainless steel tube with 16 mm ID, vertical orientation > Contains a metal grid and felt basket to hold the catalyst powder > Housed in a brass furnace with 4 temperature controlled heating zones using Gefran 800P and Gefran 600 PID heat controllers
EX-101/2	Packed-Bed Vapouriser	> ½ in. stainless steel tube, 10 mm ID, vertical orientation > N_2 dilution entry point (through DT-101) 5 cm below feed entry > Housed in a 25 mm diameter metal conduit wrapped in insulation using Gefran 600 PID heat controllers
DT-101	Dip-Tube	Stainless steel
NV-101/2	Needle Throttle Valve	Stainless steel
BR-101	Back Pressure Regulator	GO® BP-3 Adjustable back pressure regulator
CP-101/2/3/4	Catch Pot	Swagelok® DOT-3A 1800, 304L Stainless steel, 500 cm^3
MV-101	Mixing Vessel	Swagelok® DOT-3A 1800, 304L Stainless steel, 150 cm^3
SV-101	Selection Valve	VICI® 4 port
IV-101	Injection Valve	6 port 2-way
GC-101	Online Gas Chromatograph (GC)	> Varian CP-3900 equipped with a non-polar CP-Sil 5 CB (25 m, 0.15 mm ID, 2 μm thickness stationary phase) column and flame ionisation detector > H_2 carrier gas
RV-101/ 2/3/4	Pressure Relief Valve	Swagelok® R3A-C, purple spring
VC-101	Vent Catch Pot	Swagelok® DOT-3A 1800, 304L Stainless steel, 30 000 cm^3

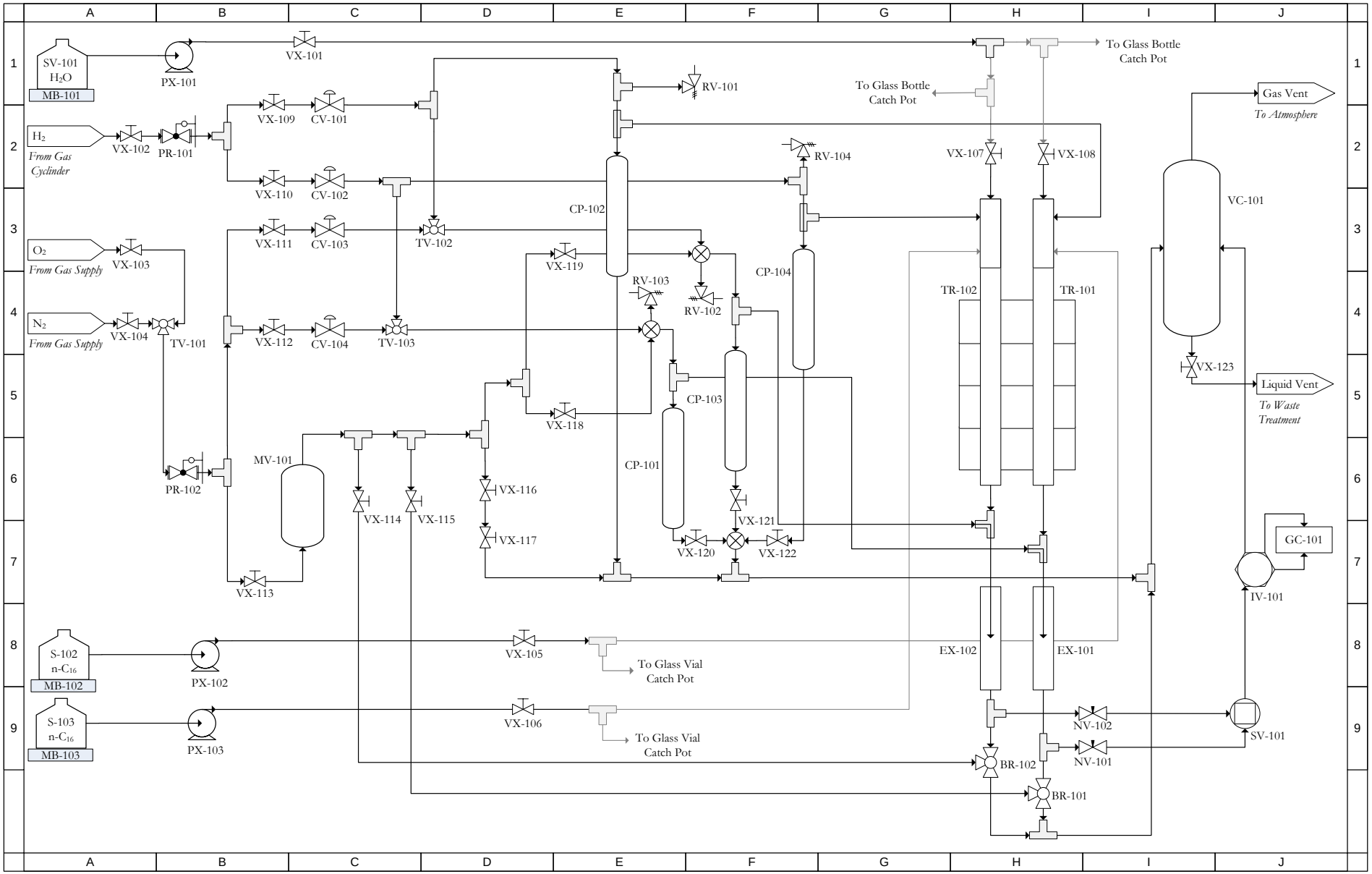

Figure 4.7: Process flow diagram of the n-C_{16} hydrocracking test unit.

Feed Delivery

The n-C_{16} rig receives both gaseous and liquid streams for operation. H_2 and N_2 gas, received from gas cylinders, is first de-pressurised (PR-101/2) before being supplied to the rig via mass flow control valves (CV-101/2). The H_2 gas enters each trickle-bed reactor (RT-101/2) from the gas injection point on the reactor head assembly, whereas the N_2 gas only enters the stream after the reactor (see vaporiser description). Pressure relief valves (RV-101/2/3/4) are installed in case of a pressure build-up and guard catch pots (CP-101/2/3/4) in case of liquid backflow from the reactor. The liquid reactant feeds (H_2O and n-C_{16}), are administered to the reactor (TR-101/2) from storage vessels (MB-101/2/3) with HPLC pumps (PX-101/2/3) through fused silica capillaries of 50 μm ID. Each liquid capillary line also has a split for a purge line. The liquid feed storage vessels are all placed on balances to monitor the mass balances throughout the runs.

Reactor

TR-101/2 is a trickle-flow packed-bed reactor where both gas and liquid phase reactants are present. The gas and liquid feeds entering the reactor are mixed in the heating zone which is in the top portion of the reactor. The catalyst powder is found below the heating zone, suspended in a catalyst basket, in the isothermal zone (which is approximately at the centre of the reactor). Refer to **Appendix A** for the reactor temperature profiles which show the zone classifications taken from Wynne *et al.*, 2013. The catalyst basket has a separate top and bottom, the bottom is made by hammering a square piece of grid and felt into the reactor using a 15 mm OD rod. The top part is another basket attached to a stainless steel coiled wire which is slid down the reactor tube using another rod which has a groove for the wire. Silicon carbide is packed both below and above the closed catalyst basket allowing for easy recovery of the catalyst powder after reaction.

Vapouriser

Each reactor is followed by a vapouriser (VX-101/2) to turn the mixed phase product stream into a completely vapour stream. The reactor product flows into the vapouriser where it spreads over silicon carbide packing before being diluted with N_2 gas, which enters through a dip-tube (DT-101/2). The vapouriser heats the product stream along its length at ~1.5 °C/cm from 175 °C to 250 °C (Brosius *et al.*, 2016). Silicon carbide fills VX-101/2 and creates a surface area for the liquid product to evaporate. The product stream is vapourised so that a purely gaseous stream can be sent to the gas chromatography apparatus for compositional analysis (see product analysis and discard description).

Product Analysis and Discard

The vapourised product stream leaves VX-101/2 and splits into a side stream which is used for product analysis and a main stream which goes to the back-pressure regulator (see back pressure regulator description). The side stream passes through a needle valve (NV-101) which reduces the stream to atmospheric pressure before entering a 4-port selection valve (SV-101) where all 4 reactor product streams connect. SV-101 allows for automatic sampling of a chosen reactor product whilst the other three reactor products are directed to a vent line. The chosen product

stream enters a 6-port 2-way injection valve (IV-101) which injects the sample into the GC for analysis.

Back Pressure Regulator

After the vapouriser, a back-pressure regulator (BR-101/2) is implemented on the main product gas line to keep the overall system at 20 bar during reaction. The back-pressure regulator keeps the inlet pressure below the set pressure by either opening, in the case of excess pressure, or closing, in the case where the pressure drops below the desired pressure. After BR-101/2, the product line is directed to the vent catch pot (VC-101). All vent lines pass through the vent catch pot where gas and liquid are separated – the gas then enters the main laboratory gas vent and the liquid is collected in the catch-pot and drained.

4.5.2 Operational Procedures

To explain the details of the reactor operation, the basic procedures required for a catalytic test are summarised.

4.5.2.1 Calibration

The following basic calibrations were conducted before the inception of this project to ensure accuracy in the flow measurements and product analysis:

- The mass controllers were calibrated to verify the flowrate readings. The calibration is done using a bubble meter which measures the rate of the gas flow at certain set points.
- The temperature controllers for the heating mantles were calibrated to account for differences between the set temperature and the actual temperature. The calibration is done using a temperature probe which is placed inside the reactor to measure the temperature.
- The GC apparatus was calibrated to ensure the correct detection of components at specific time on stream. This was achieved by running known mixtures through the GC and identifying the peaks.

4.5.2.2 Loading and Installing the Reactor

After cleaning the reactor tube with pressurised air and removing the reactor head assembly, dry catalyst powder was funnelled into the reactor tube. All catalyst powders were weighed using a 4-digit open balance. A plug of glass wool was pushed down into the reactor tube to rest on the catalyst powder without severe compression. The reactor basket was fed down into the reactor tube to hold the catalyst powder in place. Silicon carbide could then be funnelled into the top of the reactor until full. The reactor head assembly was re-installed with a new gasket via a Swagelok VCR fitting. The assembled reactor was then positioned inside the furnace block and connected via VCR-fittings to the respective lines using new gaskets. The order of connection was as follows: n-C_{16} line, gas line and gas dilution line at the bottom of the reactor. Copper compound paste was applied to the gas dilution line fitting for lubrication.

4.5.2.3 Catalyst Pre-treatment

Various pre-treatment methods were used in this research to activate the catalyst before testing performance in hydrocracking. A standard pre-treatment and cyclic pre-treatment were conducted as follows:

Standard Pre-treatment

For **oxidation**, the level in the O_2 tank was checked. Approximately 3.5 bar is lost during the standard pre-treatment and the cylinder pressure should never go below 10 bar. The O_2 flow was started by setting the 3-way valve (TV-101) and starting the flow on the mass flow controller screen. The catch pot valves VX-120 and VX-121 as well as the dilution valves (TV-102 and TV-103) were opened. The corresponding temperature programmes were then set for the 4 heating blocks. For **reduction**, after oxidation was finished and the O_2 flow stopped, the n-C_{16} lines were opened by removing the capping nut and tightening the actual line with a gasket. N_2 was used to flush the reactor for 1 hour to ensure all O_2 was removed. This was done by switching TV-103 and TV-102 to the N_2 line and then starting the flow by switching TV-101 and setting the flow on the MFC screen. H_2 flow was then introduced whilst N_2 was flowing for 10 minutes by switching VX-109 and VX-110 and setting the H_2 flow on the MFC screen. The N_2 flow was then terminated by stopping the flow on the MFC screen. Temperature programmes for the 4 heating blocks were set accordingly.

Cycling Pre-treatment

For the **OCA-NP**s, a series of oxidation/reduction cycles was needed for complete removal of the capping agent. One reactor unit was retrofitted for this purpose as seen in *Figure 4.8*.

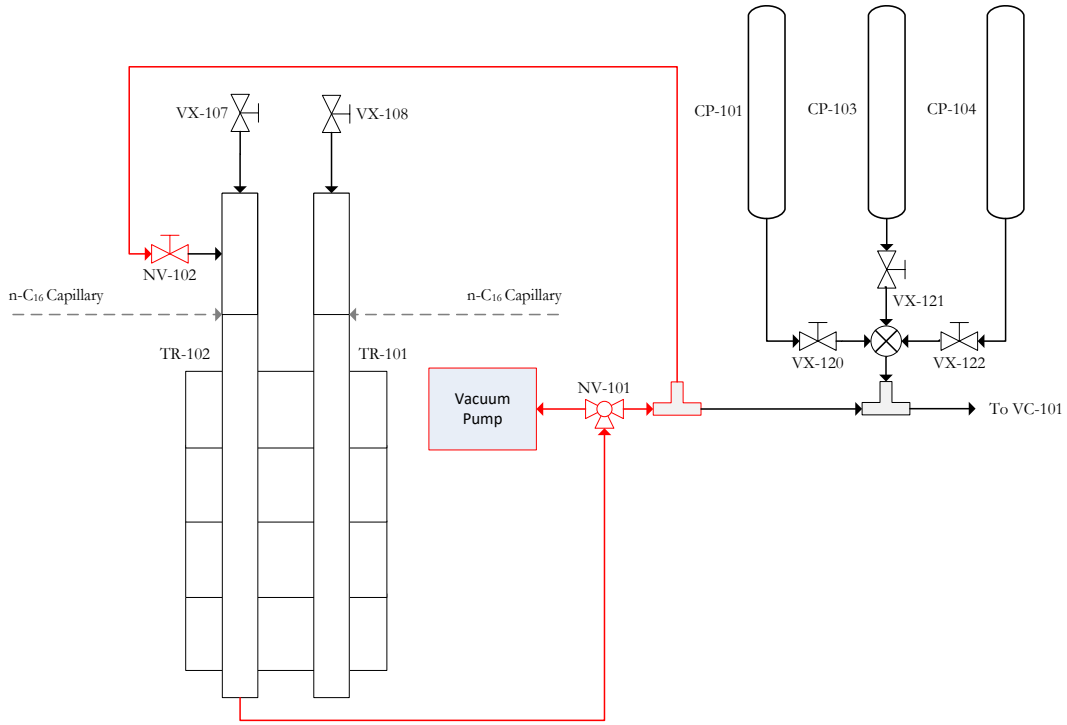

Figure 4.8: PFD of the retrofitted section for OCA cyclic pre-treatment.

Each step in the cyclic sequence was conducted for 30 minutes at a constant temperature of 300 °C. The procedure started with an evacuation step before reduction in H_2. The evacuation step requires valve NV-102 to be directed to the reactor bypass and valve NV-101 switched to the vacuum pump. Valve TV-101 was positioned for N_2 flow and the turbo pump switched on. Thereafter, the reduction step required NV-101 to be moved to the perpendicular position whilst NV-102 was switched to flow to the reactor. NV-101 was then switched toward the vent and the turbo pump switched off. In each step of the cycle, valve NV-101 was put in the perpendicular position before adjusting the reactor valve to prevent any disturbance on the catalyst bed. The H_2 flow was then set at 200 ml/min and the N_2 flow stopped. Another vacuum step followed with NV-101 switched to the vacuum pump and NV-102 to bypass before stopping the H_2 flow and starting the N_2 flow and switching on the turbo pump. The oxidation step was then started with NV-101 to vent and NV-102 to the reactor. The turbo pump was turned off and TV-101 switched from N_2 to O_2. The entire procedure was then repeated two times.

4.5.2.4 Start-Up Procedure

The start-up procedure was conducted once the catalyst pre-treatment was completed using the following steps:

1. Empty glass bottle and vial catch pots for each reactor
2. Drain the metal catch pot (VC-101)
3. Pressurise reactors to 20 bar: TV-102 and TV-103 are turned down, N_2 flow was set to 250 ml/min on the MFC screen. The n-C_{16} flow was set to 0.03 ml/min on the respective pump (which is sufficient to stop gas flow out of the reactor during pressurisation but not enough to flow into the reactor). The pressure was checked by turning VX-117 and checking the pressure gauge. Once the pressure reaches 20 bar wait 2 hours with regular checking.
4. Set the feed flowrates: the n-C_{16} flow rate was set by adjusting the pump to the appropriate flow and the H_2 flow was set by adjusting the flowrate on the MFC screen
5. Check the flowrate of the GC sample line with a bubble meter: unscrew the line which enters the metal catch pot (VC-101) and attach a bubble meter. Cycle through the GC sample switch options and assess each flowrate from each reactor in use. If needed, the flowrate can be adjusted using the needle valve (NV-101/2) at the bottom of the dilution unit for each reactor.
6. Start online GC sampling

4.5.2.5 Shut-down Procedure

After testing, the shut-down procedure was conducted as follows:

1. Stop online GC sampling
2. Reduce the reactor temperature blocks to room temperature
3. Turn off the n-C_{16} feed by switching off the pump and turning valves VX-105 and VX-106
4. Turn off the H_2 gas flow on the MFC screen
5. Depressurise the rig by slowly opening the needle valve (NV-101/2)

6. Leave N_2 flowing over night whilst rig cools down
7. Stop N_2 flow and remove reactor to recover catalyst powder

4.5.2.6 Daily Monitoring

Each day the follow steps were followed before changing settings on the reactors:

1. n-C_{16} mass balance and H_2O balance (if introduced) is conducted by measuring the glass bottle and vial catch pots as well as reading the balances for the feed pots.
2. The GC data is processed to determine the n-C_{16} conversion and C_4/C_{12} ratios (see **Section 4.5.3** for more details. Once the reactors have stabilised (with approximately 5 consistent runs) the conditions can be adjusted.
3. Change necessary settings for next testing point. The stabilisation period for new settings is ~12 hours.

4.5.2.7 Changing Settings

The following procedures were used to change settings during testing:

- **Temperature change:** when lowering the temperature on the reactor, adjust the set point manually on the temperature controllers. However, when increasing the temperature, a temperature programme is used which sets the new temperature with a ramp rate of 0.2 °C/min and a hold time of forever.
- **Introducing water:** H_2O is introduced by opening valve VX-101, VX-107 and VX-108 and then setting the appropriate flow rate on the pump and switching it on.

4.5.3 Product Stream Analysis

To assess the activity and selectivity of the catalysts, the product streams from the reactors must be accurately measured. In this study, an online GC analyses the product composition. Samples are taken directly from the reactor product (after vaporisation) at set intervals. The GC detects components as peaks on a time interval. The time it takes for a peak to appear dictates what the component is, and the area of the peak can be translated into a flowrate of the component found in the product.

4.5.3.1 Analysing the Gas Chromatograms

The peak area from the gas chromatogram is proportional to the number of fully reduced carbon atoms which can be represented by the equation below.

$$A \sim kN_c \qquad \text{Equation 4.7}$$

Where, A is the peak area from the chromatogram, **k** is a proportionality constant and $\mathbf{N_C}$ is the number of fully reduced carbon atoms. The proportionality constant is calculated by a calibration of the GC which was conducted before the start of this project. To calculate the proportional

flowrate ($\mathbf{F_A}$) of a specific product molecule, the total area under the peaks for molecule A (**Peak Area$_A$**) was divided by the number of carbon atoms in the specified molecule ($\mathbf{n_A}$).

$$F_A \sim \frac{Peak\ Area_A}{n_A} \qquad \text{Equation 4.8}$$

4.5.3.2 Performance Indicators

The performance of the catalysts is compared using the following main indicators:

Conversion

The conversion of a reactant can quantify the activity of a catalyst. The conversion rate of n-C_{16} can be calculated as follows:

$$X_{C_{16}} = 1 - \frac{F_{C_{16}}}{\sum_1^{16} F_{C_i}} \qquad \text{Equation 4.9}$$

Where, $\boldsymbol{F_{C_{16}}}$ is the flowrate of C_{16} in the product stream and $\sum_{\mathbf{1}}^{\mathbf{16}} \boldsymbol{F_{C_i}}$ is the total flowrate of C_i in the product stream (which is equivalent to the flowrate of n-C_{16} in the feed, $\boldsymbol{F_{C_{16},0}}$). In this research, the conversion was calculated directly from the GC integrated peak area results of the product stream using Equation 4.8, which simplified to:

$$X_{C_{16}} = 1 - \frac{A_{C_{16}}}{\sum_1^{16} A_{C_i}} \qquad \text{Equation 4.10}$$

Since, $\boldsymbol{A_{C_{16}}}$ is the total integrated area for C_{16} left in the product stream and $\sum_{\mathbf{1}}^{\mathbf{16}} \boldsymbol{A_{C_i}}$ is the total integrated area for the whole stream which is equivalent to $\boldsymbol{F_{C_{16},0}}$.

Intrinsic Rate of Reaction

The rate of reaction for heterogeneously catalysed reactions is defined as the amount of reactant converted per unit time per mass catalyst. For the intrinsic rate of reaction ($\mathbf{r_{C16}}$), the following equation can be used with the assumption that all sites are exposed to the same temperature and concentration (van Steen, 2014).

$$-r_{C_{16}} = \frac{F_{C_{16},0} - F_{C_{16}}}{m_{catalyst}} \qquad \text{Equation 4.11}$$

The converted formula was used in this research:

$$-r_{C_{16}} \left(\frac{mol}{g.s}\right) = \frac{F_{C_{16},0} \cdot X_{C_{16}}}{m_{catalyst}} \qquad \text{Equation 4.12}$$

Where $\boldsymbol{F_{C_{16},0}}$ was determined from the pump setpoint and converted into moles/s using a molar mass of 226.44 g/mol and density of 0.773 g/ml for n-C_{16}. The conversion ($\boldsymbol{X_{C_{16}}}$) was calculated as discussed above and the mass of the catalyst ($\mathbf{m_{catalyst}}$) was determined from measuring the dry weight of the catalyst before reaction using an analytical balance.

Turn-Over Frequency (TOF)

The turn-over frequency is an additional measure of catalytic activity which is defined as the number of molecules of reactant converted per unit time per active site. The TOF can be calculated using the intrinsic rate of reaction ($-r_A$) and the number of active sites ($\boldsymbol{N_{active\ sites}}$) per unit mass of catalyst ($\boldsymbol{m_{catalyst}}$) (van Steen, 2014).

$$T.O.F. = -r_{C_{16}} \cdot \frac{m_{catalyst}}{N_{active\ sites}} \qquad \text{Equation 4.13}$$

As the acid site is rate limiting in the bifunctional hydrocracking catalyst, $\boldsymbol{N_{active\ sites}}$ is determined from the acid site density of the MFI or NS support.

Activation Energy

The Arrhenius equation relates the activation energy ($\mathbf{E_a}$) to the intrinsic rate of reaction ($\boldsymbol{r_{C_{16}}}$), as follows:

$$\ln\left(r_{C_{16}}\right) = \ln(A) - \frac{E_a}{R} \cdot \left(\frac{1}{T}\right) \qquad \text{Equation 4.14}$$

Where **A** is the exponential factor, **T** is temperature in Kelvin, and **R** is the gas constant (8.314 J/mol.K). By plotting $\ln(\boldsymbol{r_{C_{16}}})$ versus $1/\mathbf{T}$ and fitting a linear trend line, the activation energy can be estimated from the gradient of the line.

C_4/C_{12} ratio

The extent of primary hydrocracking can be determined by plotting the C_4/C_{12} ratio. This was done using the integrated area under the C_4 and C_{12} chromatography peaks, and Equation 4.8, as follows.

$$\frac{F_{C_4}}{F_{C_{12}}} \sim \frac{\frac{A_{C_4}}{4}}{\frac{A_{C_{12}}}{12}} \qquad \text{Equation 4.15}$$

When re-arranging, it is evident that:

$$\frac{A_{C_4}}{A_{C_{12}}} \sim \frac{4F_{C_4}}{12F_{C_{12}}} \qquad \text{Equation 4.16}$$

In an ideal cracking scenario, each reactant molecule is cracked only once to form 2 products. Therefore, if n-C_{16} forms C_4 and C_{12} it has achieved primary cracking, any further cracking of the C_{12} molecule would be secondary cracking. Therefore, the flowrate of C_{12} product will be equal to C_4 product in ideal cracking. This leads to the following which can represent ideal hydrocracking:

$$\frac{A_{C_4}}{A_{C_{12}}} = \frac{4}{12} = 0.333 \qquad \text{Equation 4.17}$$

Selectivity

The selectivity of a reaction is defined as the amount of product formed relative to the amount of reactant converted (van Steen, 2014).

$$S_{C_i} = \frac{F_{C_i}}{\sum_1^{15} F_{C_i}}$$ Equation 4.18

In this work, the integrated peak areas were used since $A_i \sim nF_i$ (Equation 4.8). Which simplifies to:

$$S_{C_i} = \frac{A_{C_i}}{\sum_1^{15} A_{C_i}}$$ Equation 4.19

4.5.4 Summary of Hydrocracking Testing Conditions

For consistency, the catalyst testing conditions were replicated from Brosius *et al*, 2016 to directly compare results. An important requirement was that the trickle bed reactor operated under perfect plug flow. Where plug flow is defined as flow where no axial mixing is seen by good radial mixing. Meaning that species that enter the reactor spend the same amount of time in the vessel. Using the mass balance equation for a heterogeneous fixed bed reactor with ideal plug flow; which relates the reactant rate ($\mathbf{-r_{C16}}$) to a change in flow rate, the change in catalyst weight (as described in **Section 4.5.3.2**), and a first order apparent rate constant gives:

$$X_{n-C_{16}} = 1 - e^{-k\left(\frac{W}{F}\right)}$$ Equation 4.20

$$-\ln\left(1 - X_{n-C_{16}}\right) = k\frac{W}{F}$$ Equation 4.21

The derived equations were used in a set of experiments by Brosius *et al*, 2016 to assess the conditions at which ideal plug flow is actually achieved. Hydrocracking over **Pt/MFI** at various space times and different weights of catalyst were conducted and the results can be seen in *Figure 4.9*. From *Figure 4.9* (a) it is evident that when catalyst weights above 2 grams were used, the reaction rates decreased, whereas at 1 and 2 grams the reaction rates were identical. This finding suggests a change in reaction rate and *Figure 4.9* (b) confirms this by plotting W/F versus $-\ln(1-\mathbf{X}_{n\text{-}C16})$. As can be seen from 1 and 2 grams, the **k** value is consistent with ideal plug flow and first-order rate kinetics, whereas above 2 grams deviation is seen. Another important observation was that the activation energies remained constant at ~150 kJ/mol regardless of catalyst weight. In the event of external diffusion limitations, the activation energy was calculated to be no higher than ~21 kJ/mol (Le Page, 1988). Therefore, external diffusion limitations are not seen within the experimental conditions used.

Henceforth, the experiments were always conducted with at most 1 g of catalyst powder to ensure ideal plug flow behaviour.

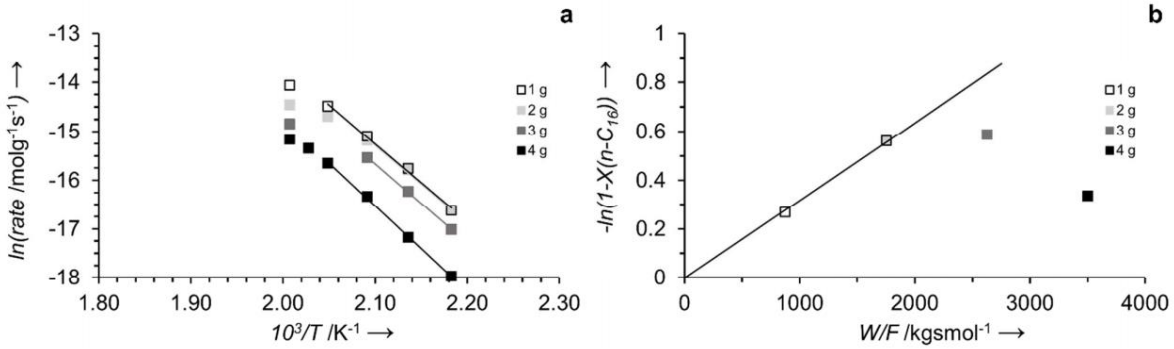

Figure 4.9: (a) Arrhenius plot of n-hexadecane hydrocracking over (a) Pt/MFI (1nm) with 0.9 wt.% Pt at W/F: 875 to 3500 kgs/mol at varying amounts of catalyst powder, (b) linear fitting to pseudo first order rate equation for ideal plug flow using data at 205 °C, 20 bar and H_2/n-C_{16} = 10 mol/mol. Taken from Brosius et al., 2016.

Furthermore, Table 4.8 summarises the typical conditions used in a reactor test. The temperature is ramped in increments of 10 °C. The temperature limits are determined during each experiment according to the activity of the catalysts with the objective being to reach low conversion (0-10 %) and high conversion (90-100 %). The test was always run with a constant H_2 and n-C_{16} flowrate with water added after the dry hydrocracking run was complete.

Table 4.8: Summary of Catalyst Test Conditions

Temperature (°C)	**Feed Flowrates (mL/min)**		
	H_2	n-C_{16}	H_2O
225	16	0.022	0
215			
205			
195			
185			
235			
245			
235	16	0.022	0.016
245			
255			
265			
275			
285			

Chapter 5

Catalyst Preparation and Characterisation

The previous chapter described the experimental method designed to test the hypotheses of this study. A three-part approach was developed as follows: catalyst preparation and characterisation; catalyst performance determination in a n-C_{16} model reaction; and post-mortem catalyst characterisation. In this chapter, catalyst preparation and characterisation is presented and discussed with the overall aim of placing Pt NPs exclusively inside or outside of the MFI micropores (~0.55 nm diameter). Placing the metal exclusively outside is attempted by placing pre-synthesised Pt NPs between 1-2 nm, which are too large to fit into the micropores, onto the MFI. Synthesis by colloidal chemistry and chemical vapour deposition are explored. Placing the metal exclusively inside is attempted via a competitive ion exchange method.

5.1 PT NPS BY COLLOIDAL CHEMISTRY

Through separation of the nucleation and growth phases, as described by LaMer's Theory (LaMer and Dinegar, 1950), it is possible to produce a monodisperse colloidal suspension of NPs. The colloidal solution can then be subjected to an appropriate inhibition of coagulation method, such as contact with a capping agent, to disperse the NPs on a support. The capping agent can then be removed to leave active monodisperse Pt NPs well dispersed on the external surfaces of a support. These steps will be discussed in detail for placing Pt NPs on MFI, as follows.

5.1.1 Monodisperse Colloidal System

A polyol process by Wang *et al.*, 2000 was replicated in this research to produce a Pt NP colloid with a particle diameter range of 1-2 nm. As described in detail in **Chapter 2**, the overall reaction is as follows:

$$H_2PtCl_6 \xrightarrow[(2)\ 160\ ℃,\ inert\ gas\ flow]{(1)\ NaOH,\ pH>12\ in\ ethylene\ glycol} \text{"unprotected" } Pt\ NPs \qquad \text{Equation 5.1}$$

The Pt containing salt is first transformed into a (hydr)oxide colloid solution via the addition of NaOH. This solution is then reduced to Pt NPs at high temperature by EG which acts as both the solvent, reducing agent and, to some extent the capping agent. The preparation method is

described in **Chapter 4** and the following observations were made:

A transparent yellow solution was formed after the initial mixing of the NaOH in EG solution and the $H_2PtCl_6.6H_2O$ in EG solution. This indicates the formation of the Pt (hydr)oxide colloidal (Wang *et al.*, 2000). After approximately 2 minutes of the mixture stirring at 160 °C, a dark-brown homogenous colloidal solution was observed with no precipitate – indicating that nucleation has occurred and the Pt NP colloidal solution has formed. No further changes were visible during the remainder of the 3 hour reaction as the solution entered the slow growth by diffusion phase (LaMer and Dinegar, 1950). The final solution remained stable after standing for several months as the EG can adsorb onto the surface of the Pt NPs to prevent aggregation (Wang *et al.*, 2000).

TEM images of the colloidal Pt NP solution in EG (**PtNPs/EG**) can be seen in *Figure 5.1*.

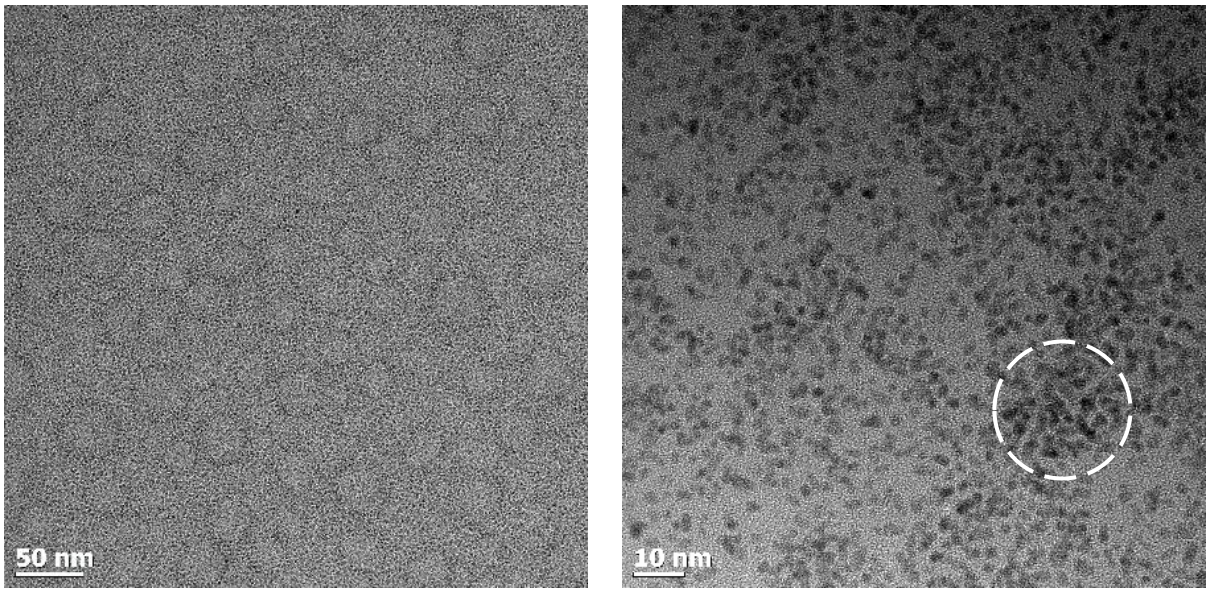

Figure 5.1: TEM images of PtNPs/EG at varying magnification

From lower magnification, a continuous layer of monodisperse Pt NPs is visible with little evidence of larger agglomerates. At higher magnification, the Pt NPs are mostly spherical in shape but there is evidence of some shape variability. In some areas, the Pt NPs may appear to be aggregated (as indicated in *Figure 5.1*) but most individual particles have visible boundaries. These aggregates are further investigated after the Pt NPs are capped and supported as it is unclear as this stage whether this effect is reversible.

Figure 5.2 displays a particle size distribution of a sample of NPs from **PtNPs/EG**. The synthesis was repeated to assess reproducibility (**PtNPs/EG (repeat)**) and compared with the published results from Wang *et al.*, 2000 (**PtNPs/EG (Wang *et al.*, 2000)**). The particle size distributions are assumed to be normally distributed with sample means as follows; **PtNPs/EG**: 1.70±0.28 nm, **PtNPs/EG (repeat)**: 1.53±0.29 nm and, **PtNPs/EG (Wang *et al.*, 2000)**: 1.57±0.31 nm.

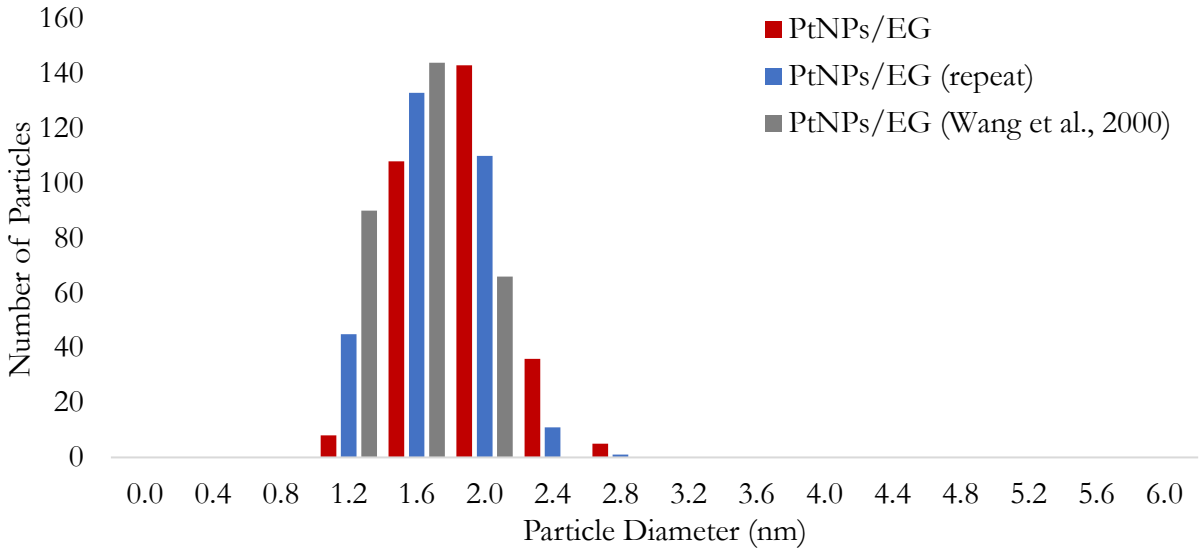

Figure 5.2: Particle size distribution of (red) PtNPs-EG, (blue) PtNPs-EG (repeat) and (grey) PtNPs-EG (Wang et al., 2000).

A statistical analysis was conducted to quantify the variability of the samples beyond the visual representation, as seen in **Appendix B**. Through "Z" hypothesis testing it is determined that the three synthesis attempts have particle means which are within 0.2 nm difference. With the overall aim defined as producing Pt NPs between 1-2 nm this level of variability is considered acceptable. It is also notable that particle size measurements of the **PtNPs/EG** are not completely accurate as EG contamination in the TEM images makes the particle boundaries unclear. Therefore, further particle size distributions will need to be evaluated at later stages in the Pt NP synthesis.

5.1.2 Capping, Supporting and Pre-Treatment

Continuing with the reproduction of Wang *et al.*, 2000, the Pt NPs were separated from EG and capped and redispersed before being supported. Oxidation/reduction pre-treatments were applied to the supported Pt NPs to remove the capping agent without drastically affecting the particle size. The smallest Pt NPs after supporting and pre-treatment on MFI were also supported on pre-synthesised MFI NSs. Details on the supporting and cleaning methods can be found in **Chapter 4**. Two capping agents were investigated in this research; PVP (Wang *et al.*, 2000) and later OCA (Kim *et al.*, 2013). Each capping agent has a different method for removing the Pt NPs from EG and applying the capping agent to the NPs. Particle size and Pt yield were compared.

5.1.2.1 PVP Capped Nanoparticles

The first method for separation of the Pt NPs from EG is achieved by adjusting the pH of the EG colloidal solution to a value lower than 4 using dilute aqueous HCl. The following observations were made:

The addition of HCl caused the Pt NPs to immediately start separating out of solution in a black precipitate which could then be recovered by centrifugation. However, a completely Pt NP free supernatant was not achieved in the centrifuging step. At best, a light brown/yellow supernatant was produced, indicating Pt NP loss in the separation stage. The black precipitate was then redispersed in a mixture of ethanol and PVP to produce a dark brown homogenous solution

with no precipitate. The homogeneous nature suggests that the Pt NPs were successfully capped as no large agglomerates of NPs formed.

The following calculation was performed to determine if the residual Pt NPs in the supernatant were because of limitations in the literature sourced centrifugation conditions (Rioux *et al.*, 2005) or because of limitations in the pH change separation method:

Using Stokes' Equation, the rate of particle sedimentation of the Pt NPs in EG is calculated to be ~1.14E-04 cm/hr. This is calculated using the maximum relative centrifugal field at maximum speed achievable using a JA-20 rotor (48 400 x *g*), see **Appendix B** for details and assumptions. Therefore, to move the sediment by 2 cm through the solvent would require ~ 17500 hours. This suggests that the particle separation is primarily achieved by the pH change in the solution and the centrifugation step will not separate out residual Pt NPs which are unaffected by the pH change. Henceforth, the given centrifuge settings from Wang *et al.*, 2000 to separate out the already formed black precipitate were used with no further investigation. Further removal may be possible by a more severe pH change, however increasing Pt NP yield is beyond the scope of this research.

The Pt NPs capped in PVP and supported on MFI (**PtNPs-PVP/MFI)** were characterised using **TEM** and **CO chemisorption** for particle size and dispersion and **ICP-OES** for Pt yield as follows.

TEM

Figure 5.3 shows representative TEM images of the ethanol colloidal solution (**PtNPs-PVP/Ethanol**).

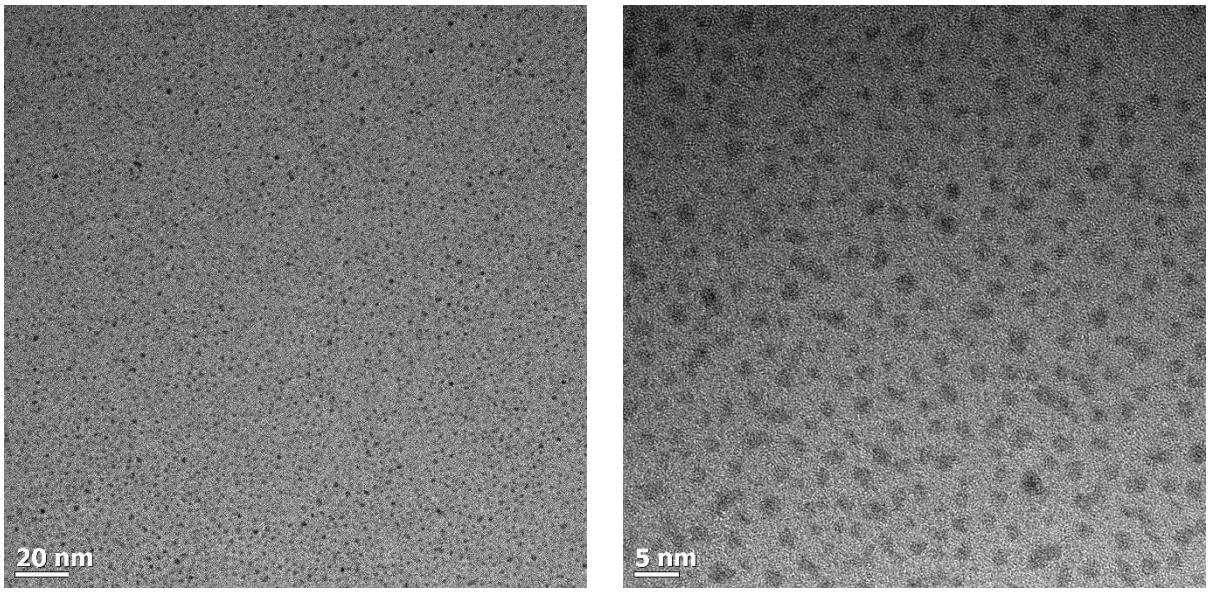

Figure 5.3: TEM images of PtNPs-PVP/Ethanol at varying magnification

It is evident at lower magnification that the capping process has occurred successfully with all individual particles clearly separated and no signs of agglomeration. At higher magnification, the particles continue to show a monodisperse nature. *Figure 5.4* shows sample TEM images of the

PtNPs-PVP particles after supporting (**PtNPs-PVP/MFI**) and after pre-treatment (**PtNPs-PVP/MFI Ox-Red & CO Chemi**).

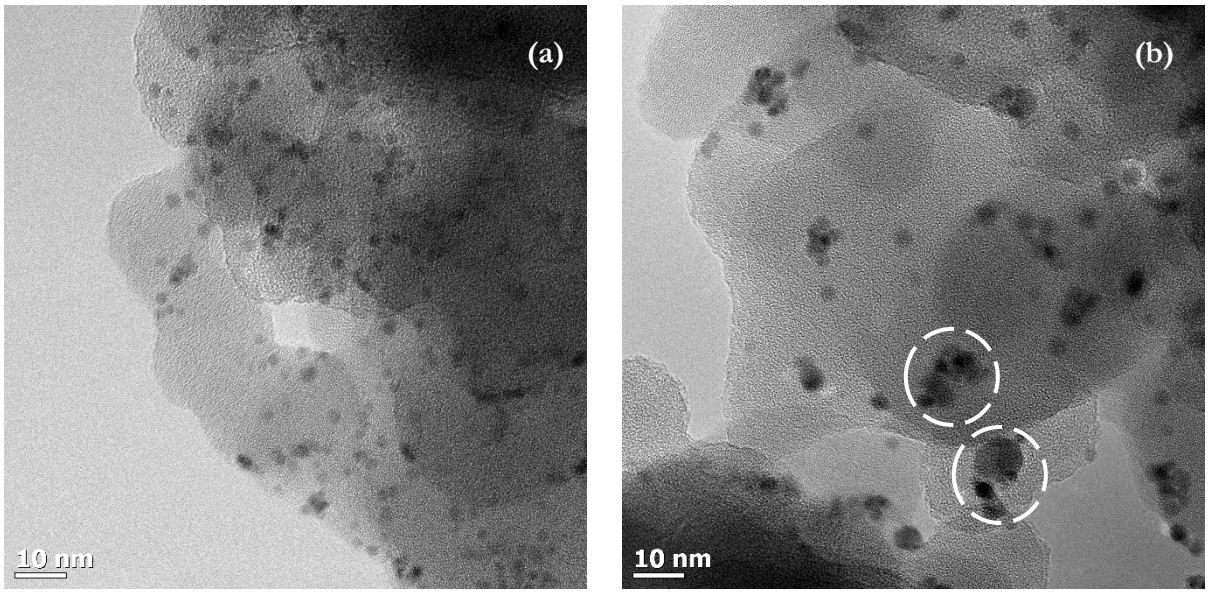

Figure 5.4: PtNPs-PVP/MFI (a) after washing and (b) after an oxidation/reduction pre-treatment

In *Figure 5.4 (a)*, the Pt NPs are dispersed on the MFI support with little sign of agglomeration. However, after pre-treatment the TEM images show noticeable sintering indicated in *Figure 5.4 (b)*. An adapted pre-treatment from Rioux *et al.*, 2005 and Brosius *et al.*, 2016 was followed: oxidation in 120 ml/min O_2 at 0.2 °C/min to 350 °C, hold for 60 mins and reduction in 120 ml/min H_2 at 0.2 °C/min to 225 °C, hold for 480 mins. Details on the chosen pre-treatment conditions are discussed in **Chapter 2**. The sintering effects are compared using particle size distributions as seen in *Figure 5.5*.

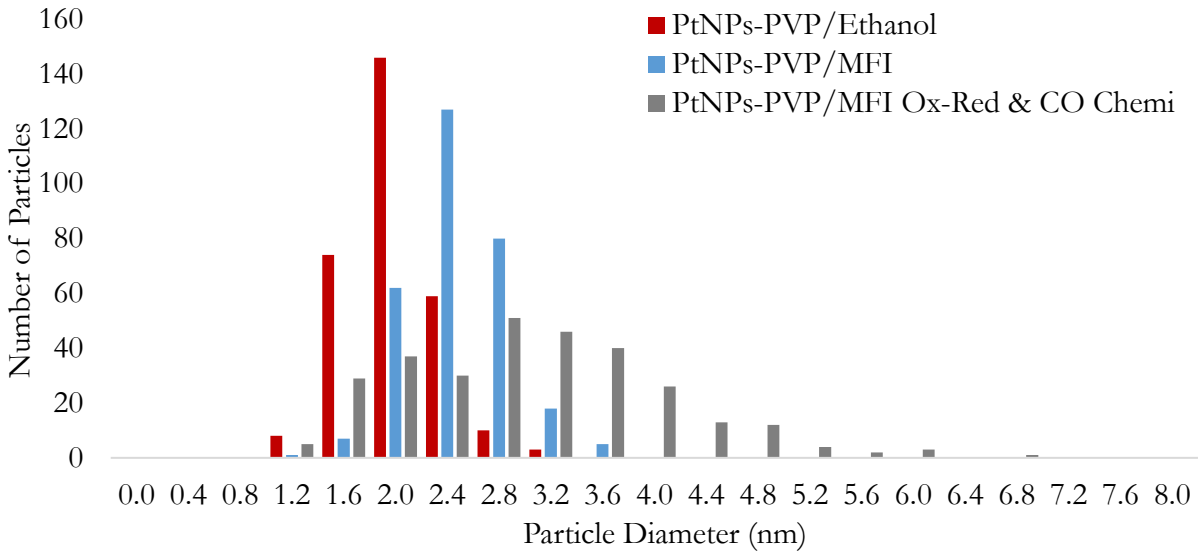

Figure 5.5: Particle size distribution of (red) PtNPs-EG-PVP, (blue) supported on MFI and (grey) after oxidation and reduction.

Two important observations can be made from the comparison of the particle size distributions at different stages of the synthesis. Firstly, comparing **PtNPs-PVP/Ethanol** and **PtNPs-PVP/MFI,** the sample mean has changed from 1.80±0.33 nm to 2.27±0.37 nm. The size increase may suggest that the smallest Pt NPs did not separate from the EG in the pH adjustment separation, leaving a larger overall size range. Alternatively, limitations in the TEM imaging may have masked the smallest particles on the support, skewing the distribution. Secondly, **PtNPs-PVP/MFI Ox-Red & CO Chemi** increased to 2.92±1.21 nm; indicating the severity of the sintering which has more than doubled both the average and standard deviation in comparison to **PtNPs-PVP/EG.**

In the paper by Rioux *et al.*, 2005, the particle size results are misleading as the free-standing particle size of 1.73±0.26 nm (from TEM) is used in the particle size effect results. However, on closer inspection it is seen that after supporting and pre-treatment on SBA-15, the particle size from TEM analysis is not re-calculated and only H_2 chemisorption results are given at 2.9 nm. The discrepancy between the free-standing TEM results and the H_2 chemisorption is explained by a portion of the Pt NPs which are involved in bonding with the silica surface and will therefore not chemisorb gas. The paper does not attribute any of the size difference to particle sintering when using SBA-15 but this is not fully proved. In this investigation of the Pt NPs on MFI, it is evident that particle sintering is playing a role. This has resulted in the final Pt NPs not being within the 1-2 nm required range and adjustments to the pre-treatment are considered and analysed using CO chemisorption as follows.

ICP-OES

ICP-OES was used to determine the weight percentage of Pt on the supported catalysts after cleaning. Each catalyst analysed in hydrocracking should have a metal loading above 0.9 wt. % to ensure the metal sites are not rate limiting, as described in **Chapter 2**. Table 5.1 displays the results of the ICP-OES analyses conducted by the UCT Analytics Laboratory. Several ICP analyses were done for different batches of **PtNPs-PVP/MFI** and were used to determine consistency in the loading method.

Table 5.1: ICP-OES Results for PtNPs-EG-PVP/MFI

Pt In/ Zeolite In (wt. %)	**ICP-OES Analysis after Supporting & Cleaning**				**Pt Yield (wt. %)**
	Sample Mass (mg)	Volume (l)	Dilution Factor	Content (wt. %)	
0.77	50.3	0.100	neat	0.45	59
1.55	50.3	0.025	4.95	0.94	61
1.65	50.5	0.025	4.97	0.99	60
1.65	49.8	0.025	4.99	1.00	61

The Pt in/zeolite in (wt. %) is calculated from the mass of the Pt salt used, converted from the moles of $H_2PtCl_6.xH_2O$ assuming x is equal to 6. The sample mass refers to the amount of solid sample digested and the volume and dilution factor refer to the final sample used for ICP-OES. *Figure 5.6* shows a graphical representation of the ICP-OES data in relation to the Pt used in the synthesis, to investigate losses due to the separation from EG, supporting and, washing steps.

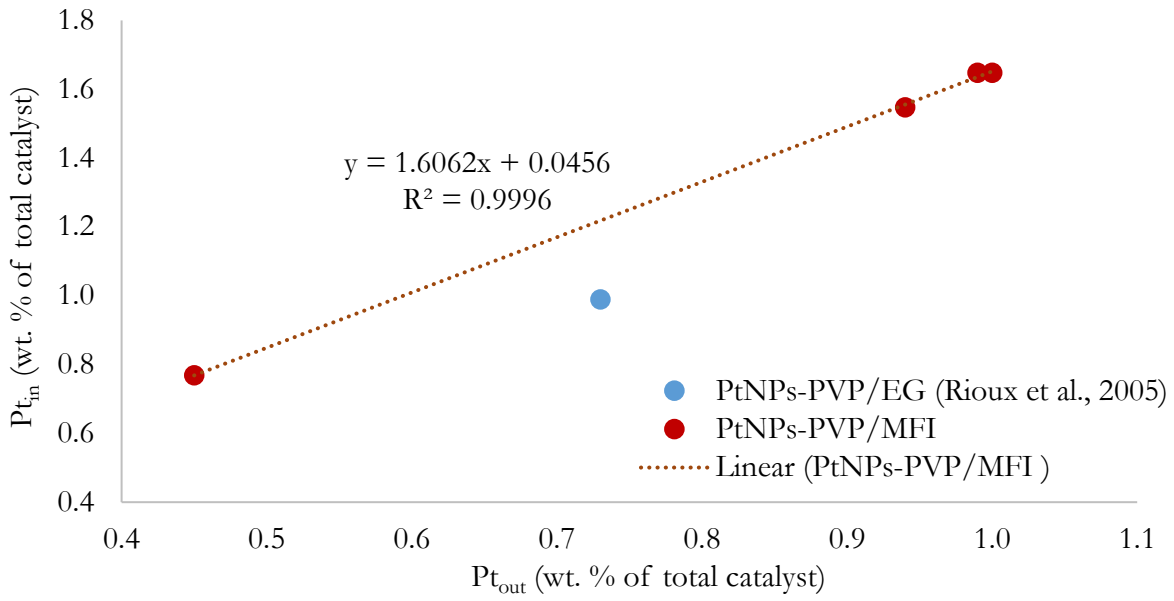

Figure 5.6: Pt loss in synthesis of (red) PtNPs-PVP/MFI and (blue) PtNPs-PVP/SBA-15 from Rioux et al., 2005.

The y-axis (**Pt_{in}**) represents Pt used in the synthesis as a wt. % of the zeolite added in the supporting step. The x-axis (**Pt_{out}**) represents the wt. % of Pt in the supported and washed catalyst determined from ICP-OES. The **PtNPs-PVP/MFI** data set is fitted with a linear trend line which has an R^2 = 0.996, indicating a good fit of the available data. The line equation was therefore used in estimating **Pt_{in}** to achieve a specified **Pt_{out}**. The **PtNPs-PVP/SBA-15** data point is calculated from Rioux *et al.*, 2005 using the given concentration of the starting Pt solution and the ICP-OES result. The literature value from Rioux *et al.*, 2005 is below the experimental line, suggesting a better yield is achieved. Interpolating from the experimental trend line, there is a difference in **Pt_{out}** of approximately 0.23 wt.%. In this preliminary investigation of metal location effects, yield is not an important factor and optimisation is not pursued.

CO Chemisorption

CO chemisorption is a bulk technique which was used to determine an average particle size for the PtNPs on MFI. Using the MicroMeritics ASAP2020 instrument, it is also possible to simulate the oxidation/reduction pre-treatment – just as it would be pre-treated ahead of catalytic testing. As CO chemisorption determines a particle size from the available active metal surface, a disparity between TEM and CO chemisorption particle sizes after pre-treatment will give an indication of the extent of PVP removal.

Two pre-treatments were initially investigated for the effects on particle size as follows:

- O2 flow: heat to 350 °C at 0.2 °C/min. **Hold 60 min**. H2 flow: heat to 225 °C at 0.2 °C/min. Hold 60 min.
- O2 flow: heat to 350 °C at 0.2 °C/min. **Hold 720 min**. H2 flow: heat to 225 °C at 0.2 °C/min. Hold 60 min.

The CO chemisorption gas adsorption quantities versus pressure for the two samples can be seen in *Figure 5.7*.

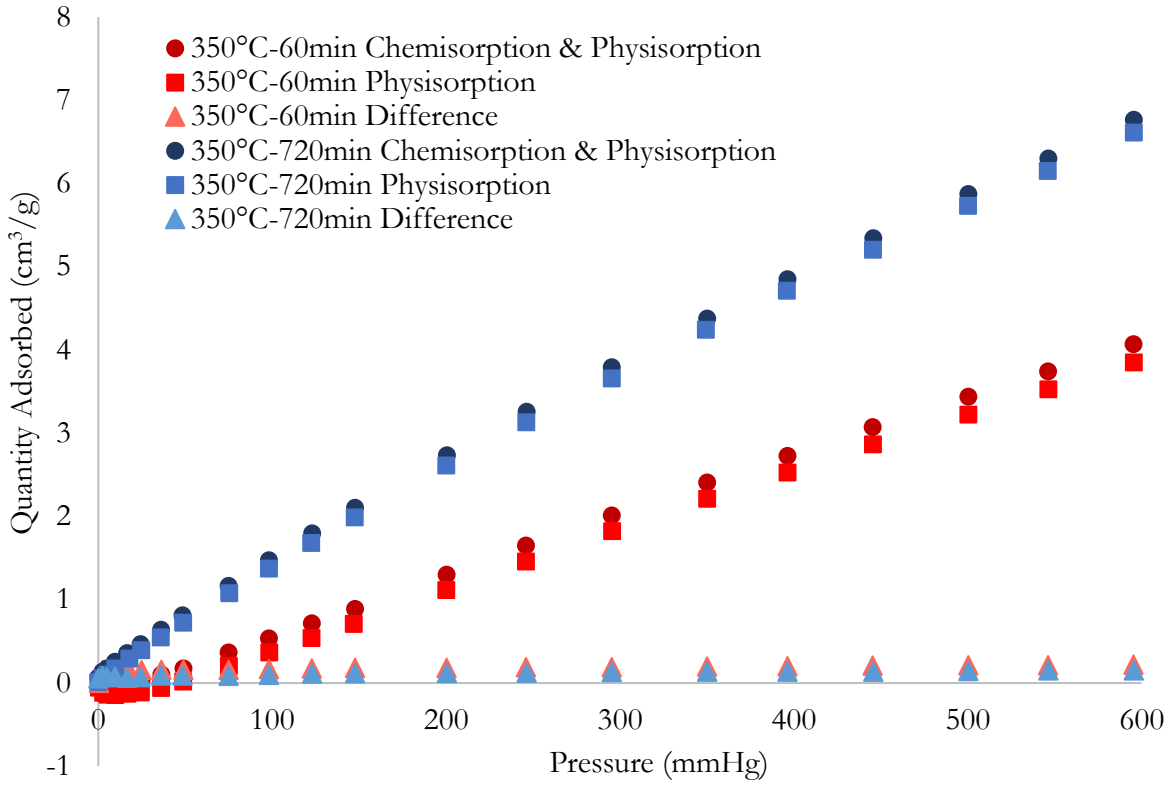

Figure 5.7: CO chemisorption on PtNPs-PVP/MFI. Oxidation at 0.4 °C/min to 350 °C, hold (red) 60 mins and (blue) 720 mins. Reduction at 0.4 °C/min to 225 °C, hold 60 mins.

For each sample, the chemisorption and physisorption isotherm is indicated by circle markers; the physisorption only isotherm by square markers; and the difference isotherm by triangle markers. It is evident that the change in pre-treatment did not show a large difference in the particle size with each corresponding isotherm being similar. Table 5.2 shows the results for the dispersion and particle size calculations as described in detail in **Chapter 4.**

Table 5.2: CO Chemisorption Results for PtNPs-PVP/MFI, Varying the Pre-Treatment

Oxidation Hold Time (mins)	**Oxidation Temp-erature**	**TEM Particle Size before PT (nm)**	**ICP-OES (wt. %)**	**CO Chemisorption**			**TEM Particle Size after PT (nm)**
				Quantity Adsorbed (cm^3/g STP)	Dis-persion (%)	Particle Size (nm)	
60	**350**	**1.80 ± 0.33**	1.00	0.14	11.77	**9.78**	**2.92 ± 1.21**
720	**350**			0.13	11.62	**9.91**	**4.40 ± 10.67**

The two samples were taken from the same batch of **Pt-NPs-PVP/MFI** with a TEM particle size before pre-treatment of 1.80±0.33 nm and an ICP-OES determined metal loading of 1.00 wt.%. Evidently, the CO chemisorption particle sizes after pre-treatment (which are >9 nm) differ greatly from the size before pre-treatment. This indicates that the pre-treatments have been unsuccessful. It is expected that there are two main reasons why the CO chemisorption diameters are larger than the pre-treated sample. The first is particle sintering, which is caused during high temperature pre-

treatment (van Steen., 2014). The second is insufficient removal of PVP from the metal sites, which is caused by an ineffective pre-treatment (Rioux *et al.*, 2005).

Comparing the post pre-treatment results for the shorter hold time of 60 minutes: the TEM particle diameter gave 2.92±1.21 nm whereas, the CO chemisorption calculation gave ~9.78 nm. The difference shows that the CO chemisorption active metal surface area is too low indicating that there might still be PVP on the surface. Comparing the post-treatment results for a longer hold time of 720 minutes: the TEM particle diameter was 4.40±10.67 nm and the CO chemisorption particle size was ~9.91 nm. The difference is now smaller indicating that less PVP is blocking metal sites – showing better PVP removal with increased pre-treatment time. However, the severity of sintering has increased as evident from the TEM particle size standard deviation of 10.67 nm.

In a last attempt, a pre-treatment with oxidation at 250 °C was undergone to assess whether a much longer (above 720 minutes) low temperature pre-treatment could retain the original NP size distribution and remove PVP. The catalyst was pre-treated in the trickle bed reactor and then removed for TEM analysis. Unfortunately, after oxidation at 0.2 °C/min to 250 °C and 480 mins hold time followed by the standard reduction conditions (shown above), the Pt size distribution was already 2.74 ± 0.62 nm. PVP is notoriously difficult to remove from Pt NPs (Rioux *et al.*, 2006) and no exception was seen in **PtNPs-PVP/MFI** samples. Sintering (which takes the Pt NPs out of the diameter range needed) is experienced under the necessary pre-treatment conditions to remove PVP and therefore this capping agent is not further explored.

5.1.2.2 OCA Capped Nanoparticles

The second method to separate the Pt NPs from EG is achieved through phase separation after capping, as described in **Chapter 4**. The following was observed:

OCA in a toluene solution was added directly to the Pt NP colloidal solution in EG and allowed to stir over night. After stirring, two layers form. The top layer was dark brown with a viscous appearance (the organic layer) and the bottom layer was cloudy and less viscous (the aqueous layer). Ethanol was added to the solution which re-disperses the Pt NPs into a brown homogeneous solution. After the addition of H_2O with shaking, the solution settled into the aqueous and organic layers again. The aqueous layer was then decanted and a small amount of HCl was added to the Pt NP organic layer for neutralisation of excess OCA. It was observed when adding the HCl that a white vapour is released on contact with the organic layer. A series of washes was then conducted by adding H_2O, shaking, allowing to settle, and then removing the aqueous layer. This was repeated until no residual chloride was seen in the washing waters, as chloride is a known poison to the catalyst system (Philippaerts *et al.*, 2010). 0.1 M silver nitrate solution was used to test for residual chloride; since the reaction of silver nitrate and HCl produces a colour change from transparent to cloudy white.

TEM

The Pt NPs capped in OCA in the organic (toluene) layer (**PtNPs-OCA/Toluene**) were analysed under TEM as seen in *Figure 5.8*.

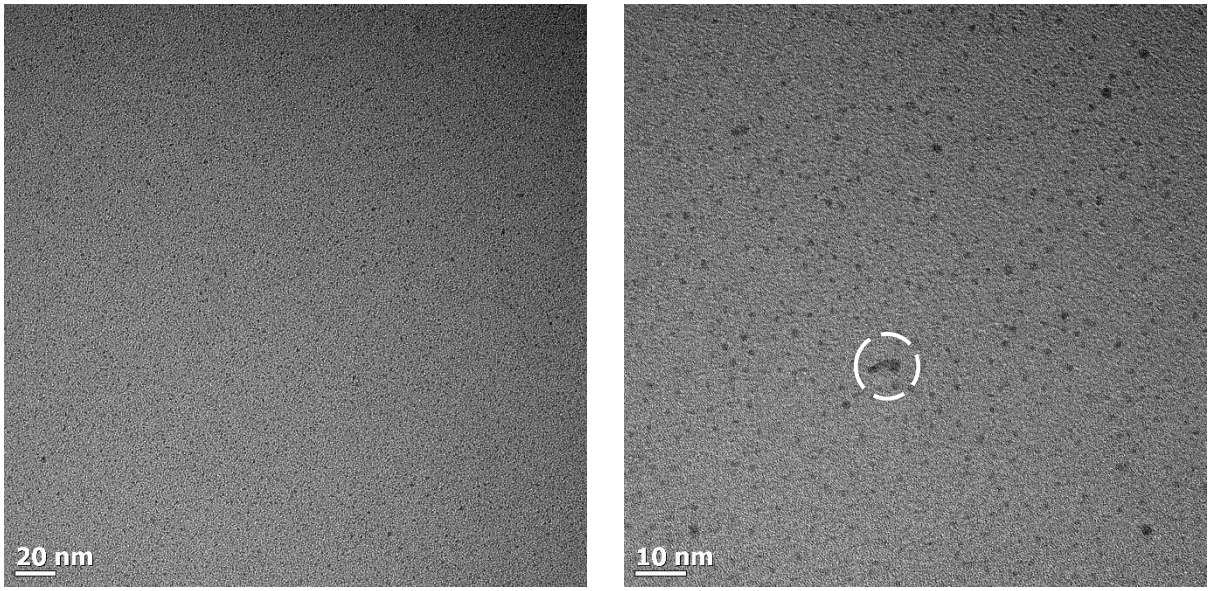

Figure 5.8: TEM images of PtNPs-OCA/Toluene.

The results are similar to the PVP capped Pt NPs, with little sign of agglomeration at lower magnification and a monodisperse nature at higher magnification. There is some evidence of areas where a few individual particles have agglomerated (as marked on the TEM image), however this was rarely seen in the full TEM analysis.

PtNPs Supported on Bulk MFI (MFI)

The Pt NPs capped in OCA were supported on MFI (**PtNPs-OCA/MFI**) after thoroughly washing the organic layer with H_2O. The sample was then analysed by STEM-BF and corresponding HAADF images (*Figure 5.9*). Standard TEM techniques could not be used as the very small NPs (1-2 nm) supported on MFI are difficult to see – resulting in inaccurate diameter measurements.

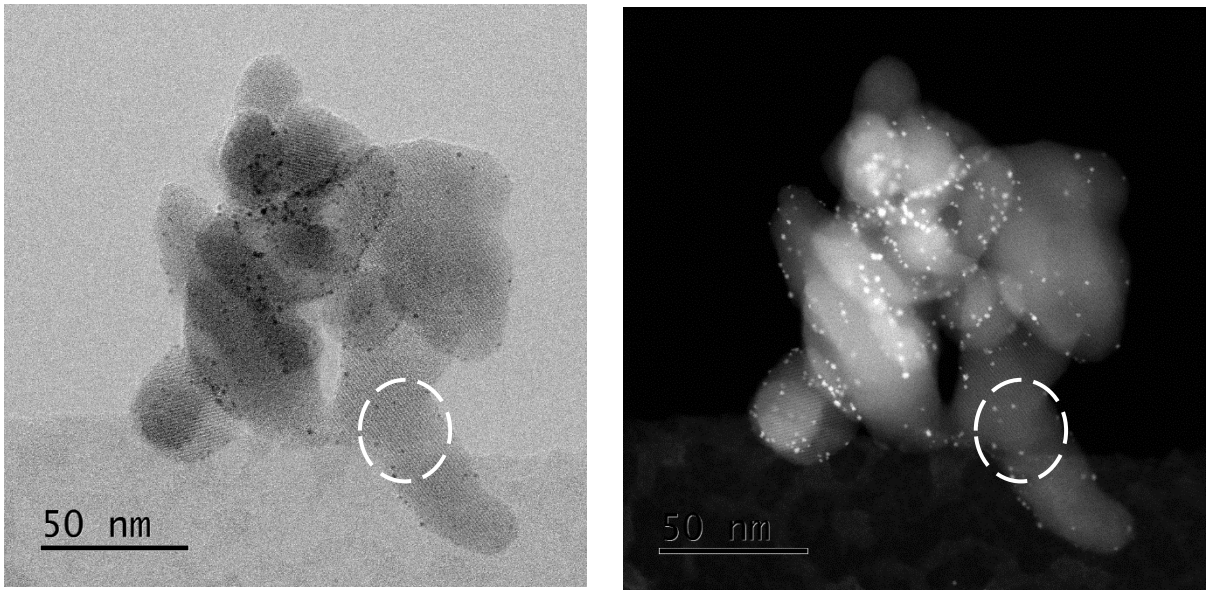

Figure 5.9: STEM-BF and HAADF images of PtNPs-OCA/MFI.

A good dispersion of small monodisperse Pt NPs is observed. The smallest particles are easier to detect in the HAADF image in some cases as highlighted on the images. *Figure 5.10* shows the STEM-BF and HAADF images of **PtNPs-OCA/MFI** after a cyclic pre-treatment of oxidation and reduction steps (as detailed in **Chapter 4**) performed in the CO chemisorption apparatus. It is important to note that the images were taken after CO chemisorption and it is assumed that the NP size is not affected by adsorption of CO.

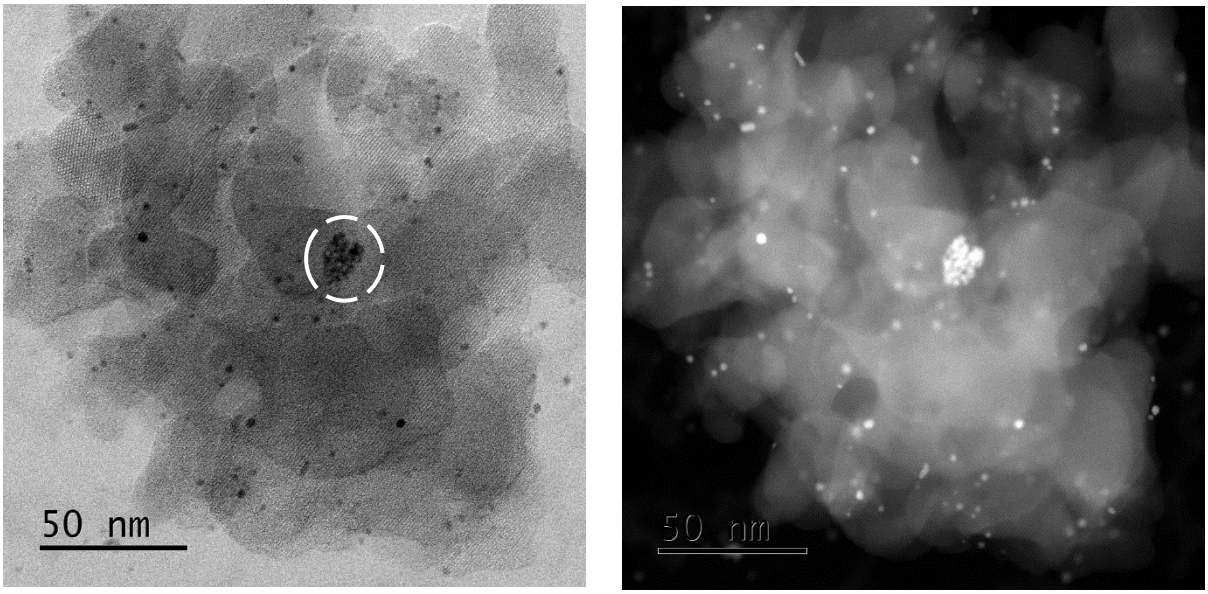

Figure 5.10: STEM-BF and HAADF images of PtNPs-OCA/MFI after a cyclic oxidation/reduction pre-treatment and CO chemisorption

The majority of the Pt NPs appear to have held their size and shape – indicating a successful pre-treatment. There is some evidence of agglomeration (as indicated) but the majority of the Pt NPs have not sintered. A particle size distribution comparison can be seen in *Figure 5.11* of the Pt NPs capped in OCA at different stages of the synthesis.

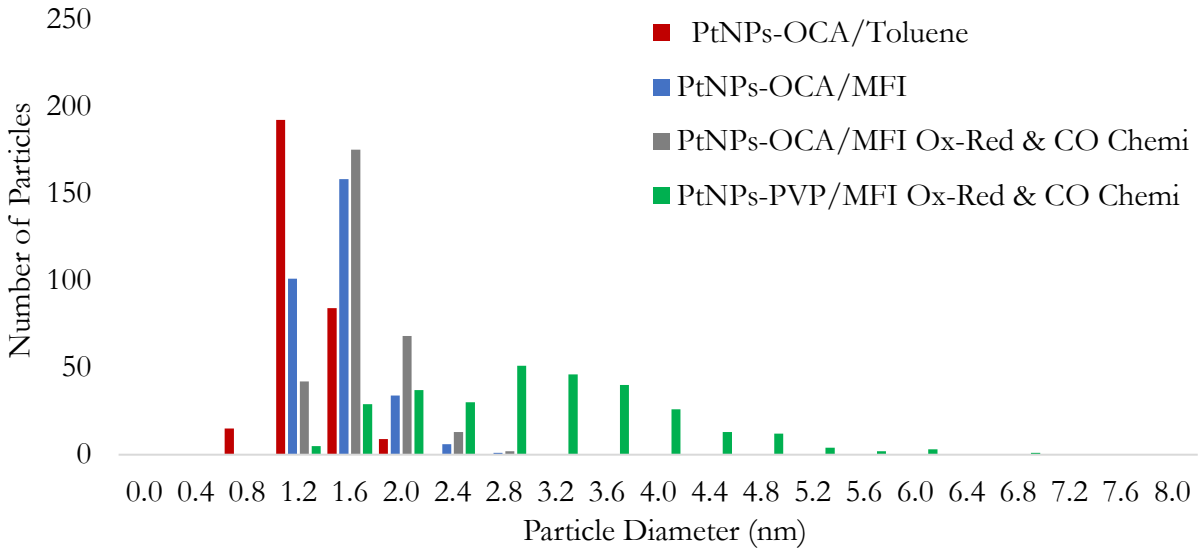

Figure 5.11: Particle size distribution of (red) PtNPs-OCA/Toluene, (blue) supported on MFI and (grey) after oxidation and reduction and CO chemisorption as well as (green) PtNPs-PVP/MFI Ox-Red.

The sample means are 1.11±0.21 nm and 1.33±0.26 nm for **PtNPs-OCA/Toluene** and **PtNPs-OCA/MFI** respectively. In this case, there is no centrifuging step which could remove the smaller Pt NPs and the only difference is the visibility of the particles before and after supporting. This shows that even with the HAADF images there is still a discrepancy in the size once the Pt NPs are supported. After the oxidation/reduction pre-treatment the sample mean is 1.48±0.28 nm which indicates only a small amount of sintering has occurred. This is a significant improvement in comparison to **PtNPs-PVP/MFI Ox-Red** which shows severe sintering. Therefore, it is evident that the cyclic pre-treatment can remove OCA from the Pt NPs without drastically changing the particle size. Another interesting observation is comparing the Pt NPs uncapped and capped in PVP and OCA but not supported, the results are seen in *Figure 5.12*.

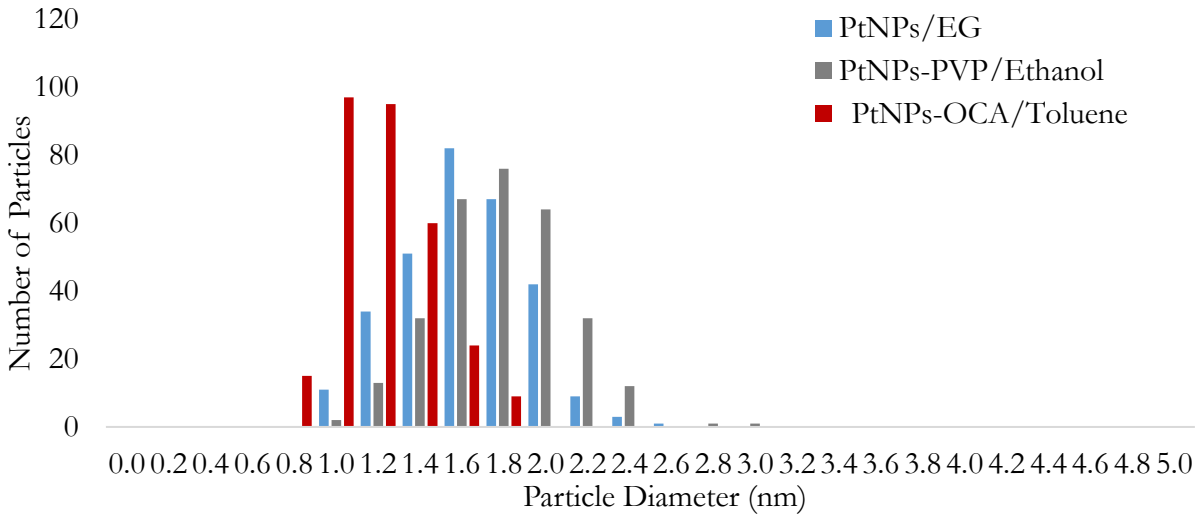

Figure 5.12: Particle size distribution of (red) PtNPs-OCA/Toluene, (blue) PtNPs/EG and, (grey) PtNPs-PVP/Ethanol.

In increasing size, the sample means were **PtNPs-OCA/Toluene**: 1.11±0.21 nm, **PtNPs/EG**: 1.53±0.30 nm and, **PtNPs-PVP/Ethanol**: 1.70±0.30 nm. This is an unexpected result as the same **PtNPs/EG** batches were used before contacting the different capping agents. One explanation may be that OCA is a much smaller molecule than PVP, resulting in an overall smaller particle in TEM imaging. Molecular modelling could be used to further investigate this effect but is deemed out of scope for this dissertation.

PtNPs Supported on MFI Nanosheets (NS)

PtNPs capped in OCA were also supported on NS (**PtNPs-OCA/NS**) following the same procedure used when supporting on MFI. *Figure 5.13* shows the STEM-BF and HAADF images.

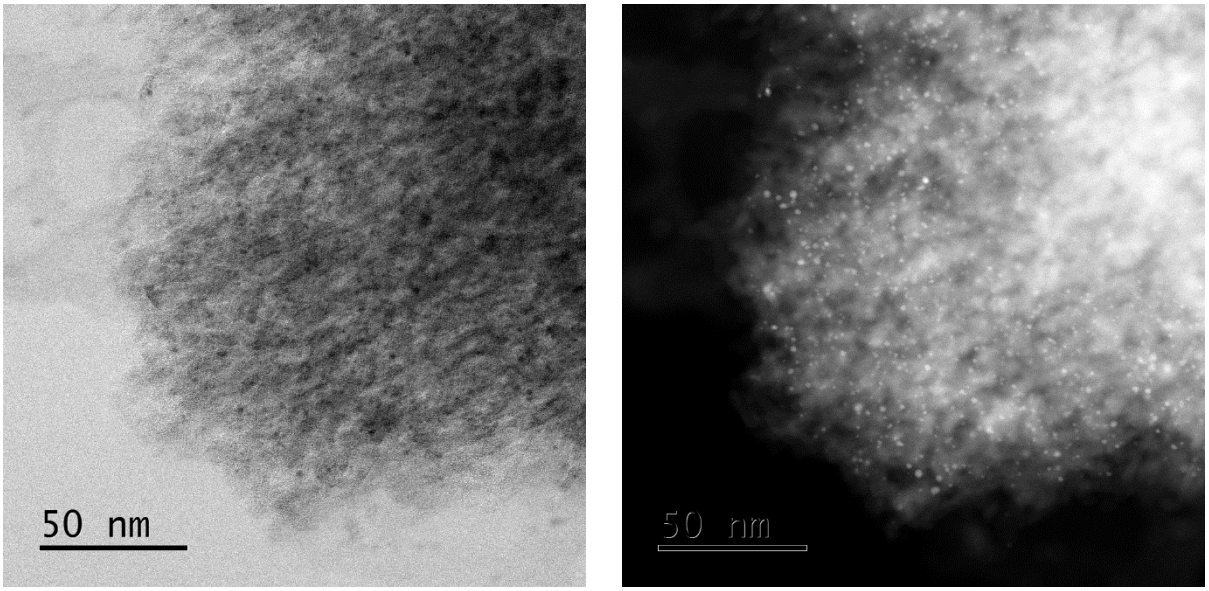

Figure 5.13: STEM-BF and HAADF images of PtNPs-OCA/NS.

The Pt NPs are small, monodisperse and well distributed on the NSs. The NS structure is evident from the thin strands which are visible on the edges of the imaged particle. *Figure 5.14* shows TEM images of the same sample after the cyclic pre-treatment and CO chemisorption.

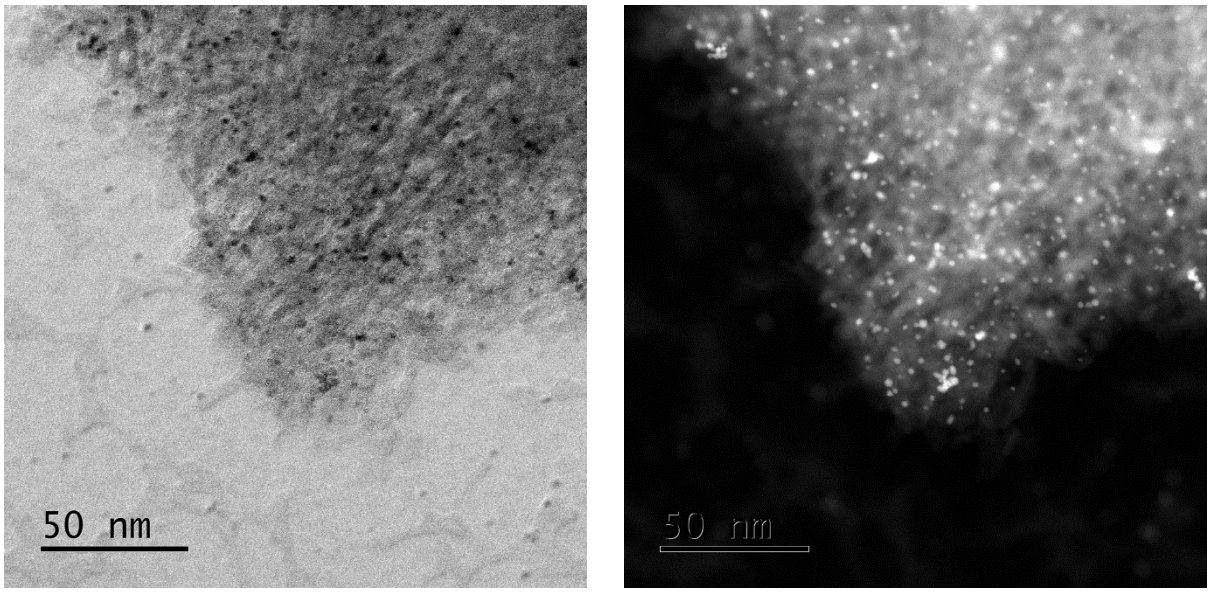

Figure 5.14: TEM and HAADF images of PtNPs-OCA/NS after cyclic pre-treatment and CO chemisorption.

The Pt NPs appear to have retained their dispersion in most cases with only small signs of sintering, showing an even better result than **PtNPs-OCA/MFI**. The particle size distribution can be seen in *Figure 5.15*, compared with the previous OCA samples.

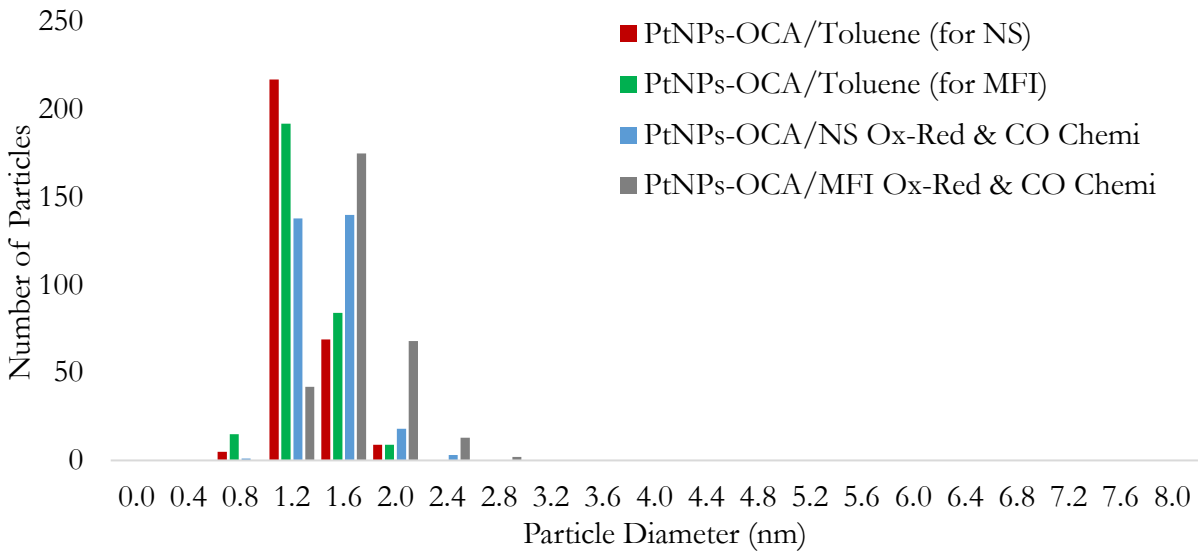

Figure 5.15: Particle size distribution of (red) PtNPs-OCA/Toluene (for NS), (green) PtNPs-OCA/Toluene (for MFI), (blue) PtNPs-OCA/NS Ox-Red & CO Chemi and (grey) PtNPs-OCA/MFI Ox-Red & CO Chemi.

The sample means for the two batches of PtNPs before capping were, **PtNPs-OCA/Toluene (for NS)**: 1.12±0.19 nm and **PtNPs-OCA/Toluene (for MFI)**: 1.11±0.21 nm. Since the sample means are so similar it is assumed that the batches are identical and can be compared. Therefore, after capping and pre-treatment the **PtNPs-OCA/NS Ox-Red & CO Chemi** gave, 1.24±0.23 nm and the **PtNPs-OCA/MFI Ox-Red & CO Chemi**, 1.48±0.28 nm. This indicates that the NS significantly decreased sintering. This was expected as the NS surface is made of individual thin strands which makes Pt migration more difficult than on a smooth bulk MFI surface.

In comparison to literature, Kim *et al.*, 2013 after supporting and pre-treatment achieved TEM distributions of 3.2±0.7 nm for bulk MFI and 1.8±0.3 nm for NSs with a similar thickness (~2 nm). This study produced significantly smaller particle means for both the MFI and NSs than previously seen in literature.

ICP-OES

The weight percentage of Pt on the supported catalysts was analysed for **PtNPs-OCA/MFI & NS** using ICP-OES. Table 5.3 shows the results of several samples prepared to determine reproducibility.

Table 5.3: ICP-OES Results for PtNPs-OCA/MFI and PtNPs-OCA/NS

Support	Pt In/ Zeolite In (wt. %)	ICP-OES Analysis after Supporting & Cleaning				Pt Yield (wt. %)
		Sample Mass (mg)	Volume (l)	Dilution Factor	Content (wt. %)	
MFI	1.601	50	0.05	4.94	1.35	84
	1.789	50.1	0.10	5.02	1.20	67
	1.570	45.2	0.10	5.01	1.24	79
	1.632	50.7	0.10	4.96	1.22	75
	1.538	52.9	0.10	5.02	1.06	69
NS	1.570	51.2	0.10	5.02	1.15	73

Using the same calculations as described for PVP Pt NPs, a plot of $\mathbf{Pt_{in}}$ versus $\mathbf{Pt_{out}}$ can be seen in *Figure 5.16*.

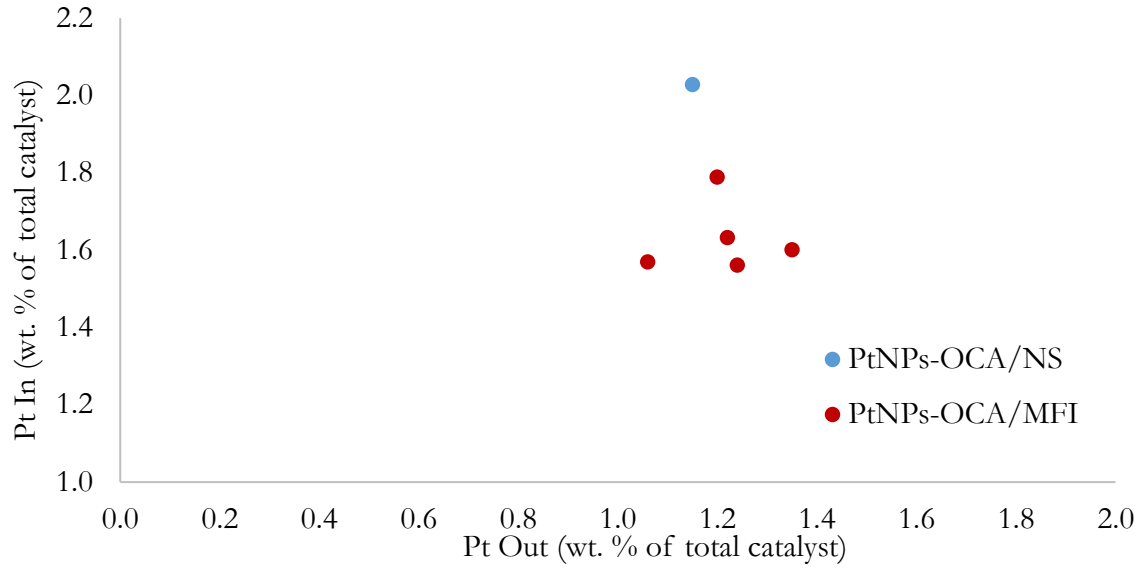

Figure 5.16: Pt loss in synthesis of (red) PtNPs-OCA/MFI and (blue) PtNPs-OCA/NS. Pt_{in} calculated from mass of Pt salt in and Pt_{out} determined from ICP-OES analysis.

No clear trendline can be plotted from the available data but it is evident that Pt_{out} is varying by ~0.4 wt. % when a similiar Pt_{in} in is used. The variability is most likely due to uncontrollable losses of Pt during the phase separation and washing steps. Comparing yield, the PVP synthesis was ~60 % whereas the yield for the OCA synthesis is higher at ~70 %. Yield optimisation was not further explored as it is beyond the scope of this study.

CO Chemisorption

The bulk technique with simulated pre-treatment was used to confirm the particle sizes which have been determined from TEM analysis. The CO chemisorption isotherms for MFI and NS samples can be seen in *Figure 5.17*.

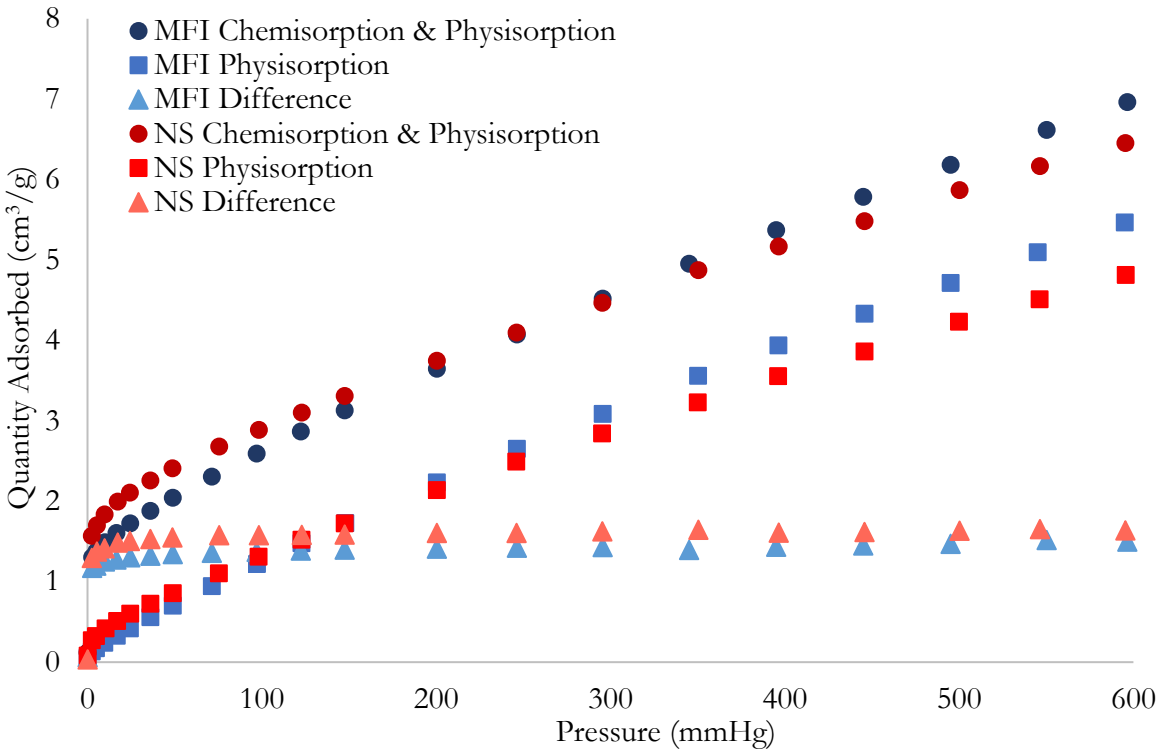

Figure 5.17: CO chemisorption on PtNPs-OCA/ (blue) MFI and (red) NS. Oxidation and reduction cycles at 0.4 °C/min to 300 °C, hold 30 mins and evacuate 30 mins for each step.

As described in the earlier CO chemisorption results, 3 isotherms are recorded for each experiment marked by circles, squares, and triangles. Comparing the experimental results, it is evident that there is not a significant difference between the MFI and NS results, which indicates the particle size means will be similar. In comparing to the **PtNPs-PVP/MFI CO chemisorption** results it is notable that the difference adsorption values have increased from ~0.5 (cm^3/g STP) to ~1.5 (cm^3/g STP) with **PtNPs-OCA/MFI**. The calculated results are summarised in Table 5.4

Table 5.4: CO Chemisorption and TEM Results for PtNPs-OCA on MFI and NS

Catalyst	**TEM Particle Size before Supporting (nm)**	**ICP-OES (wt. %)**	**CO Chemisorption**			**TEM Particle Size after CO Chemisorption (nm)**
			Quantity Adsorbed (cm^3/g STP)	Dispersion (%)	Particle Size (nm)	
PtNPs-OCA/MFI	1.11 ± 0.21	1.35	1.44	93.06	1.24	1.48 ± 0.28
			1.42[1]	91.55[1]	1.26[1]	
PtNPs-OCA/NS	1.12 ± 0.19	1.15	1.48	95.68	1.10	1.24 ± 0.23

[1] Repeat CO chemisorption

In the first main row of the table, the same **PtNPs-OCA/MFI** sample was repeated in the CO chemisorption experiment to ascertain reproducibility. The particle size averages were 1.24 and

1.26 nm, which are considered close enough to confirm that the CO chemisorption technique is reproducible in this study.

Overall, comparing the TEM before pre-treatment and CO chemisorption after pre-treatment it is evident that the results are within ~0.05 nm. Which suggests that very little sintering is observed. Furthermore, comparing the particle diameter results using CO chemisorption and TEM after CO chemisorption, it is evident that the difference is ~0.2 nm. Since the standard deviation of the TEM results is also ~0.2 nm, these results are considered to be the same. Suggesting that all the active metal surface is available for chemisorption and is not blocked by residual OCA.

NH_3-TPD

NH_3 TPD is used to investigate the effect of increased water washing in the preparation of **PtNPs-OCA/MFI**. *Figure 5.18* displays the results with different amounts of washing as well as non-supported MFI as a reference peak.

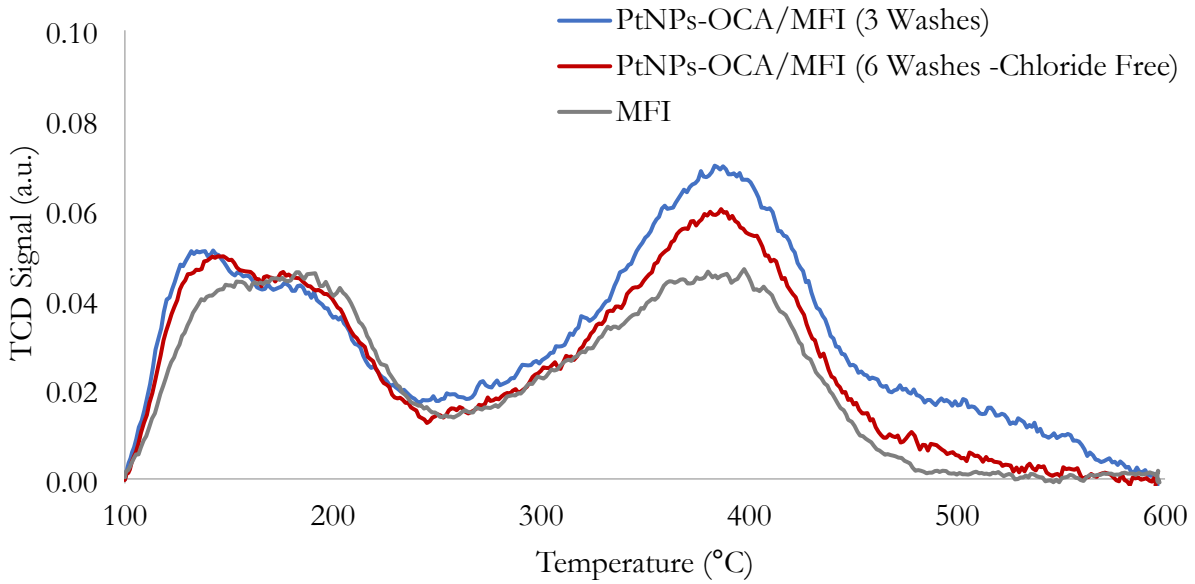

Figure 5.18: NH_3 temperature programmed desorption normalised per gram of PtNPs-OCA/MFI (blue) after 3 washes and (red) after 6 washes compared against (grey) pure MFI.

The peaks from the TCD signal are plotted against temperature for the three samples. In a typical MFI TPD pattern, 2 characteristic desorption peaks are seen at ca. 275 °C and 500 °C. In this case, the MFI plot shows a low temperature peak shifted to centre around ~180 °C and a high temperature peak shifted to centre around ~400 °C. These shifts are not further investigated in this research as they are consistent for the 3 samples and only a comparison is needed. It is widely accepted that the high temperature peak represents the desorption of NH_3 from Bronsted-acid sites (Reschetilowski *et al.*, 1989, Woolery *et al.*, 1997). Whereas, the low temperature peak/s are more difficult to identify. Reschetilowski *et al.*, 1989 proposed that the peaks are due to the interaction of ammonia with framework aluminium and sodium cations in the structure. Regardless of the speculation, the important conclusion is that the **PtNPs-OCA/MFI** samples show similar acidity to the base MFI – indicating that the impurities from the Pt addition have not compromised the MFI support. Furthermore, comparing the 3 samples, the only noticeable additional peak is

seen at ~500 °C for the sample which was washed 3 times (blue). As no other changes were made between the **PtNPs-OCA/MFI** samples, it is assumed that the peak centred ~500 °C is related to residual chloride. The chloride is subsequently seen to be removed after 6 washes as the peak at ~500 °C is no longer visible.

5.2 ORGANO-METALLIC CHEMICAL VAPOUR DEPOSITION

Another method to synthesise Pt NPs is through OMCVD. The principle behind OMCVD involves the vaporisation of a metal-containing precursor, commonly an organometallic complex, which thermally decomposes and deposits a metal film onto a substrate material (Thurier and Doppelt, 2008).

An in-house method developed by the UCT HySA research group was followed as described in **Chapter 4**. Platinum(II) acetylacetonate is used as the metal-organic precursor which is deposited onto MFI as Pt using a tubular reactor furnace. An important benefit of this method is that the metal is directly deposited onto the surface meaning no capping agent is required. The following observations were made:

After physically mixing and then sonicating the MFI powder and $Pt(acac)_2$, the final mixture appeared to be well mixed and homogenous. After the reaction, the resulting powder was less homogenous with spots of grey areas and white areas. After grinding, the powder appeared to be a consistent grey colour.

5.2.1 TEM

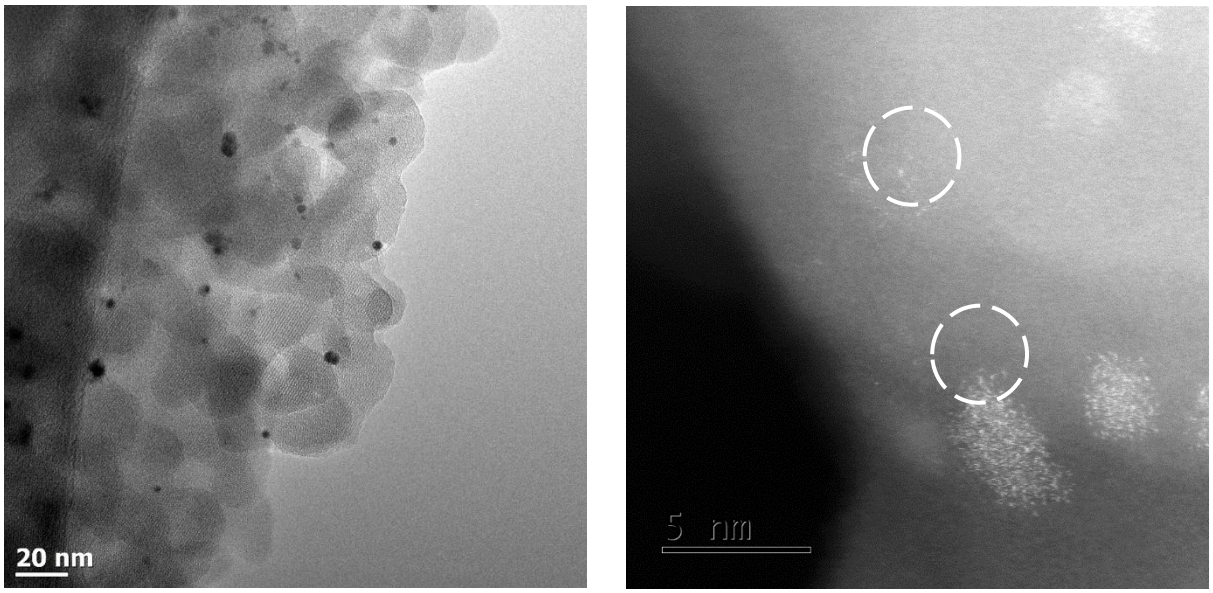

Figure 5.19: STEM-BF and HAADF images of Pt NPs deposited on MFI

The Pt NPs on MFI after OMCVD where analysed using BF-STEM and HAADF as can be seen in *Figure 5.19*. From the TEM images, the particles appear to be relatively well dispersed and are monodisperse in nature with sizes ranging from 1-3 nm. However, at higher magnification isolated small Pt clusters become visible amongst the particles of 1-3 nm range. This is a concern as the

clusters can fit into MFI micropores, meaning the Pt may no longer be exclusively on the outside. A particle size distribution can be seen in *Figure 5.20* which does not consider the Pt clusters.

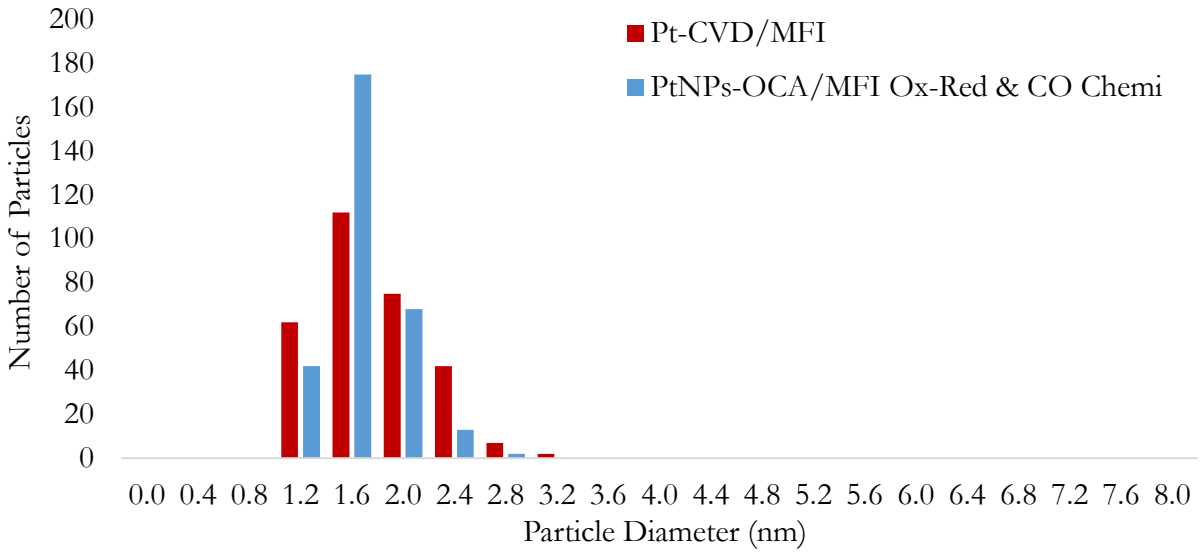

Figure 5.20: Particle size distribution plot for Pt-CVD/MFI before and after oxidation/reduction and CO chemisorption

The sample mean of **Pt-CVD/MFI** is 1.57±0.42 nm which is similar to the best Pt NPs synthesised by a colloidal method, **PtNPs-OCA/MFI Ox-Red & CO Chemi:** 1.48±0.28 nm. **Pt-CVD/MFI** does not need further oxidation pre-treatment as there is no capping agent to remove, however a reduction step will be needed before catalyst testing – which will further reduce the NP size.

Therefore, even though the NPs are in the correct size range, **Pt-CVD/MFI** cannot be used in metal location testing as there is no certainty that the metal is exclusively outside. An investigation into performance of this catalyst against **PtNPs-OCA/MFI**, which only has metal outside, may give an indication of how much impact the internal Pt clusters have.

5.2.2 ICP-OES

ICP-OES was used to determine the metal loading of the catalyst after synthesis, as seen in Table 5.5.

Table 5.5: ICP-OES Results for Pt-CVD/MFI

Pt In/ Zeolite In (wt. %)	**ICP-OES Results**				**Pt Yield (%)**
	Sample Mass (mg)	Volume (l)	Dilution Factor	Content (wt. %)	
0.92	50.6	0.1	neat	0.74	81

The yield is 81 % which is higher in comparison to the colloidal Pt NPs (at best 70 %). This is because the OMCVD method does not require cleaning which is usually where metal loss occurs. The remaining 19 % loss is most likely due to unreacted Pt salt.

Further characterisation was deemed unnecessary as **Pt-CVD/MFI** will not be used in the primary aim of this research which is to test metal location exclusively inside and outside the MFI micropores.

5.3 COMPETITIVE ION EXCHANGE

For placement of the metal inside the micropores, an IE technique was used. As zeolite crystalline lattices bear electric charges they are ideal ion exchangers. These ions are readily exchanged with Pt ions bearing an equivalent charge from aqueous solution (Schwarz *et al.*, 1995).

The method by Philippaerts *et al.*, 2010 was followed which uses $Pt(NH_3)_4Cl_2$ and the MFI zeolite (H-MFI) in the Na form (Na-MFI). CIE was implemented by adding additional Na ions (NaCl) during the ion exchange. Details on the synthesis method can be found in **Chapter 4**. The following observations were made:

Throughout the ion exchange steps, the zeolite remained a solid in suspension. In the filtering step, the white zeolite powder was collected and only after pre-treatment the catalyst changed to the characteristic light grey colour which indicates the Pt ions have reduced to Pt.

5.3.1 TEM

STEM-BF and HAADF images of the reduced Pt on MFI after pre-treatment and CO chemisorption (**Pt-CIE/MFI CO Chemi**) can be seen in *Figure 5.21*. Standard TEM was deemed insufficient in the analysis of this sample as the MFI support masks the very small Pt NPs and atoms/clusters.

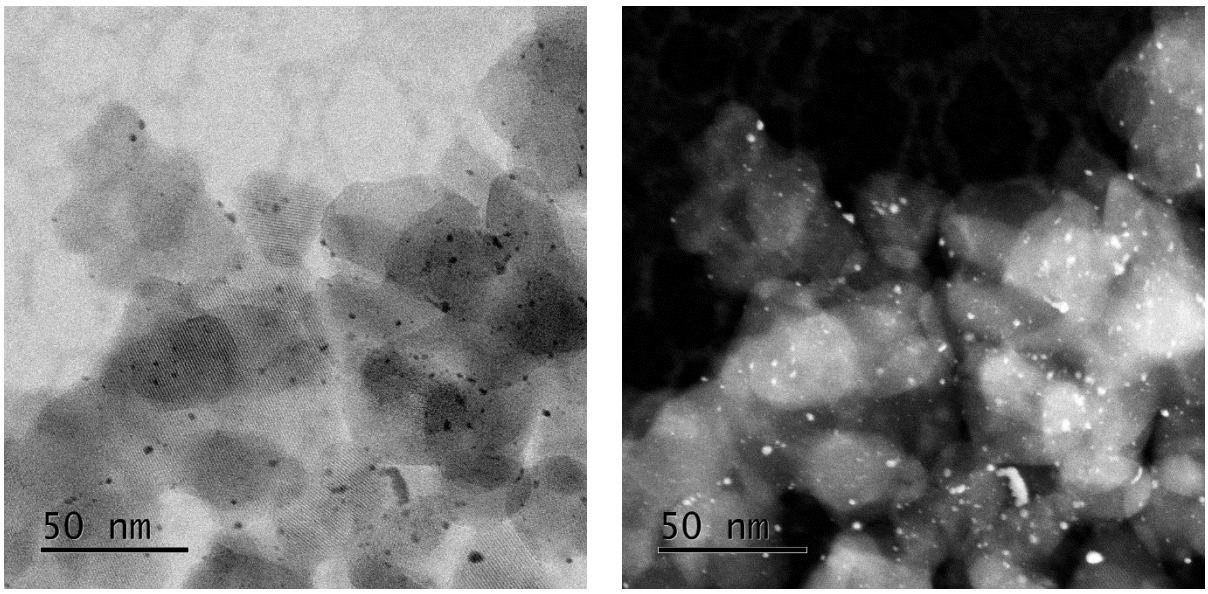

Figure 5.21: STEM-BF and HAADF images of Pt-CIE/MFI after an oxidation/reduction pre-treatment and CO chemisorption.

A good dispersion of small Pt NPs is visible from the STEM-BF image on the left. Furthermore, smaller white dots from the HAADF image on the right confirm evidence of smaller Pt clusters. These results are expected as the ion exchange method atomically disperses the Pt within the MFI structure and after pre-treatment some sintering is expected - which in this case formed 1-2 nm Pt

NPs. A particle size distribution from the microscopy images is not conducted as the smaller Pt clusters/atoms are difficult to measure and only measuring the bigger particles gives a skewed view on the actual particle size distribution. CO chemisorption is therefore used (**Section 5.3.3**) as a bulk technique for measuring the average Pt particle size.

5.3.2 ICP-OES

The ICP-OES results for **Pt-CIE/MFI** are displayed in Table 5.6. Comparing the Pt in versus the wt. % out, the Pt yield is high at 85 %, showing that not much metal is lost in the washing cycles using the filter press method.

Table 5.6: ICP-OES Results for Pt-CIE/MFI

Pt In/ Zeolite In (wt. %)	**ICP-OES Analysis after Supporting & Cleaning**				**Pt Yield (%)**
	Sample Mass (mg)	Volume (l)	Dilution Factor	Content (wt. %)	
0.91	50.8	0.1	neat	**0.78**	85

5.3.3 CO Chemisorption

The CO chemisorption results for **Pt-CIE/MFI** after a simulated pre-treatment can be seen in *Figure 5.22*.

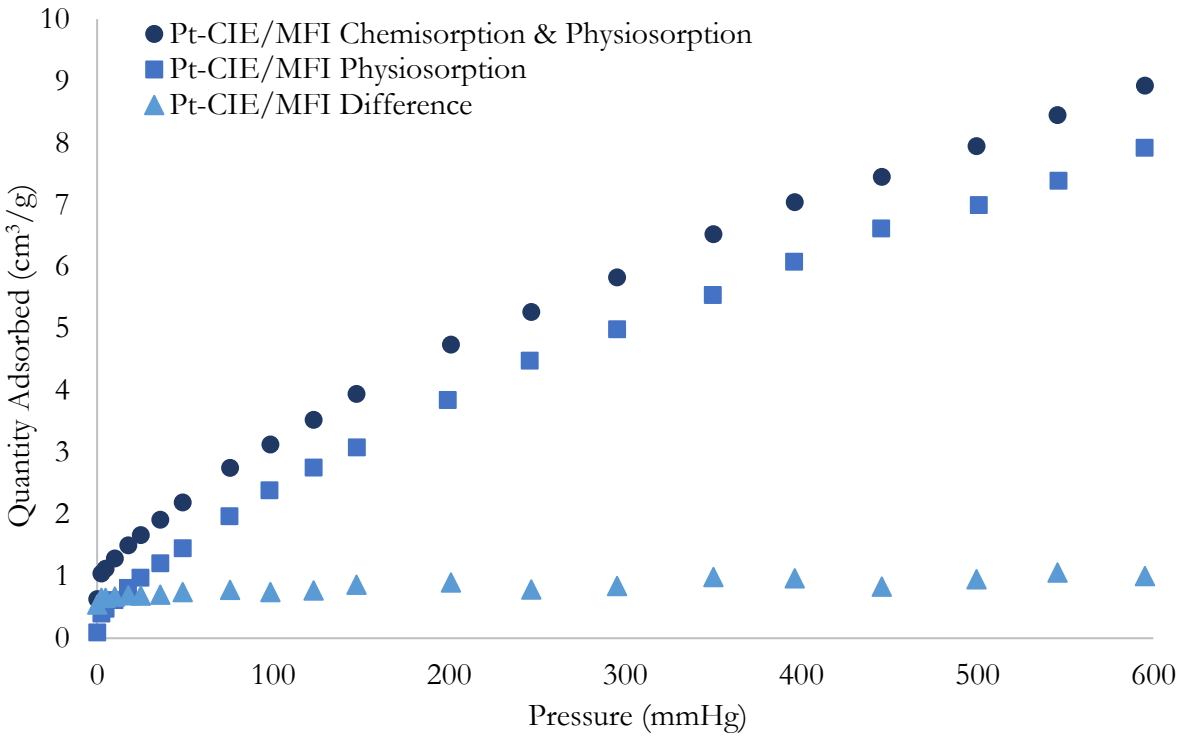

Figure 5.22: CO chemisorption on Pt-CIE/MFI. Oxidation at 0.4 °C/min to 300 °C, hold 30 mins and reduction at 0.4 °C/min to 300 °C, hold 30 mins.

Two isotherms are recorded, first the chemisorption & physisorption (circles) followed by the physisorption only (squares). The difference of these two is calculated and displayed (triangles). The calculated particle size was determined as seen in Table 5.7.

Table 5.7: CO Chemisorption for Pt-CIE/MFI

Catalyst	ICP-OES (wt. %)	CO Chemisorption		
		Quantity Adsorbed (cm^3/g STP)	Dispersion (%)	Particle Size (nm)
Pt-CIE/MFI	0.85	0.96	93.31	1.23

The average particle size at ~1.23 nm is expected as the result takes into account atoms, small clusters, and Pt NPs of 1-2 nm.

5.4 CHAPTER 5 SUMMARY AND OVERALL DISCUSSION

The aim of this chapter was to place small Pt NPs exclusively inside and outside of MFI micropores. This was achieved by the following two catalyst synthesis methods which are summarised in Table 5.8.

Table 5.8: Summary of Final Catalysts with Pt Exclusively Inside and Outside MFI Micropores

Location	Catalyst Name	Synthesis Method	Particle Diameter (nm)	Justification for Location
Outside	PtNPs-OCA/MFI	1. Pre-synthesis of Pt NPs in EG 2. Capping of Pt NPs in OCA 3. Supporting, cleaning and pre-treatment	TEM: 1.48 ± 0.28 CO Chemi: ~1.25	No TEM evidence of particles smaller than MFI micropore diameter of 0.55 nm
Inside	Pt-CIE/MFI	1. Transfer of H-MFI to Na-MFI 2. Competitive ion exchange 3. Pre-treatment	CO Chemi: ~1.23	Pt NPs are exchanged into the MFI framework which has a much larger internal area

Pt was placed outside the MFI micropores using pre-synthesised Pt NPs which are too big to fit inside the micropores. Whereas, Pt was placed inside the micropores by competitive ion exchange within the MFI structure.

To compare metal location effects, it was attempted to keep all other variables constant. However, Pt particle size was one parameter which was difficult to control due to the varying nature of the synthesis procedures. Using colloidal chemistry, it is possible to achieve monodisperse Pt NPs of uniform size but with ion exchange, the Pt size varies between atoms, clusters and NPs. Therefore, mean Pt diameter had to be used to compare particle size with a target of ~1.2 nm, which is the size for the wet impregnation literature comparison (**Pt/MFI**). Therefore, using this comparison the samples are all in good agreement with particle means between 1.2 – 1.5 nm. Furthermore, as discussed in **Chapter 2**, it is expected that under ideal hydrocracking particle size does not affect activity or selectivity.

The OMCVD technique was also attempted for placing Pt exclusively outside the MFI micropores. The method successfully produced Pt NPs with a particle diameter mean close to the target at 1.57±0.42 nm. However, TEM imaging confirmed that Pt clusters were present – meaning the Pt NPs are not homogeneous and there is no guarantee that the Pt is exclusively outside.

Chapter 6

Metal Location in n-C_{16} Shape Selective Hydrocracking

To investigate the effects of metal location, the metal was supported using MFI and NSs in different ways. In the previous chapter, it was confirmed that Pt was successfully placed inside and outside the micropores using characterisation techniques. In this chapter, a comparison of metal location in normal hydrocracking and hydrocracking in the presence of H_2O will be presented and discussed. A comparison of metal location in the presence of H_2O on MFI and NS will also be presented to determine if the NSs affect the outcome of the metal location results. The catalyst performance will be determined as follows: activity is compared using conversion vs temperature graphs and Arrhenius plots. Primary hydrocracking is assessed using C_4/C_{12} versus yield/conversion graphs and if primary cracking is achieved, selectivity can be compared by analysing the branched and linear products.

6.1 Quantifying the Metal Location Effect in Shape Selective n-C_{16} Hydrocracking

Hydrocracking of the model reactant, n-C_{16}, over Pt supported on MFI in the absence and presence of H_2O is used in this study to get a better understanding of the effects of metal location.

6.1.1 Summary of Catalysts

Several methods were used to prepare Pt supported on MFI catalysts with varying Pt location – as presented in **Chapter 5**. Table 6.1 shows a summary of the catalysts prepared for determining metal location effects in n-C_{16} hydrocracking. A dry weight of 1.0 g was used for each catalyst to ensure ideal plug flow.

Table 6.1: Summary of Pt Supported on MFI Catalysts for Performance Determination

Metal Location	Catalyst Name	Preparation Method	Average Particle Diameter from CO Chemi (nm)	Metal Loading (wt. %)
Outside	**PtNPs/MFI**	Pre-synthesised Pt NPs by colloidal chemistry with OCA capping	~1.25	1.2

Inside and Outside	**Pt/MFI**	Wet impregnation	~1.20	0.9
Inside	**Pt-CIE/MFI**	Competitive ion exchange	~1.23	0.8

PtNPs/MFI and **Pt-CIE/MFI** were prepared in this study by following established literature methods, as discussed in detail in **Chapter 5**. **Pt/MFI** was prepared and analysed by Brosius *et al.*, 2016 and the results are included in the graphs of this study to provide a benchmark for comparison. Comparing the three catalysts, the CO Chemisorption average particle diameters are all extremely close at ~1.2 nm. These diameters are considered close enough to remove any particle size effects, even though it is expected that in an ideal hydrocracking scenario the metal sites are not rate limiting (as discussed in **Chapter 2**). More importantly, with similar sized NPs and metal loading close to 1 wt. % (1.0±0.2 wt.%), the metal dispersion across the MFI supports is considered similar enough to exclusively observe metal location effects.

The Pt NPs prepared by colloidal chemistry using PVP as a capping agent (Rioux *et al.*, 2005) and the Pt NPs prepared by OMCVD were also tested in n-C_{16} hydrocracking. The results are presented in **Appendix 6** in comparison to **PtNPs-OCA/MFI**, which were found to be the most appropriate for testing metal location effects as the particles are between 1-3 nm after pre-treatment and are exclusively outside the micropores (as discussed in **Chapter 5**). Comparing activity, **PtNPs-OMCVD** showed higher conversion than **PtNPs-PVP/MFI** and **PtNPs-OCA/MFI**, which showed very similar activities. The increase in activity may be because OMCVD Pt NPs did not require a capping agent and may have more active metal surface area. Comparing the samples in hydrocracking selectivity, it is evident that they all show similar results (achieving ideal hydrocracking in the presence of H_2O). Furthermore, looking at the yield of linear alkanes, it is evident that all the samples again show very similar results. The similarities in selectivity suggest two things: (1) **PtNPs-OMCVD**, even though they have some smaller clusters of Pt, must have most of the metal on the outside to show such similar results to the other samples (2) Particle size changes do not have a large effect on activity or selectivity as the results for **PtNPs-PVP/MFI** and **PtNPs-OCA/MFI** are very similar.

6.1.2 Activity

The catalysed hydrocracking performance is determined by analysing the product stream at varying reactor temperatures (as described in **Chapter 4**). A good view into the overall catalyst activity under ideal plug flow can be seen in *Figure 6.1*, which compares the overall reactant conversion at varying temperatures for the samples in the absence and presence of H_2O. Conversions can be used for comparison because the catalyst mass in each experiment was consistent (van Steen, 2014).

Overall in dry hydrocracking, all three samples show low (close to 0 %) and high (close to 100 %) conversions between 180 - 240 °C. Whereas, in the presence of H_2O, all three samples have experienced a decrease in activity with the low and high conversions shifted between 220 - 290 °C. Comparing the samples against one another in dry hydrocracking at a constant temperature shows that the activities are relatively close. **Pt/MFI** is the most active ($X_{215°C}$ is 41 %) followed by **Pt-CIE/MFI** ($X_{215°C}$ is 35 %) and then **PtNPs/MFI** ($X_{215°C}$ is 34 %). However, in the presence of

H_2O, **PtNPs/MFI** ($X_{245°C}$ is 18 %) has shown much stronger deactivation than the other two samples: **Pt-CIE/MFI** ($X_{245°C}$ is 43 %) and then **Pt/MFI** ($X_{245°C}$ is 52 %).

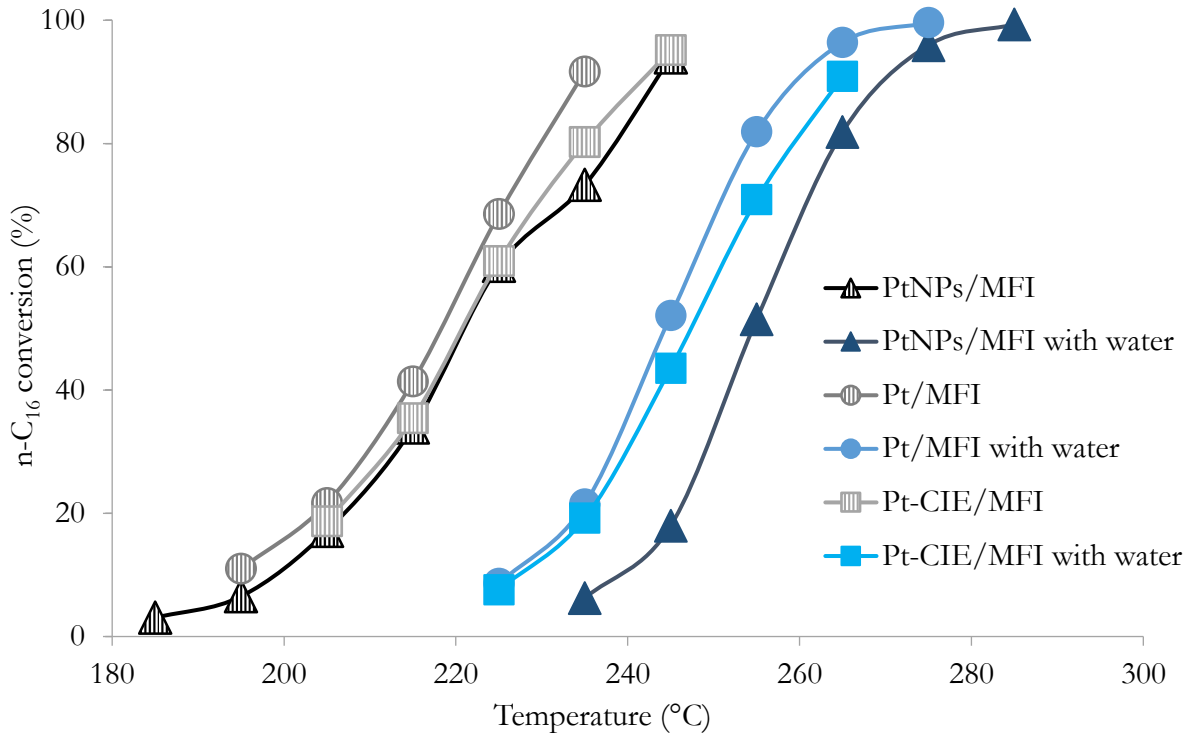

Figure 6.1: Light-off curves in the absence (grey) and presence (blue) of H_2O over PtNPs/MFI, Pt/MFI, and Pt-CIE/MFI.

The overall drop in activity when adding H_2O is expected, as H_2O was shown to suppress activity in hydrocracking over **Pt/MFI** by ~ 30 °C in Brosius *et al.*, 2016. In comparing the individual samples, the general similarity in the light off curves in dry hydrocracking suggests that in this case the metal location is not strongly influencing overall n-C_{16} conversion. This suggests that the rate limiting step is the isomerisation and cracking step at the acid sites. Whereas, in the presence of H_2O, **PtNPs/MFI** shows significantly more deactivation than the other samples. **PtNPs/MFI** has all the metal outside the micropores, which suggests that diffusion limitations between metal and acid site might be influencing the rate when H_2O is deactivating the acid sites. The reason **Pt/MFI** and **Pt-CIE/MFI** show similar results under H_2O is because the metal sites are expected to be quite well dispersed inside the micropores for both samples, decreasing diffusion limitations. The amount of metal inside vs outside the micropores in **Pt/MFI** will be further explored in hydrocracking product selectivity. However, in terms of activity, it appears that the amount of metal outside is not enough to affect the results which are very similar to **Pt-CIE/MFI**, which is known to have metal mostly inside the micropores.

The intrinsic rate of reaction is another measure of catalyst activity which relates the amount of reactant converted per unit time per mass catalyst. *Figure 6.2* relates the intrinsic rate of reaction to temperature in an Arrhenius plot for the samples in n-C_{16} hydrocracking in the absence and presence of H_2O.

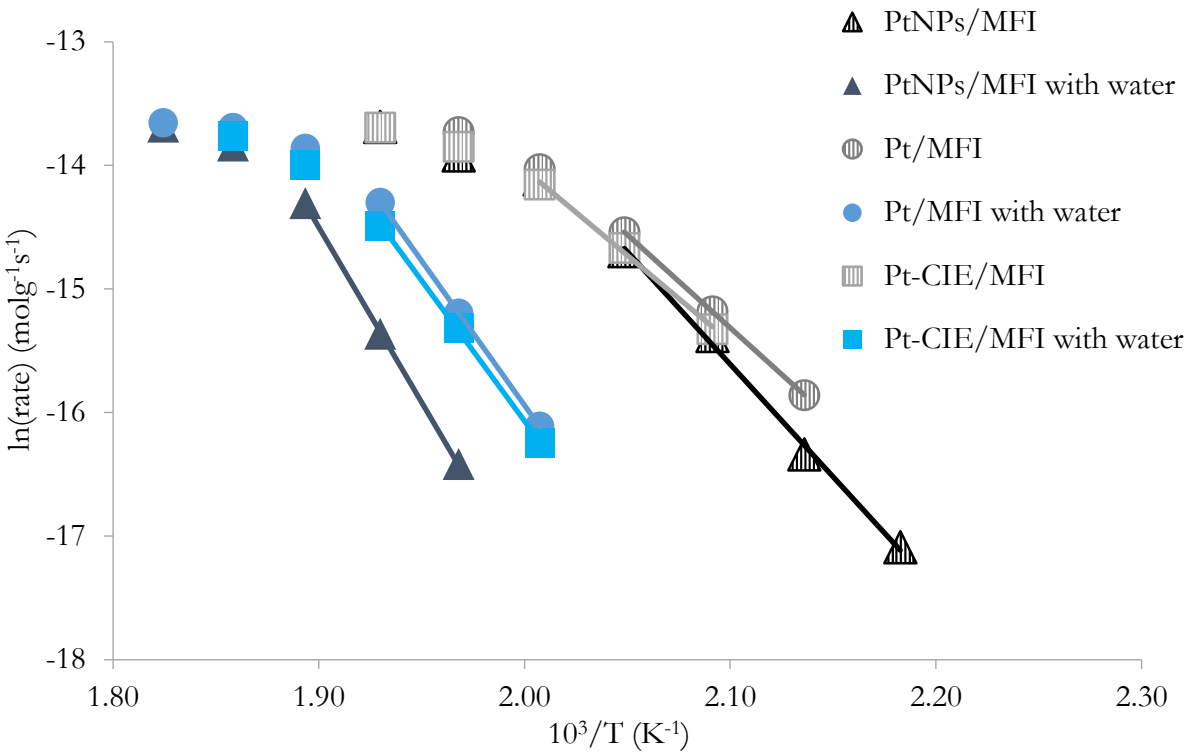

Figure 6.2: Arrhenius plot for n-C_{16} hydrocracking in the absence (grey) and presence (blue) of H_2O over PtNPs/MFI, Pt/MFI and, Pt-CIE/MFI.

The Arrhenius plots are in good agreement with the light off curves showing the same trends of higher activity with dry hydrocracking in the order of **Pt/MFI** ($r_{215°C}$=4.8x10^{-7} mol/g.s), **Pt-CIE/MFI** ($r_{215°C}$=4.3x10^{-7} mol/g.s) and then **PtNPs/MFI** ($r_{215°C}$=4.2x10^{-7} mol/g.s). Similarly, in wet hydrocracking, the activity decreased more for **PtNPs/MFI** ($r_{245°C}$=2.13x10^{-7} mol/g.s) followed by **Pt-CIE/MFI** ($r_{245°C}$=5.10x10^{-7} mol/g.s) and **Pt/MFI** ($r_{245°C}$=6.16x10^{-7} mol/g.s).

Furthermore, from the Arrhenius plot, the gradient for each sample is representative of the activation energy, as shown in Table 6.2.

Table 6.2: Activation Energy for MFI Samples with Varying Pt Location

Sample	**~ Activation Energy (kJ/mol)**		
	Absence of H_2O	Presence of H_2O	Difference
PtNPs/MFI	155	230	74
Pt/MFI	125	194	69
Pt-CIE/MFI	116	189	73

The difference in activation energy between hydrocracking in the absence and presence of H_2O is 72±3 kJ/mol. This value is in good agreement with the isosteric heat of adsorption of H_2O on MFI with hydrophilic sites and water coverage which is between 55 – 70 kJ/mol (Ahunbay, 2011). Furthermore, in the absence of H_2O, the activation energies are all above 100 kJ/mol, which is a good indication that no external diffusion limitations are present for these samples, as discussed in **Chapter 4**.

6.1.3 Isomerisation and Cracking Products

The first step in the hydrocracking mechanism is the isomerisation of n-C_{16} before the first cracking step can take place (as discussed in **Chapter 2**). A significant portion of the n-C_{16} reactant which forms iso-C_{16} does not crack further (sometimes up to ~30 %). This is best represented by *Figure 6.3*, which shows the yields of iso-C_{16} and cracked products (C_1-C_{15}) versus n-C_{16} conversion for **PtNPs/MFI**, **Pt/MFI** and **Pt-CIE/MFI**.

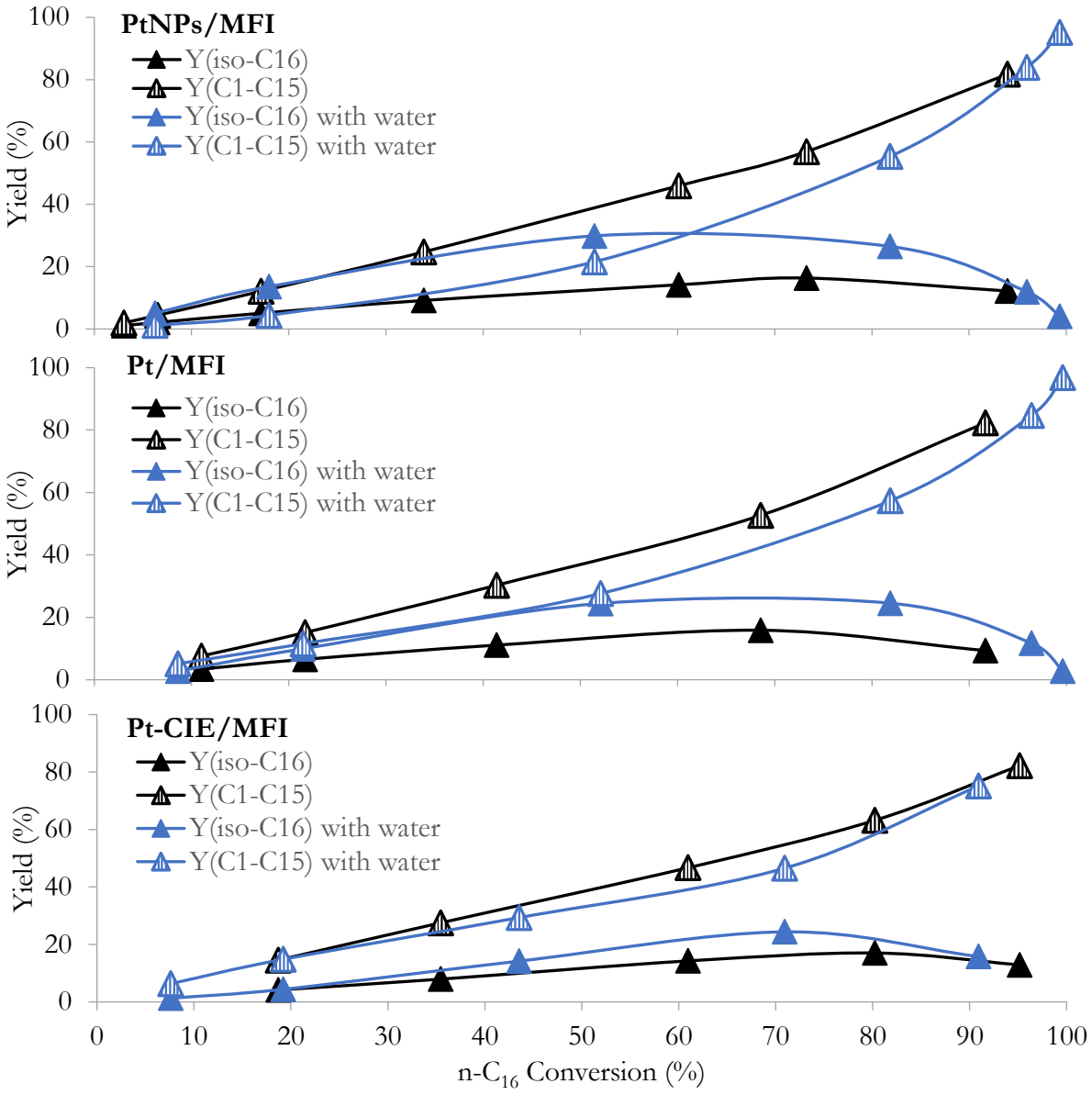

Figure 6.3: Yields of isomerised, Y(iso-C_{16}), and cracked, Y(C_1-C_{15}), products against n-C_{16} conversion in the absence (black) and presence (blue) of water for PtNPs/MFI, Pt/MFI and Pt-CIE/MFI.

The overall trend for all three catalyst samples is similar and shows that the yield of cracked products, Y(C_1-C_{15}), and isomers, iso-C_{16}, both increase with increasing conversion. The yield of isomers however, only increases with increasing conversion up to a certain point before reaching a maximum and lowering off again. The lowering off at high conversion occurs as the iso-C_{16} products are cracked to further increase cracking conversion.

In the presence of H_2O, isomer yields are higher for all MFI samples and the isomer yields decrease in the order of **PtNPs/MFI**, **Pt/MFI** and, **Pt-CIE/MFI**. The increase in isomer yields due to H_2O is suggested to be effected by the competitive adsorption of H_2O, which facilitates the desorption of iso-C_{16} and thereby impeding consecutive cracking (Brosius *et al.*, 2016). The order of decreasing isomer yields further suggests that when metal is outside the micropores more iso-C_{16} is produced than when metal is on the inside of the micropores. This result will be further discussed when comparing metal location for its effect on secondary isomerisation.

The next set of results is a deep dive into the products which do proceed through the first cracking step (meaning they are no longer iso-C_{16}), as these products have the potential to form the desired products (linear diesel fragments).

6.1.4 Achieving Primary Hydrocracking

The degree of secondary cracking is measured as a ratio of C_4 to C_{12} products versus conversion of the feed (n-C_{16}) as shown in *Figure 6.4*. Primary cracking is indicated as a ratio of 0.33, as described in **Chapter 4**.

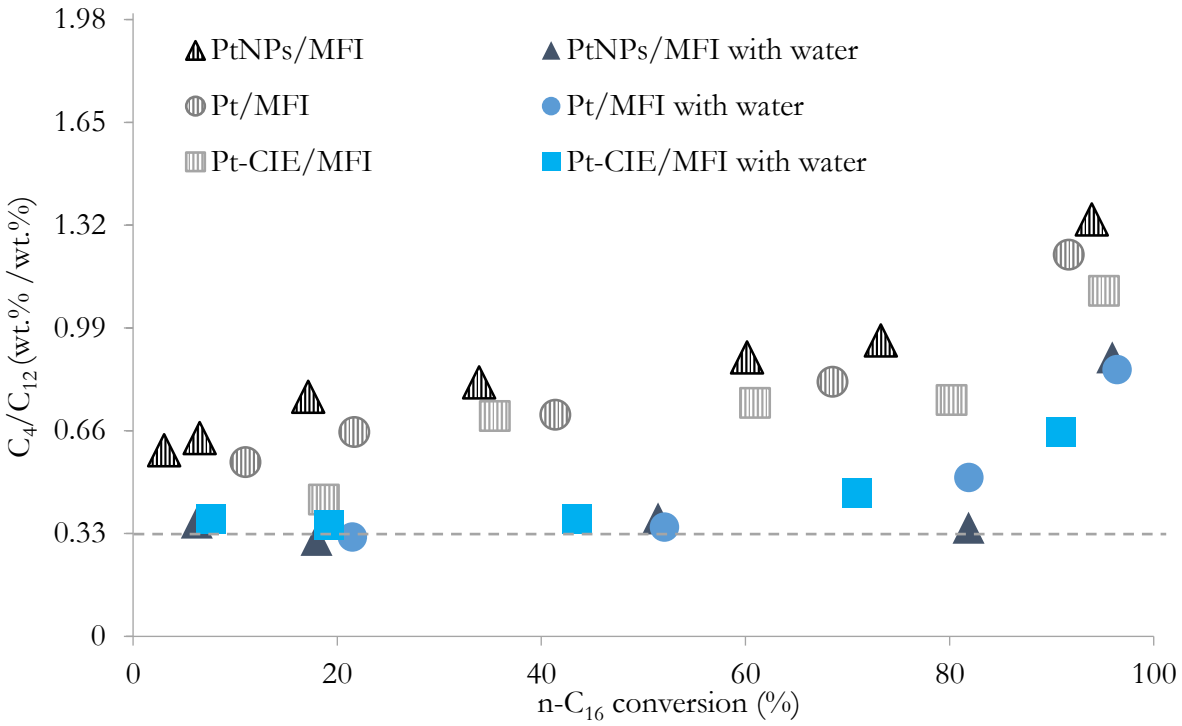

Figure 6.4: Degree of secondary cracking in the absence (grey) and presence (blue) of H_2O over PtNPs/MFI, Pt/MFI and, Pt-CIE/MFI.

Overall, for all the catalyst samples, the amount of secondary cracking increases with increasing conversion. For dry hydrocracking, **PtNPs/MFI** shows slightly more secondary cracking than **Pt/MFI** and **Pt-CIE/MFI** at all conversions. In comparing hydrocracking in the absence and presence of H_2O, it is evident that secondary cracking is eliminated in the presence of H_2O at lower conversions (up to 60 %) for all three catalysts.

PtNPs/MFI is underperforming in dry hydrocracking, most likely due to diffusion limitations between metal and acid sites. Primary cracking in the presence of H_2O was achieved as H_2O

competes for adsorption on the acid sites of the MFI, forcing the primary cracked products to desorb and move out of the MFI pores, as discussed in **Chapter 2** (Brosius *et al.*, 2016). It is evident that, regardless of metal location, primary cracking is still achieved in the presence of H_2O – showing for this particular system, that diffusion limitations between metal and acid sites are not influential enough to prevent ideal hydrocracking.

6.1.5 Secondary Isomerisation Selectivity

Since primary cracking is achieved for all three samples in the presence of H_2O, regardless of metal location, the next step is to compare product branching. After primary cracking the resultant molecule is either immediately desorbed to form a linear product after hydrogenation, or secondary isomerisation occurs before desorption, resulting in a branched product. *Figure 6.5* shows a product distribution for each catalyst sample at an n-C_{16} conversion of 45-50 %. The product molecules are grouped by length of carbon chain and then further grouped according to branching. If no branching has occurred the products are classified as 'linear,' whereas any branching is grouped under 'branched'.

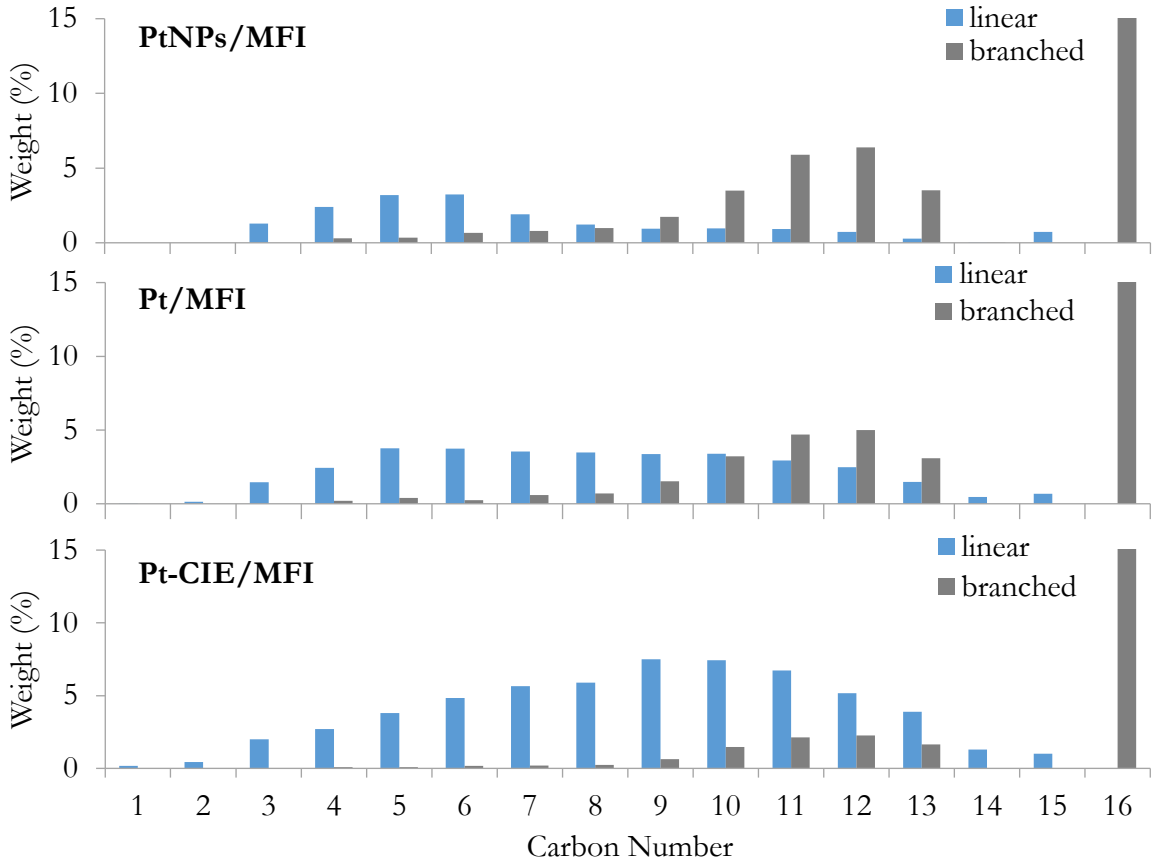

Figure 6.5: Cracking product distribution of linear (blue) and branched (grey) alkanes from primary hydrocracking with H_2O at n-C_{16} conversions between 45-50 % over PtNPs/MFI, Pt/MFI and Pt-CIE/MFI.

The product distributions demonstrate that at 45-50 % conversion, as the metal sites move from outside to inside the micropores, there is an increase in the amount of linear products across the varying carbon number products. This result is expected, as discussed in **Chapter 3**, since the

cracking steps need to occur inside the micropores for type C β-scission (giving linear cracked products) and this is much more likely when the metal is inside and the (de)hydrogenation products are released inside the micropores. Analysing the linear products against n-C_{16} conversion can be seen in *Figure 6.6*. This figure gives a better picture of what the product distribution looks like over low and high conversion and can be used to quantify the metal location effect.

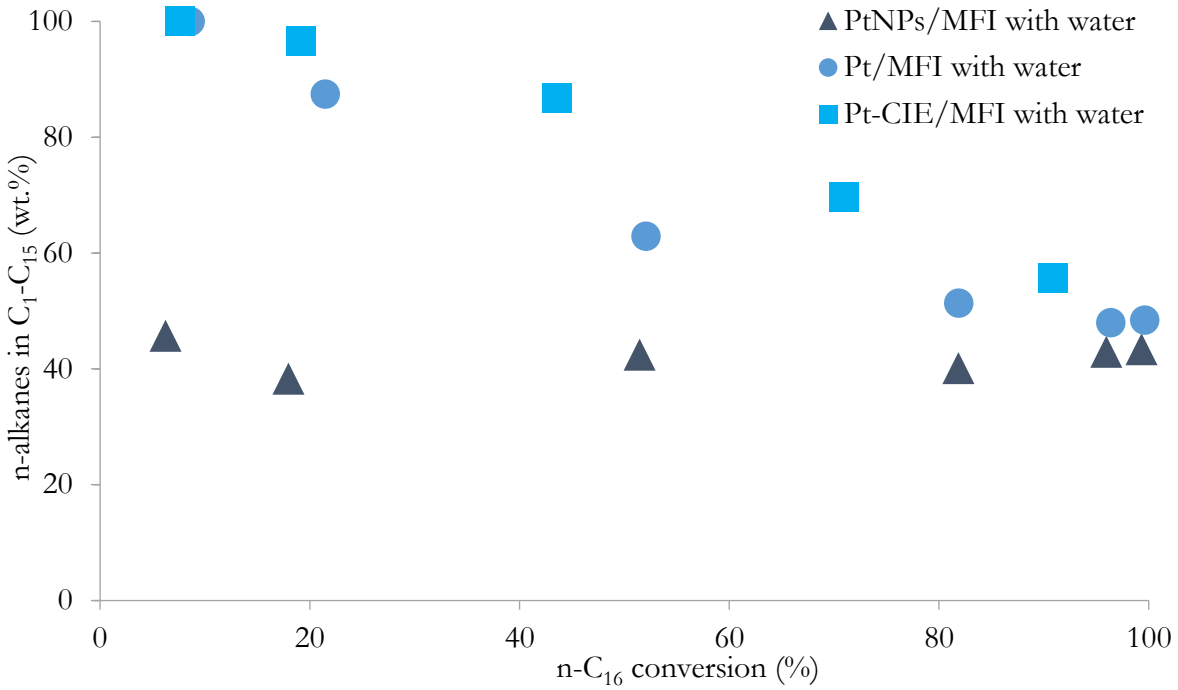

Figure 6.6: Linearity of total product distribution of primary cracking in the presence of water for PtNPs/MFI, Pt/MFI and Pt-CIE/MFI.

At low conversion, the greatest differences are seen with **Pt/MFI** and **Pt-CIE/MFI** achieving ~100 % n-alkanes in C_1-C_{15} cracked products, whereas **PtNPs/MFI** achieves only ~40 %. As conversion increases, **PtNPs/MFI** consistently produces around 40 % linear products, whereas the **Pt-CIE/MFI** and **Pt/MFI** samples experience reductions in linear products from ~100 % to ~50 %. **Pt-CIE/MFI** retains the highest percentage of linear products with increasing conversion; showing the greatest improvement at ~50 % conversion with ~40 % more linear products than **Pt/MFI** and **PtNPs/MFI**.

The C_{12} fragment, which is the most prone to adsorption on acid sites as it is the longest primary cracking product, provides a good window into the effects of metal location on prohibiting secondary isomerisation. Since, linear products are only achieved with type C β-scission and then prevention of secondary isomerisation. *Figure 6.7* shows the results for the percentage of n-C_{12} products versus cracking yield.

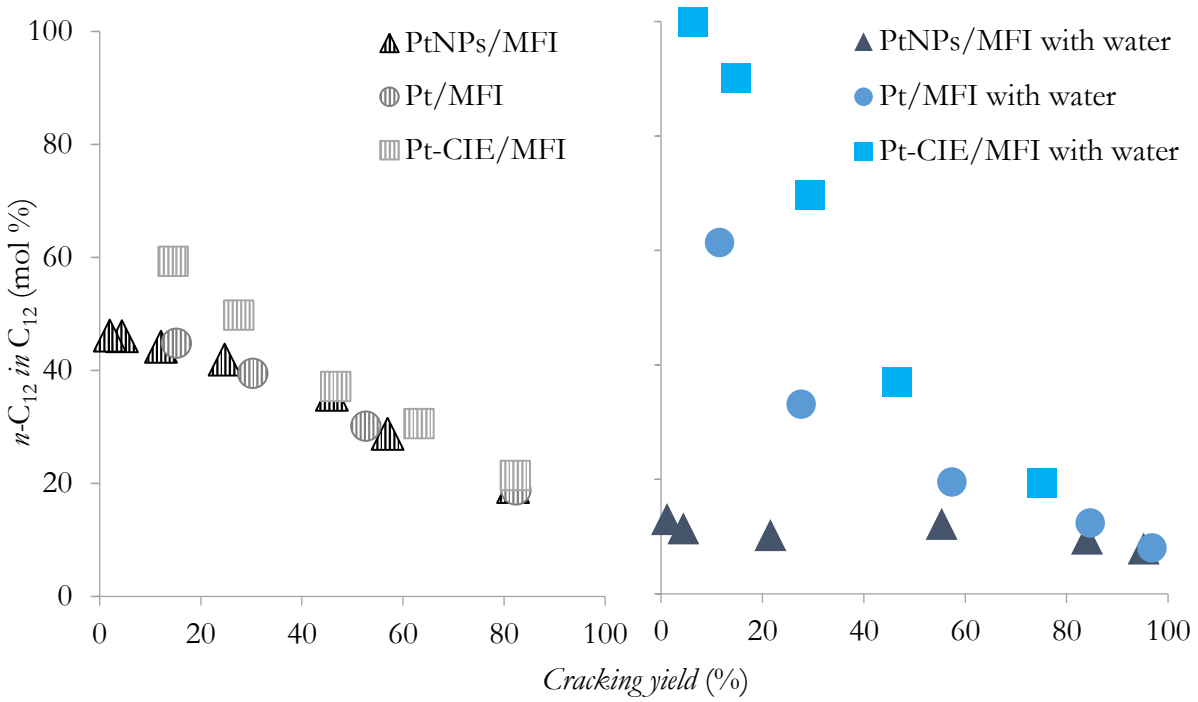

Figure 6.7: Content of linear n-C_{12} in the C_{12} hydrocracking product fraction in the absence (grey) and presence (blue) of water over PtNPs/MFI, Pt/MFI and Pt-CIE/MFI.

These results show that, in the presence of H_2O, metal located inside the MFI micropores suppresses secondary isomerisation. At ~30 % cracking yield, **Pt-CIE/MFI** showed ~70 % n-C_{12} in C_{12} followed by **Pt/MFI** (~30 %) and **PtNPs/MFI** (~10 %). This confirms that metal location plays a significant role in linear cracking product selectivity for **Pt/MFI** hydrocracking in the presence of H_2O, by influencing the amount of type C β-scission and secondary isomerisation. Another interesting observation is that comparing **PtNPs/MFI** in dry and wet hydrocracking, the presence of H_2O significantly reduces the yield of n-C_{12}. This was not seen for **Pt/MFI** and **Pt-CIE/MFI** which both show increases in linear products with the addition of H_2O.

Secondary isomerisation is influenced by competitive adsorption. Therefore, the H_2O creates a competitive environment as it adsorbs on the acid sites and when the metal is inside it provides a non-hindered steady supply of new reactant molecules which are competing for acid sites. With these two factors working together, type C β-scission primary cracked products are forced to desorb from the acid site and hydrogenate to form n-C_{12}.

However, when the metal is outside, three factors may be affecting the high yield of iso-C_{12} in the presence of H_2O:

(1) <u>If hydrocracking is occurring inside the micropores</u>: H_2O is creating a competitive environment but there is not an unhindered supply of hydrogenated reactant molecules (due to metal/acid site distance) to force desorption of the primary cracking products from the micropores (Brosius *et al.*, 2016).

(2) <u>If hydrocracking is occurring near the ends of the micropores:</u> shorter primary cracked fragments are more easily removed (decreasing acid site competition) and this may leave longer fragments adsorbed for secondary isomerisation.

(3) If hydrocracking is occurring on the outside of the micropores: type A and type B β-scission can occur which results in more branched C_{12} products. This is more likely with external metal sites (Weitkamp *et al.*, 1983).

An explanation for why **PtNPs/MFI** shows a higher yield of isomerised products in wet over dry hydrocracking is most likely affected by the increase in competitive adsorption at the acid sites in the presence of H_2O. However, the result is opposite to what is expected, and this is not fully understood. It could be that H_2O is encouraging desorption of smaller fragments near the surface, with lowered diffusion limitations, and this is causing the longer fragments (like n-C_{12}) to stay adsorbed for secondary isomerisation inside the micropores.

Looking back at iso-C_{16} yields, an interesting result is seen where metal on the outside saw the highest yield of iso-C_{16} (meaning early desorption from the acid sites) but then also the highest yield of iso-C_{12} (meaning the cracked molecules were less likely to desorb). This is a contradictory result which suggests that desorption of isomerised C_{16} and desorption of the large primary cracked products is affected differently. The reason for this effect is not currently explained by the available results. The implication of this result, however, is positive in the case of **Pt-CIE/MFI** which achieves both a lower yield of iso-C_{16} and iso-C_{12}, producing instead more linear primary cracked products.

6.2 THE METAL LOCATION EFFECT IN MFI VS NS

NSs have been explored in MFI hydrocracking as a method to decrease diffusion limitations between metal and acid sites, as described in **Chapter 2** (Verheyen *et al.*, 2013).

6.2.1 Summary of Catalysts

In this study, **PtNPs/MFI** is compared with **PtNPs/NS** to assess the effects of metal location when changing micropore length. Table 6.3 shows a summary of the catalysts.

Table 6.3: Summary of Pt Supported on MFI and NS Catalysts for Performance Determination

Metal Location	Catalyst Name	Synthesis Method	Average Particle Diameter from CO Chemisorption (nm)	Metal Loading (wt. %)
Outside	**PtNPs/MFI**	Pre-synthesised Pt NPs by colloidal chemistry with OCA capping	~1.25	1.2
	PtNPs/NS		~1.10	1.2

The Pt NPs were made using an identical synthesis method but **PtNPs/NS** showed overall slightly smaller NPs, most likely due to reduced sintering in the pre-treatment. The loadings however were very similar, showing reproducibility of the contacting method. The catalyst samples are therefore appropriate for comparing metal location effects as particle size and loading are constant.

6.2.2 Activity

The activity of **PtNPs/NS** is compared with **PtNPs/MFI** by looking at n-C_{16} conversion at varying temperature in the absence and presence of H_2O, as seen in *Figure 6.8*. The light off curve

for the **PtNPs/NS** sample shows a significantly lower activity than **PtNPs/MFI** with a temperature range of 185 - 245 °C versus 205 – 255 °C in dry hydrocracking and 255 - 305 °C versus 235 – 255 °C in wet hydrocracking. Comparing conversions at specific temperatures, in dry hydrocracking, **PtNPs/MFI** had $X_{215°C}$ ~34 %, whereas **PtNPs/NS** had $X_{215°C}$ ~10 %. In the presence of H_2O, **PtNPs/MFI** had $X_{255°C}$ ~51 % and **PtNPs/NS** had $X_{245°C}$ ~3.4 %. The significant difference is attributed to a loss in acid site activity during the NS synthesis. It is assumed that the selectivities can be discussed independently of the lower activity of this particular batch of NSs, as fewer acid sites actually help to establish ideal hydrocracking.

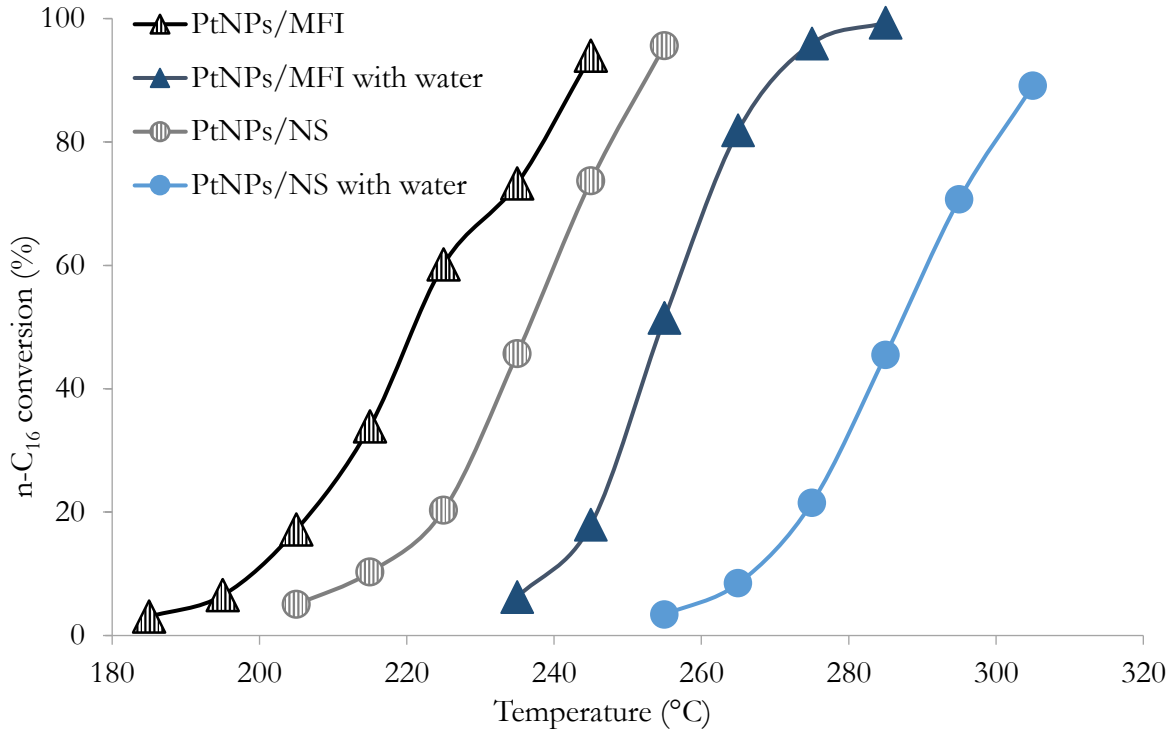

Figure 6.8: Light-off curves in the absence (grey) and presence (blue) of H_2O over PtNPs/MFI and PtNPs/NS.

Furthermore, the intrinsic rate of reaction was determined and compared against temperature in the form of an Arrhenius plot as seen in *Figure 6.9*. The results are in good agreement with the conversion versus temperature curves showing **PtNPs/NS** to have lower activity than **PtNPs/MFI** in dry and wet hydrocracking. Comparing rates at specific temperatures in dry hydrocracking shows that **PtNPs/MFI** had $r_{215°C}=4.2x10^{-7}$ mol/g.s and **PtNPs/NS** had $r_{215°C}=1.2x10^{-7}$ mol/g.s. In wet hydrocracking, **PtNPs/MFI** had $r_{255°C}=6.1x10^{-7}$ mol/g.s and **PtNPs/NS** had $r_{255°C}=3.7x10^{-8}$ mol/g.s.

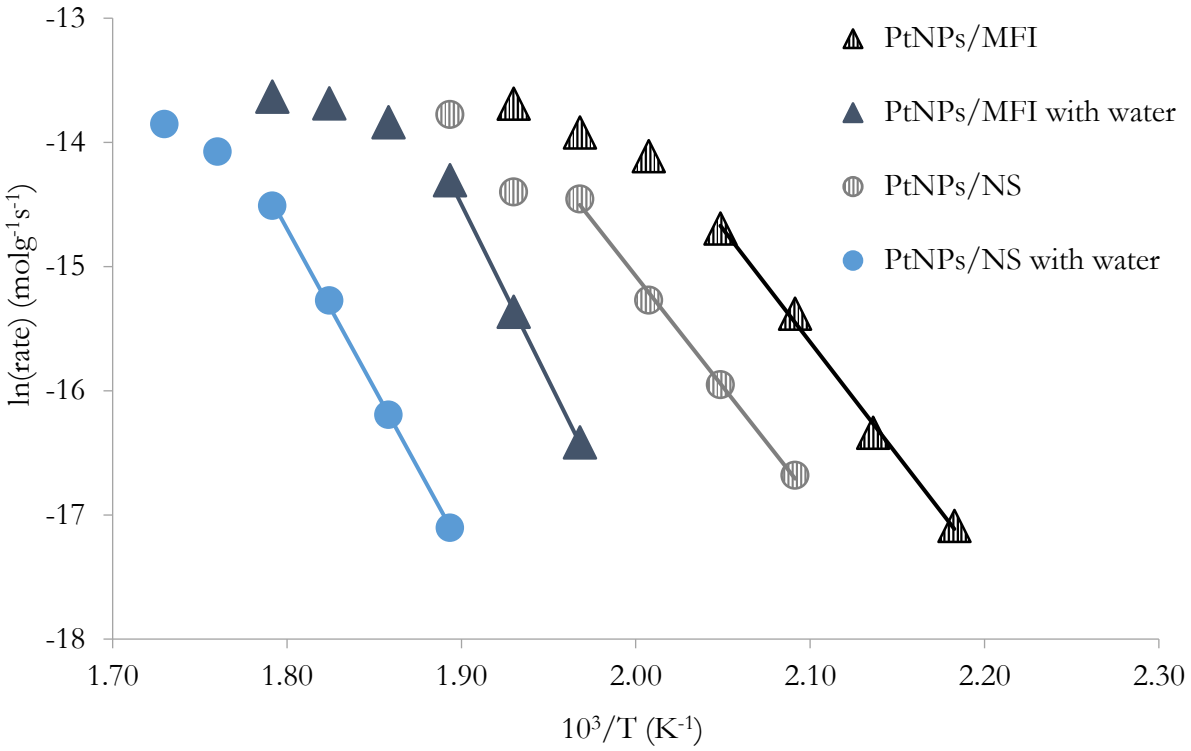

Figure 6.9: Arrhenius plot for n-C_{16} hydrocracking in the absence (grey) and presence (blue) of H_2O over PtNPs/MFI and PtNPs/NS.

The activation energies were determined as seen in Table 6.4 from the gradients of the Arrhenius plots. Similar results are seen between the two catalysts with values above ~100 kJ/mol, indicating no external mass transfer limitations. The difference values are again indicative of the isosteric heat of adsorption of H_2O on MFI with hydrophilic sites and water coverage.

Table 6.4: Activation Energies for PtNPs with Varying Support

Sample	**~ Activation Energy (kJ/mol)**		
	Absence of H_2O	Presence of H_2O	Difference
PtNPs/MFI	155	230	74
PtNPs/NS	148	213	65

6.2.3 Isomerisation and Cracking Products

The yield of iso-C_{16} and C_1-C_{15} against increasing conversion are shown in *Figure 6.10*.

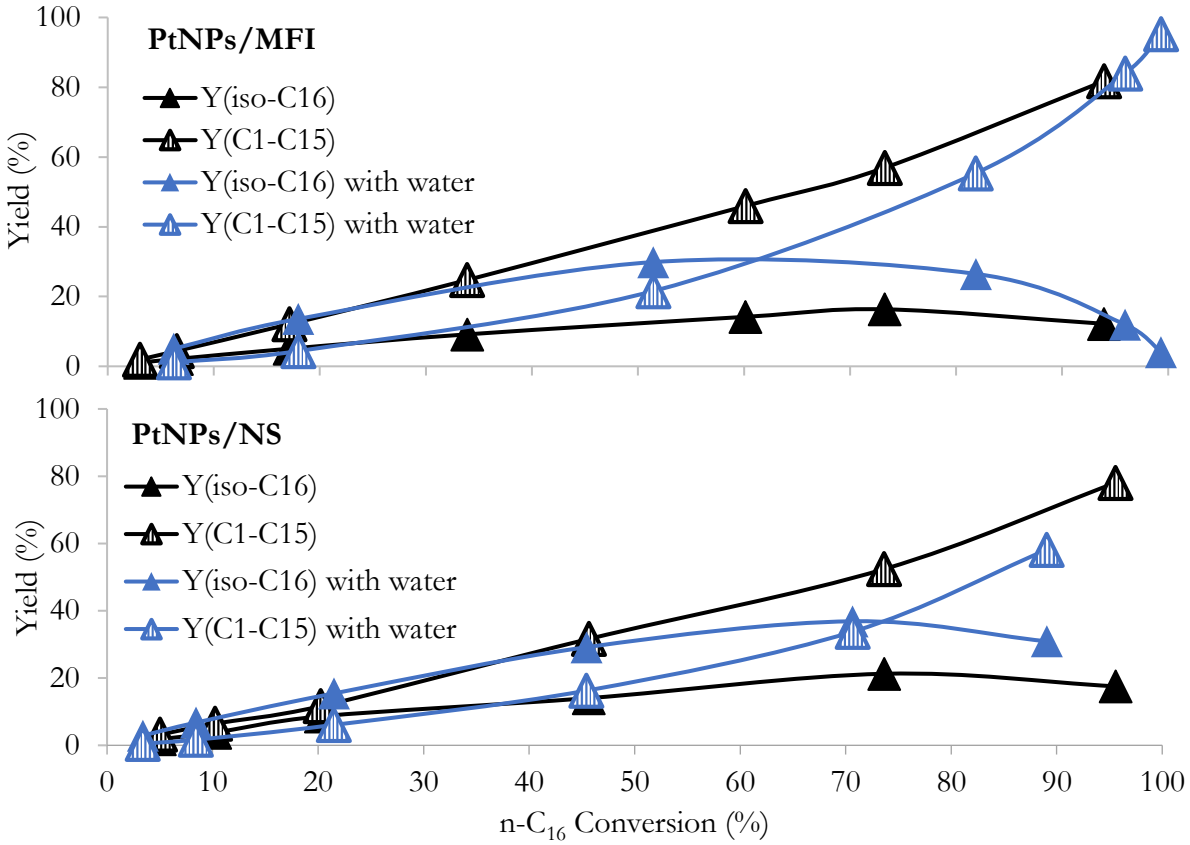

Figure 6.10: Yields of isomerised, Y(iso-C_{16}), and cracked, Y(C_1-C_{15}), products against n-C_{16} conversion in the absence (black) and presence (blue) of water for PtNPs/MFI and PtNPs/NS.

Comparing **PtNPs/MFI** with **PtNPs/NS**, similar amounts of cracked and iso-C_{16} products are seen in dry and wet hydrocracking and, as expected, both samples show an increase in iso-C_{16} in the presence of H_2O. This may suggest that the reduction in diffusion limitations between metal and acid, when using NSs, does not show any significant effect on the yield of iso-C_{16} when the metal is outside the micropores.

6.2.4 Achieving Primary Cracking

The extent of primary hydrocracking was investigated by determining the C_4/C_{12} ratio versus n-C_{16} conversion, as seen in *Figure 6.11*.

Similar results are observed as in **Section 6.1**, where primary hydrocracking is achieved in the presence of H_2O. This result is expected as the **Pt/NS** samples from Brosius *et al.*, 2016 also achieved primary hydrocracking in the presence of H_2O, showing that reduced diffusion limitations does not affect the ability for H_2O to achieve primary hydrocracking. The effects on selectivity were further investigated.

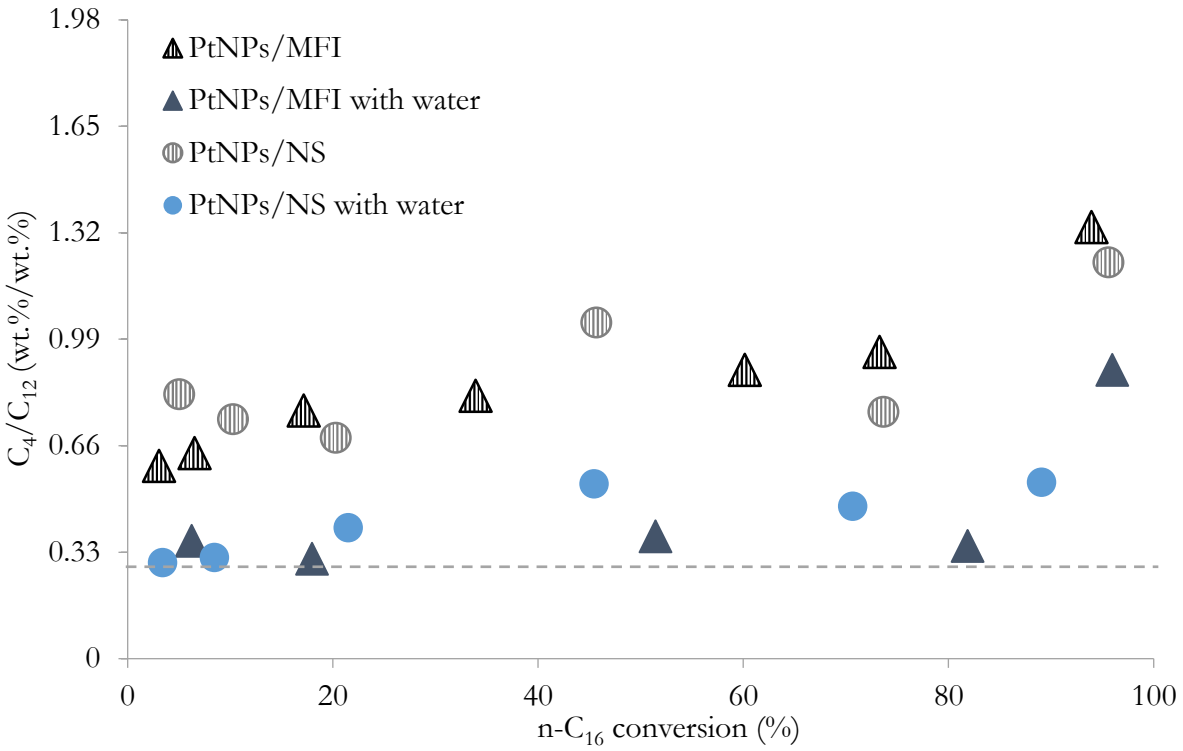

Figure 6.11: Degree of secondary cracking in the absence (grey) and presence (blue) of H_2O over PtNPs/MFI and PtNPs/NS.

6.2.5 Secondary Isomerisation Selectivity

The difference between branching and linear primary cracked products was compared by looking at the percentage of linear products in C_1-C_{15} products, as demonstrated in *Figure 6.12*.

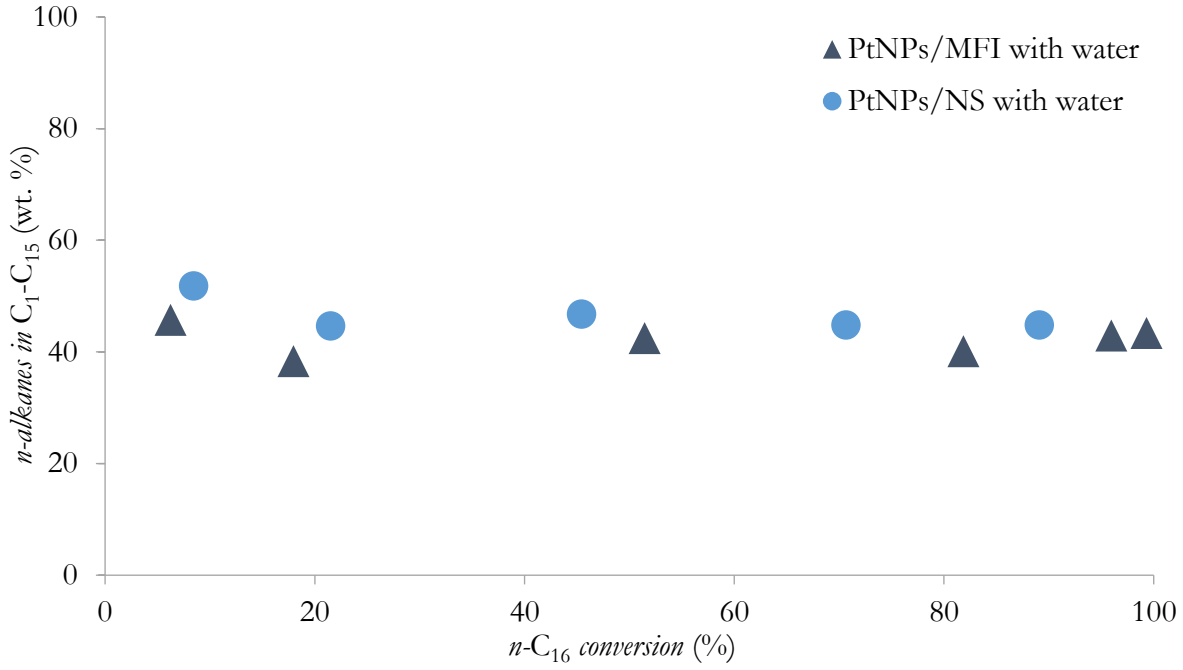

Figure 6.12: Linearity of total product distribution of primary cracking in the presence of H_2O for PtNPs/MFI and PtNPs/NS.

The results show that a similar percentage of linear primary cracked products is achieved for MFI and NS supports. The values are between ~40-50 % throughout varying n-C_{16} conversion. The amount of linear C_{12} against total C_{12} products over cracking yield is also investigated as seen in *Figure 6.13*.

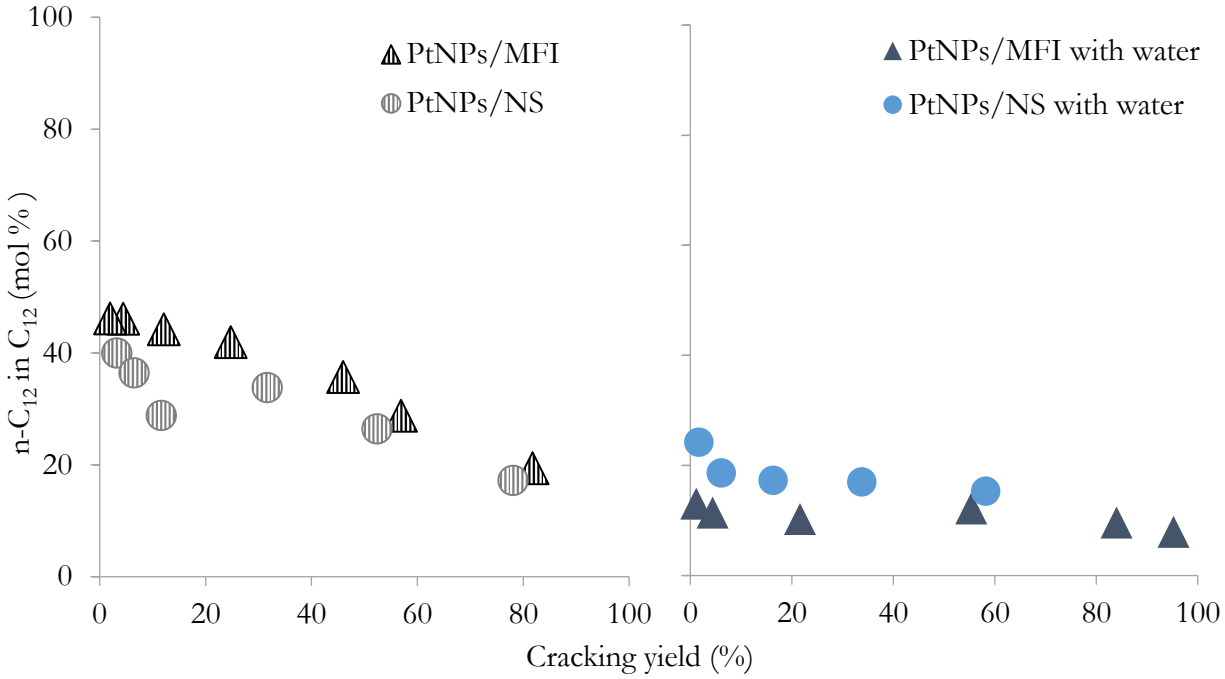

Figure 6.13: Content of linear n-C_{12} in the C_{12} hydrocracking product fraction in the absence (grey) and presence (blue) of water over PtNPs/MFI and PtNPs/NS.

Evidently, both MFI and NSs show a low ability to prevent secondary isomerisation. These results show that:

(1) Even with thin NSs there is a distinction between inside and outside metal and without metal on the inside, type C β-scission is not guaranteed
(2) The reduced diffusion limitations between acid and metal with NSs still do not provide a strong enough competition at the acid sites to ensure primary linear hydrocracking products are desorbed.

Furthermore, it was suggested in **Section 6.1** that the high secondary isomerisation seen in **PtNPs/MFI** with metal on the outside may be affected by increased hydrocracking occurring near the ends of the MFI micropores. Since, at the micropore edges, it is expected that shorter primary cracked products can more easily desorb leaving the longer fragments more prone to secondary isomerised. However, if this suggestion was true, it would make sense that with NSs there would be an even higher affinity for iso-C_{12}.

6.3 Chapter Summary and Overall Discussion

In summary, the effects of metal location were demonstrated in n-C_{16} hydrocracking over **Pt/MFI**, in the presence and absence of H_2O, by placing the metal outside the micropores with Pt NPs and inside the micropores with CIE. It was found that regardless of metal location, primary

hydrocracking could be achieved up to ~70 % n-C_{16} conversion in the presence of H_2O. Furthermore, when looking at product selectivity it was found that placing the metal on the inside (**Pt-CIE/MFI**) increased the overall linear product selectivity by 40 % (at 50 % n-C_{16} conversion) in comparison to metal outside (**PtNPs/MFI**). It was also shown that **PtNPs/NS** showed very little difference to **PtNPs/MFI**, indicating that metal inside and outside still shows significant differences even with thin NSs.

A comparison between the **Pt/MFI** catalysts with industrially found **Pt/HY** shows the impact of the findings for the difference between metal location. Looking specifically at the effect on linear n-C_{12} product yield, as shown in Figure 6.14, a clear difference is seen in the ability for **Pt/MFI** and **Pt/H-Y** to produce linear cracking products. In the presence and absence of H_2O, **Pt/H-Y** produces very little linear n-C_{12}, as there is no shape selectivity in the pores and large pores further encourage branching as the cracking molecules have space for branching. In the presence of H_2O at ~30 % cracking yield, **Pt-CIE/MFI** produces ~70 % n-C_{12} products whereas commercially used **Pt/H-Y** produces only ~11%. This is a ~60 % selectivity improvement from the industrially used catalyst at lower conversion.

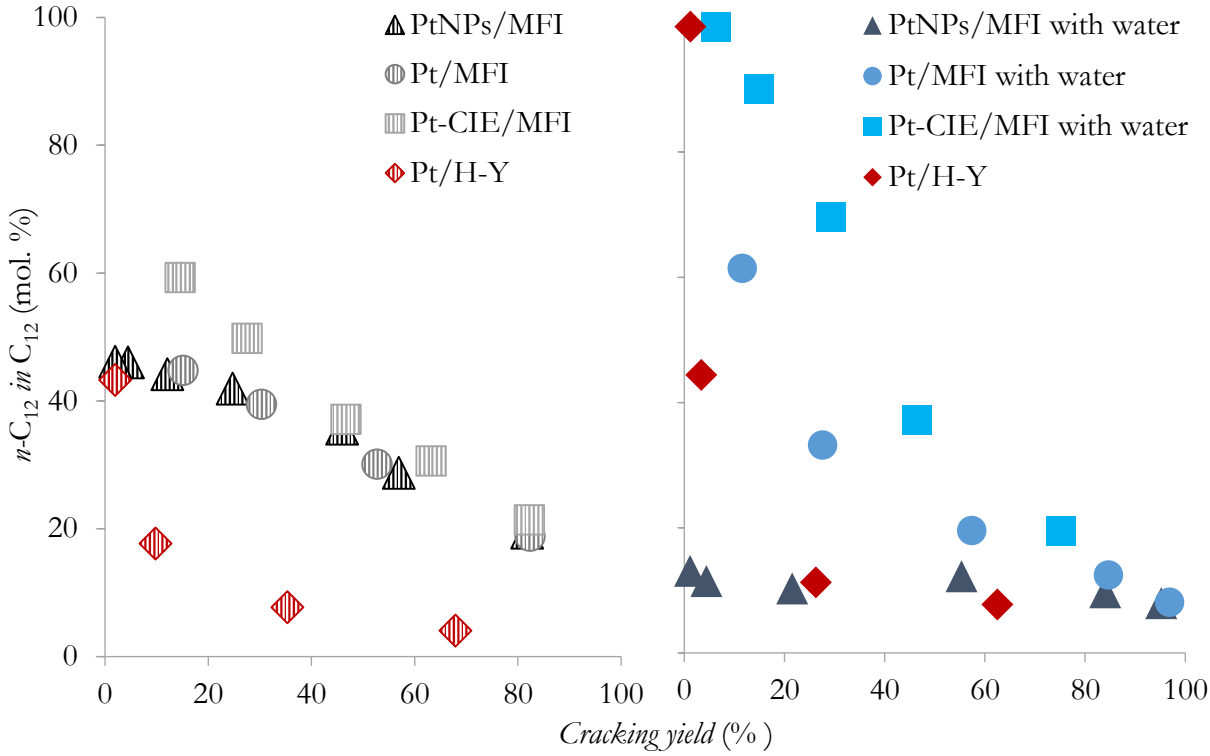

Figure 6.14: Content of linear n-C_{12} in the C_{12} hydrocracking product fraction in the absence (striped fill) and presence (solid fill) of water over PtNPs/MFI, Pt/MFI, Pt-CIE/MFI and Pt/H-Y.

Chapter 7

Post-Run Characterisation

In the previous chapter the effects of metal location inside and outside the micropores were shown to affect hydrocracking selectivity in the presence of H_2O. It is assumed throughout the previous chapter that the metal particle size is relatively consistent and in this chapter, the catalysts are analysed after hydrocracking to assess if this assumption holds. Characterisation by TEM techniques were used on the collected catalyst samples to measure the Pt NP size and check for dispersion changes.

7.1 VARYING METAL LOCATION ON MFI

The average catalyst run time to collect the data for this work was 10 days. After this period, the catalysts were removed from the reactor and analysed using TEM to ensure the catalysts did not experience any major changes- such as sintering due to exposure to elevated temperature for extended periods. The results for **PtNPs/MFI** and **Pt-CIE/MFI** will be discussed as follows.

7.1.1 PtNPs/MFI

BF-STEM and HAADF images of **PtNPs/MFI after hydrocracking** can be seen in *Figure 7.1*.

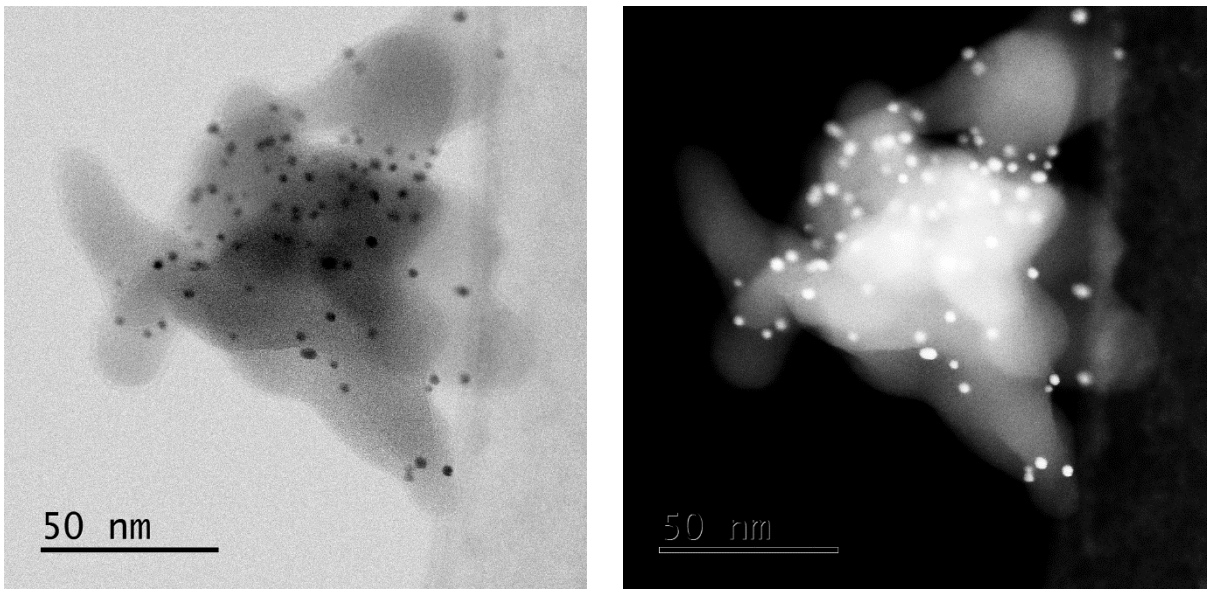

Figure 7.1: STEM-BF and HAADF images of PtNPs/MFI after 10 days of hydrocracking between 180-280 °C at 20 bar with and without H_2O.

The Pt NPs appear to be monodisperse in nature and still well dispersed on the MFI support, indicating that the catalyst did not change significantly under hydrocracking. The particle size distribution after hydrocracking is compared to the catalyst sample after oxidation/reduction pre-treatment, as seen in *Figure 7.2*.

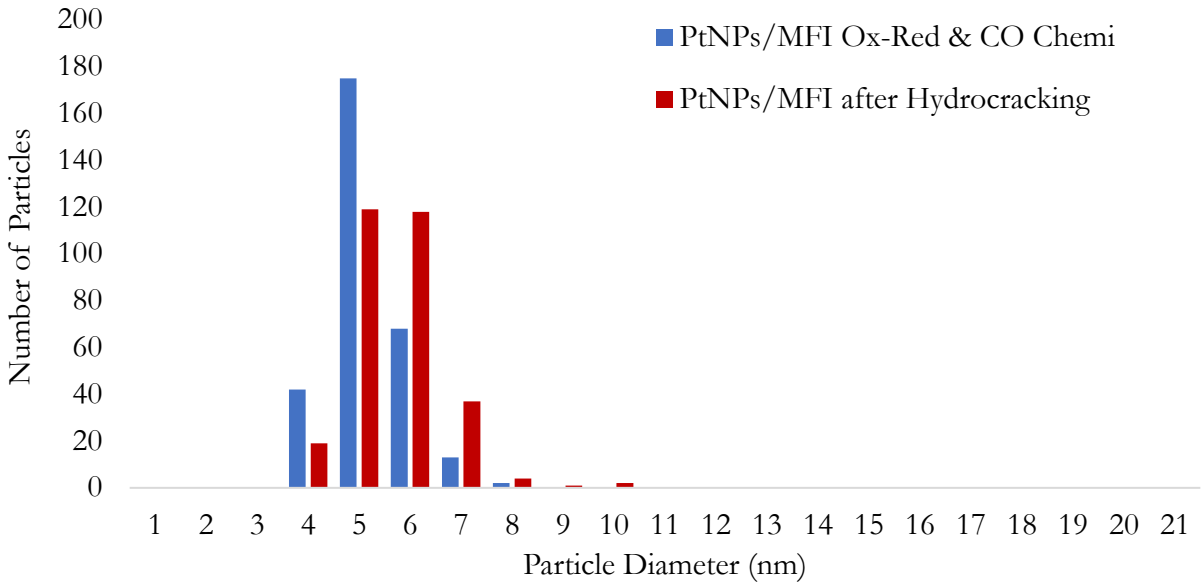

Figure 7.2: Particle size distribution of PtNPs/MFI (blue) after oxidation and reduction and CO chemisorption and (red) after hydrocracking

The sample mean for **PtNPs/MFI after Hydrocracking** is slightly larger at 1.65±0.35 nm compared to the same sample after pre-treatment: 1.48±0.28 nm. The slight increase in size may be indicative of some minor sintering but since the sample mean is still between 1-2 nm this is considered acceptable. Furthermore, it is assumed that the **PtNPs/NS** sample will show a similar result after hydrocracking as the same active metal in NP form is used.

7.1.2 Pt-CIE/MFI

BF-STEM and HAADF images of **Pt-CIE/MFI after hydrocracking** can be seen in *Figure 7.3*. A good dispersion of small Pt NPs is still visible from the STEM-BF image. Overall there was slightly less evidence of smaller Pt clusters in the HAADF images, but it is expected that this is partly due to TEM limitations on the day of imaging and then otherwise additional sintering during hydrocracking. Since the Pt NPs are still all below 2 nm, it is assumed that there has not been a significant change in the metal sites during reaction.

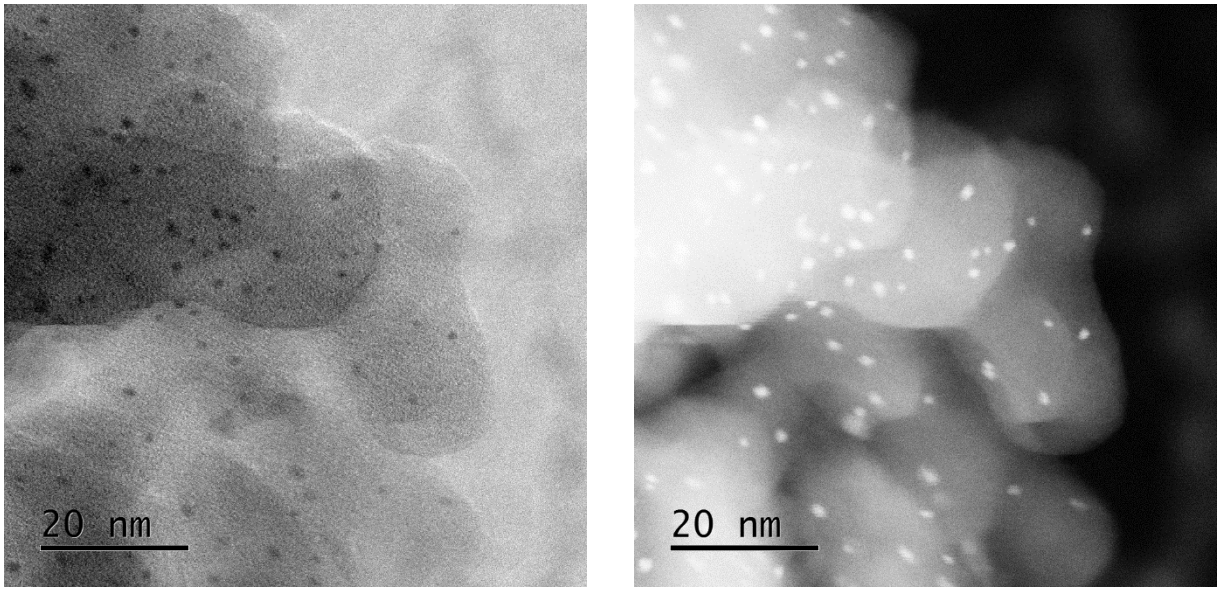

Figure 7.3: STEM-BF and HAADF images of Pt-CIE/MFI after 10 days of hydrocracking between 180-280 °C at 20 bar with and without H_2O.

7.2 CHAPTER 7 SUMMARY AND DISCUSSION

In summary, the post-mortem TEM characterisation has shown that no significant sintering occurs under hydrocracking conditions for both **PtNP/MFI** and **Pt-CIE/MFI**. It is also further assumed that **PtNP/NS** would not show further sintering during hydrocracking. Furthermore, the results are also consistent with **Pt/MFI** from Brosius *et al.*, 2016 which did not experience further sintering affects during hydrocracking.

These results validate the assumption that the Pt particle shape and size is kept consistent to test metal location affects.

Chapter 8

Conclusions and Recommendations

From the previous chapter, the post-mortem of the catalysts showed that the harsh conditions of hydrocracking do not significantly impact the metal sites. These results validated the initial assumption that only metal location is adjusted in this work. This chapter will present the overall conclusions in line with the aim presented at the beginning of this thesis and recommendations for future work in this area.

In conclusion, Pt metal was successfully placed outside the MFI micropores using pre-synthesised Pt NPs capped in OCA. The capping agent was successfully removed using a cyclic oxidation and reduction pre-treatment with minimal sintering. Pt was also successfully placed mostly inside the MFI micropores using a competitive ion exchange technique which exchanged the MFI surface with Pt ions which were then reduced to give Pt clusters and NPs. To ensure metal location was isolated in this study, the Pt metal placed inside and outside the MFI micropores always achieved an average particle size between 1-2 nm using TEM and CO chemisorption characterisation techniques. Furthermore, the Pt metal loading was successfully kept above 0.8 wt. % as this ensured the metal sites were not rate limiting. CO chemisorption was also used to ensure that the capping agents were appropriately removed from the Pt NPs surface. The experimental testing conditions were kept consistent throughout this study including pressure, feed flow rates and all experimental equipment.

Through catalyst performance determination in hydrocracking, this study was able to show that placing metal inside and outside the micropores of MFI firstly, does not affect the suppression of secondary cracking in the presence of H_2O – as primary hydrocracking is achieved regardless of metal location. However, metal location does significantly affect the extent of secondary isomerisation where for example at 40 % conversion, **Pt-CIE/MFI** achieves ~90 % linear cracking products whereas, **Pt-NPs/MFI** achieves ~40 % (*Figure 6.6*). This results in an increase in selectivity toward linear cracking products of ~50 %, which has significant benefits in achieving very high cetane diesel products. The reason for the vast difference is because having the metal inside the micropores, firstly, provides a non-diffusion hindered steady supply of reactant molecules to encourage desorption of the primary cracked products and, secondly, the cracking/isomerisation steps need to occur inside the MFI micropores which is more likely with

internal metal. Comparing **Pt-CIE/MFI** to commercially available **Pt/H-Y** in the presence of H_2O; at ~30 % cracking yield, **Pt-CIE/MFI** produces ~70 % n-C_{12} products whereas, **Pt/H-Y** produces only ~11%. This is a ~60 % selectivity improvement from the industrially used catalyst at lower conversion. Furthermore, placing Pt NPs on NSs showed that even with thin NSs of 2 nm thickness, if the metal is placed outside, the hydrocracking products are just as branched as those from **PtNPs/MFI**.

Post-mortem TEM characterisation of the catalyst samples revealed that no significant changes to the Pt metal sites were seen after ~10 days of reaction under varying hydrocracking conditions, ensuring that metal location was the only parameter varied in the study.

For further work in this area, recommendations include:

- Further analysis of **Pt/MFI** and **Pt-CIE/MFI** catalysts with varying metal location in wax hydrocracking under the presence of H_2O to assess if the benefits hold when cracking larger reactant molecules.
- Research into a process scale-up would be the next step towards industrialisation of the process, as scale up may affect the hydrocracking activity and selectivity.

REFERENCES

AHUNBAY, M. G. K. 2011. Monte Carlo simulation of water adsorption in hydrophobic MFI zeolites with hydrophilic sites. *Langmuir,* 27**,** 4986-4993.

AL-DAHHAN, M. H., LARACHI, F., DUDUKOVIC, M. P. & LAURENT, A. 1997. High-Pressure Trickle-Bed Reactors: A Review. *Industrial & Engineering Chemistry Research,* 36**,** 3292-3314.

AN, K., ALAYOGLU, S., MUSSELWHITE, N., NA, K. & SOMORJAI, G. A. 2014. Designed Catalysts from Pt Nanoparticles Supported on Macroporous Oxides for Selective Isomerization of n-Hexane. *Journal of the American Chemical Society,* 136**,** 6830-6833.

BALS, S., KABIUS, B., HAIDER, M., RADMILOVIC, V. & KISIELOWSKI, C. 2004. Annular dark field imaging in a TEM. *Solid state communications,* 130**,** 675-680.

BENSON, J. E. & BOUDART, M. 1965. Hydrogen-oxygen titration method for the measurement of supported platinum surface areas. *Journal of Catalysis,* 4**,** 704-710.

BERGERET, G., GALLEZOT, P., ERTL, G., KNÖZINGER, H. & WEITKAMP, J. 1997. Handbook of heterogeneous catalysis. *VCH, Weinheim,* 2**,** 439.

BÖHRINGER, W., KOTSIOPOULOS, A., DE BOER, M., KNOTTENBELT, C. & FLETCHER, J. 2007. Selective Fischer-Tropsch wax hydrocracking–opportunity for improvement of overall gas-to-liquids processing. *Studies in surface science and catalysis,* 163**,** 345-365.

BÖNNEMANN, H. & RICHARDS, RYAN M. 2001. Nanoscopic Metal Particles − Synthetic Methods and Potential Applications. *European Journal of Inorganic Chemistry,* 2001**,** 2455-2480.

BOSS, C. B. & FREDEEN, K. J. 1999. *Concepts, instrumentation and techniques in inductively coupled plasma optical emission spectrometry*, Perkin Elmer Norwalk.

BOUCHY, C., HASTOY, G., GUILLON, E. & MARTENS, J. 2009. Fischer-Tropsch waxes upgrading via hydrocracking and selective hydroisomerization. *Oil & Gas Science and Technology-Revue de l'IFP,* 64**,** 91-112.

BOUDART, M. & DJÉGA-MARIADASSOU, G. 2014. *Kinetics of heterogeneous catalytic reactions*, Princeton University Press.

BOUTONNET, M., KIZLING, J., STENIUS, P. & MAIRE, G. 1982. The preparation of monodisperse colloidal metal particles from microemulsions. *Colloids and Surfaces,* 5**,** 209-225.

BROSIUS, R., KOOYMAN, P. J. & FLETCHER, J. C. Q. 2016. Selective Formation of Linear Alkanes from n-Hexadecane Primary Hydrocracking in Shape-Selective MFI Zeolites by Competitive Adsorption of Water. *ACS Catalysis***,** 7710-7715.

CHOI, M., NA, K., KIM, J., SAKAMOTO, Y., TERASAKI, O. & RYOO, R. 2009. Stable single-unit-cell nanosheets of zeolite MFI as active and long-lived catalysts. *Nature,* 461**,** 246-249.

CSICSERY, S. M. 1984. Shape-selective catalysis in zeolites. *Zeolites,* 4**,** 202-213.

DE HAAN, R., JOORST, G., MOKOENA, E. & NICOLAIDES, C. P. 2007. Non-sulfided nickel supported on silicated alumina as catalyst for the hydrocracking of n-hexadecane and of iron-based Fischer-Tropsch wax. *Applied Catalysis A: General,* 327**,** 247-254.

DRY, M. E. 2002. High quality diesel via the Fischer–Tropsch process – a review. *Journal of Chemical Technology & Biotechnology,* 77**,** 43-50.

FADONI, M. & LUCARELLI, L. 1999. Temperature programmed desorption, reduction, oxidation and flow chemisorption for the characterisation of heterogeneous catalysts. Theoretical aspects, instrumentation and applications. *Studies in Surface Science and Catalysis,* 120**,** 177-225.

FIÉVET, F. & BRAYNER, R. 2013. Nanomaterials: a danger or a promise? A chemical and biological perspective. Springer-Verlag, London.

FIEVET, F., LAGIER, J. & FIGLARZ, M. 1989. Preparing monodisperse metal powders in micrometer and submicrometer sizes by the polyol process. *Mrs Bulletin,* 14**,** 29-34.

GRANDVIEWRESEARCH 2015. Hydrocracking Market Analysis, Market Size, Application Analysis, Regional Outlook, Competitive Strategies, and Forecasts, 2015 To 2022.

HOU, X. & JONES, B. T. 2006. Inductively Coupled Plasma-Optical Emission Spectrometry. *Encyclopedia of Analytical Chemistry.* John Wiley & Sons, Ltd.

HUANG, W., KUHN, J. N., TSUNG, C.-K., ZHANG, Y., HABAS, S. E., YANG, P. & SOMORJAI, G. A. 2008. Dendrimer Templated Synthesis of One Nanometer Rh and Pt Particles Supported on Mesoporous Silica: Catalytic Activity for Ethylene and Pyrrole Hydrogenation. *Nano Letters,* 8**,** 2027-2034.

JACKSON, C. 2014. *Preparation and Characterisation of Pt-Ru/C Catalysts For Direct Methanol Fuel Cells.* Master of Science Degree, University of Cape Town.

JACOBS, P., FLANIGEN, E., JANSEN, J. & VAN BEKKUM, H. 2001. *Introduction to zeolite science and practice*, Elsevier.

JACQUIN, M., JONES, D. J., ROZIÈRE, J., LÓPEZ, A. J., RODRÍGUEZ-CASTELLÓN, E., TREJO MENAYO, J. M., LENARDA, M., STORARO, L., VACCARI, A. & ALBERTAZZI, S. 2004. Cetane improvement of diesel with a novel bimetallic catalyst. *Journal of Catalysis,* 228**,** 447-459.

KIM, J., KIM, W., SEO, Y., KIM, J.-C. & RYOO, R. 2013. n-Heptane hydroisomerization over Pt/MFI zeolite nanosheets: Effects of zeolite crystal thickness and platinum location. *Journal of Catalysis,* 301**,** 187-197.

KUHN, J. N., HUANG, W., TSUNG, C.-K., ZHANG, Y. & SOMORJAI, G. A. 2008. Structure Sensitivity of Carbon−Nitrogen Ring Opening: Impact of Platinum Particle Size from below 1 to 5 nm upon Pyrrole Hydrogenation Product Selectivity over Monodisperse Platinum Nanoparticles Loaded onto Mesoporous Silica. *Journal of the American Chemical Society,* 130**,** 14026-14027.

KUHN, J. N., TSUNG, C.-K., HUANG, W. & SOMORJAI, G. A. 2009. Effect of organic capping layers over monodisperse platinum nanoparticles upon activity for ethylene hydrogenation and carbon monoxide oxidation. *Journal of Catalysis,* 265**,** 209-215.

KUKARD, R. 2008. *The Effect of Zeolite Type on the Hydrocracking of Long n-Paraffins.* Master of Science, University of Cape Town.

KUNZ, S., MATURI, M. M., SCHRADER, I., BACKENKÖHLER, J., TSCHURL, M. & HEIZ, U. 2014. Same ligand – Different binding: A way to control the binding of N-acetyl-cysteine (NAC) to Pt clusters. *Journal of Colloid and Interface Science,* 426**,** 264-269.

LAMER, V. K. & DINEGAR, R. H. 1950. Theory, Production and Mechanism of Formation of Monodispersed Hydrosols. *Journal of the American Chemical Society,* 72**,** 4847-4854.

LE PAGE, A. J. F. 1988. *Applied Heterogeneous Catalysis,* Houston, Gulf Publishing Company.

LI, D., WANG, C., TRIPKOVIC, D., SUN, S., MARKOVIC, N. M. & STAMENKOVIC, V. R. 2012. Surfactant Removal for Colloidal Nanoparticles from Solution Synthesis: The Effect on Catalytic Performance. *ACS Catalysis,* 2**,** 1358-1362.

LI, Y. & SOMORJAI, G. A. 2010. Nanoscale advances in catalysis and energy applications. *Nano letters,* 10**,** 2289-2295.

LILIK, G. K. & BOEHMAN, A. L. 2011. Advanced Diesel Combustion of a High Cetane Number Fuel with Low Hydrocarbon and Carbon Monoxide Emissions. *Energy & Fuels,* 25**,** 1444-1456.

LIU, Z., SHAMSUZZOHA, M., ADA, E. T., REICHERT, W. M. & NIKLES, D. E. 2007. Synthesis and activation of Pt nanoparticles with controlled size for fuel cell electrocatalysts. *Journal of Power Sources,* 164**,** 472-480.

MCCLUNE, W. 1980. Powder diffraction file alphabetical index inorganic phase. *JCPDS, Swarthmore, PA*.

MEYERS, R. A. 2004. *Handbook of petroleum refining processes*, McGraw-Hill.

MURRAY, C. B., KAGAN, C. & BAWENDI, M. 2000. Synthesis and characterization of monodisperse nanocrystals and close-packed nanocrystal assemblies. *Annual Review of Materials Science,* 30**,** 545-610.

NIU, Z. & LI, Y. 2014. Removal and Utilization of Capping Agents in Nanocatalysis. *Chemistry of Materials,* 26**,** 72-83.

PACHÓN, L. D. & ROTHENBERG, G. 2008. Transition-metal nanoparticles: synthesis, stability and the leaching issue. *Applied Organometallic Chemistry,* 22**,** 288-299.

PHILIPPAERTS, A., PAULUSSEN, S., TURNER, S., LEBEDEV, O. I., VAN TENDELOO, G., POELMAN, H., BULUT, M., DE CLIPPEL, F., SMEETS, P. & SELS, B. 2010. Selectivity in sorption and hydrogenation of methyl oleate and elaidate on MFI zeolites. *Journal of catalysis,* 270**,** 172-184.

POMOGAILO, A. D. & DZHARDIMALIEVA, G. I. 2014. *Nanostructured materials preparation via condensation ways*, Springer.

RASTELLI, H., LOK, B., DUISMAN, J., EARLS, D. & MULLHAUPT, J. 1982. Characterization of zeolitic acidity I. The cracking of 2 mole% n-Butane over a fixed zeolite bed. *The Canadian Journal of Chemical Engineering,* 60**,** 44-49.

REISS, H. 1951. The growth of uniform colloidal dispersions. *The Journal of Chemical Physics,* 19**,** 482-487.

RESCHETILOWSKI, W., UNGER, B. & WENDLANDT, K.-P. 1989. Study of the ammonia–zeolite interaction in modified ZSM-5 by temperature-programmed desorption of ammonia. *Journal of the Chemical Society, Faraday Transactions 1: Physical Chemistry in Condensed Phases,* 85**,** 2941-2944.

RIOUX, R., SONG, H., HOEFELMEYER, J., YANG, P. & SOMORJAI, G. 2005. High-surface-area catalyst design: synthesis, characterization, and reaction studies of platinum nanoparticles in mesoporous SBA-15 silica. *The Journal of Physical Chemistry B,* 109**,** 2192-2202.

RIOUX, R. M. 2006. *The Synthesis, Characterization and Catalytic Reaction Studies of Monodisperse Platinum Nanoparticles in Mesoporous Oxide Materials.* ; Ernest Orlando Lawrence Berkeley NationalLaboratory, Berkeley, CA (US).

RIOUX, R. M., SONG, H., GRASS, M., HABAS, S., NIESZ, K., HOEFELMEYER, J. D., YANG, P. & SOMORJAI, G. A. 2006. Monodisperse platinum nanoparticles of well-defined shape: synthesis, characterization, catalytic properties and future prospects. *Topics in Catalysis,* 39**,** 167-174.

SCHERZER, J. & GRUIA, A. J. 1996. *Hydrocracking science and technology*, CRC Press.

SCHWARZ, J. A., CONTESCU, C. & CONTESCU, A. 1995. Methods for preparation of catalytic materials. *Chemical Reviews,* 95**,** 477-510.

SCOTT, R. W. J., WILSON, O. M. & CROOKS, R. M. 2005. Synthesis, Characterization, and Applications of Dendrimer-Encapsulated Nanoparticles. *The Journal of Physical Chemistry B,* 109**,** 692-704.

SEAH, M. P., BRIGGS, D. & SEAH, M. 1983. *Practical Surface Analysis: By Auger and X-ray Photoelectron Spectroscopy*, Wiley New York.

SONG, H., RIOUX, R. M., HOEFELMEYER, J. D., KOMOR, R., NIESZ, K., GRASS, M., YANG, P. & SOMORJAI, G. A. 2006. Hydrothermal Growth of Mesoporous SBA-15 Silica in the Presence of PVP-Stabilized Pt Nanoparticles: Synthesis, Characterization, and Catalytic Properties. *Journal of the American Chemical Society,* 128**,** 3027-3037.

van STEEN, E. 2014. Heterogeneous Catalysis - Basic Principles, Catalyst Synthesis and Characterisation, and Industrial Applications. Cape Town: University of Cape Town.

TAYLOR, S. M. 2013. *Oxygen reduction reaction on carbon supported dispersed platinum nanoparticles and extended platinum surfaces.* University of Cape Town.

TERANISHI, T., HOSOE, M., TANAKA, T. & MIYAKE, M. 1999. Size Control of Monodispersed Pt Nanoparticles and Their 2D Organization by Electrophoretic Deposition. *The Journal of Physical Chemistry B,* 103**,** 3818-3827.

THERMOFISCHERSCIENTIFIC. 2017. *The Scanning Transmission Electron Microscope* [Online]. Available: https://www.fei.com/introduction-to-electron-microscopy/stem/ [Accessed 13/09/2017].

THURIER, C. & DOPPELT, P. 2008. Platinum OMCVD processes and precursor chemistry. *Coordination Chemistry Reviews,* 252**,** 155-169.

VERHEYEN, E., JO, C., KURTTEPELI, M., VANBUTSELE, G., GOBECHIYA, E., KORÁNYI, T. I., BALS, S., VAN TENDELOO, G., RYOO, R. & KIRSCHHOCK, C. E. 2013. Molecular shape-

selectivity of MFI zeolite nanosheets in n-decane isomerization and hydrocracking. *Journal of Catalysis,* 300**,** 70-80.

VERMEIREN, W. & GILSON, J.-P. 2009. Impact of Zeolites on the Petroleum and Petrochemical Industry. *Topics in Catalysis,* 52**,** 1131-1161.

WAND, P., BARTL, J. D., HEIZ, U., TSCHURL, M. & COKOJA, M. 2016. Functionalization of small platinum nanoparticles with amines and phosphines: Ligand binding modes and particle stability. *Journal of Colloid and Interface Science,* 478**,** 72-80.

WANG, Y., REN, J., DENG, K., GUI, L. & TANG, Y. 2000. Preparation of Tractable Platinum, Rhodium, and Ruthenium Nanoclusters with Small Particle Size in Organic Media. *Chemistry of Materials,* 12**,** 1622-1627.

WEISSER, O. & LANDA, S. 2013. *Sulphide catalysts, their properties and applications*, Elsevier.

WEISZ, P. B. 1962. Polyfunctional Heterogeneous Catalysis. *Advances in Catalysis,* 13**,** 137-190.

WEITKAMP, J. 2012. Catalytic Hydrocracking—Mechanisms and Versatility of the Process. *ChemCatChem,* 4**,** 292-306.

WEITKAMP, J. & ERNST, S. 1990. Factors Influencing the Selectivity of Hydrocracking in Zeolites. *In:* BARTHOMEUF, D., DEROUANE, E. G. & HÖLDERICH, W. (eds.) *Guidelines for Mastering the Properties of Molecular Sieves: Relationship between the Physicochemical Properties of Zeolitic Systems and Their Low Dimensionality.* Boston, MA: Springer US.

WEITKAMP, J., JACOBS, P. A. & MARTENS, J. A. 1983. Isomerization and hydrocracking of C9 through C16 n-alkanes on Pt/HZSM-5 zeolite. *Applied Catalysis,* 8**,** 123-141.

WILLIAMS, D. B. & CARTER, C. B. 2009. The transmission electron microscope. *Transmission electron microscopy***,** 3-22.

WOOLERY, G., KUEHL, G., TIMKEN, H., CHESTER, A. & VARTULI, J. 1997. On the nature of framework Brønsted and Lewis acid sites in ZSM-5. *Zeolites,* 19**,** 288-296.

ZECEVIC, J., VANBUTSELE, G., DE JONG, K. P. & MARTENS, J. A. 2015. Nanoscale intimacy in bifunctional catalysts for selective conversion of hydrocarbons. *Nature,* 528**,** 245-248.

Appendix A

Experimental

A.1 Temperature Calibration between Oil Bath and Reacting Liquid

The temperature in the oil bath was measured against the actual temperature in the reaction vessel to calibrate for the correct temperature setting, as seen in *Figure A.1*.

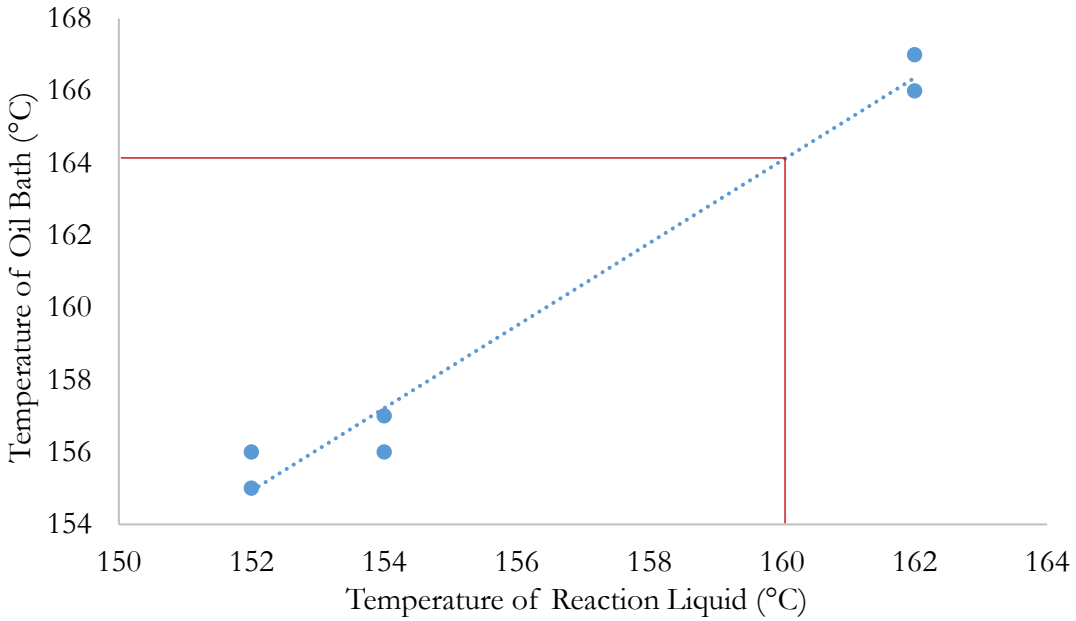

Figure A.1: Temperature calibration of heating mantle for Pt NP Synthesis

A.2 Image J

The free software is available for download at: https://imagej.en.softonic.com/ and requires an updated Java package.

The measuring tool was used along with the set scale function to record particle measurements. Cntrl-A opens an additional toolbox which was used to mark already measured particle diameters on the TEM image.

A.3 N-C_{16} RIG

A4.3.1 Reactor Temperature Profile

A temperature profile of the trickle bed reactors can be seen in *Figure A.2*.

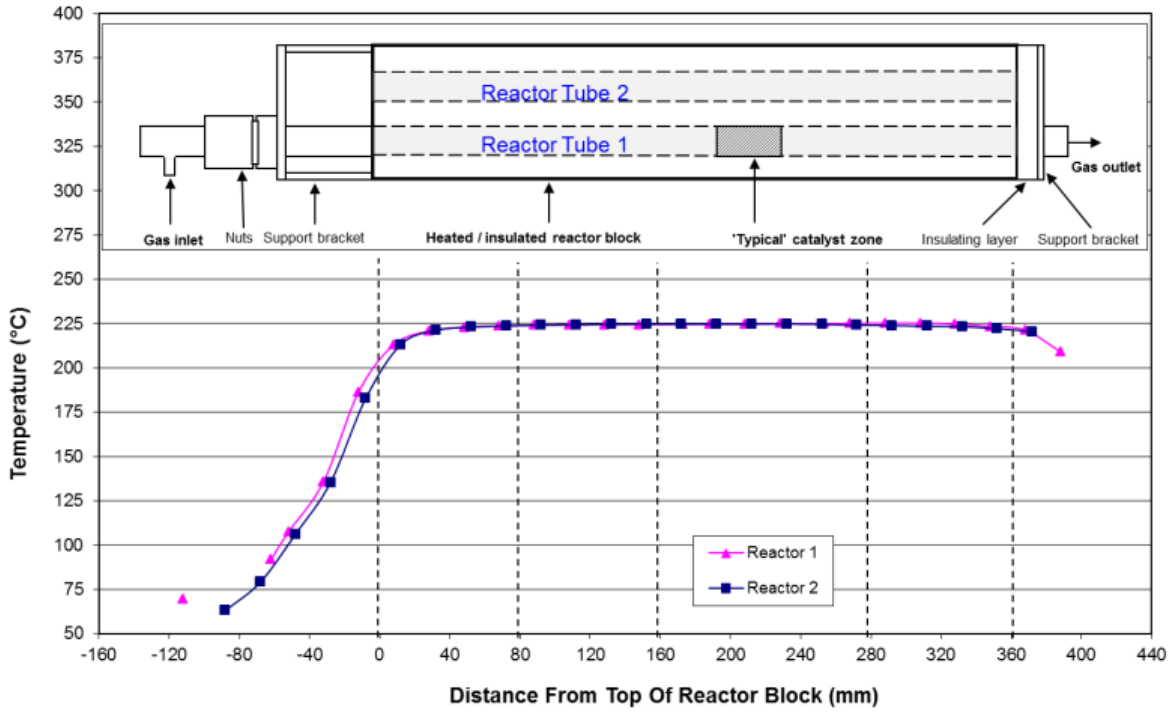

Figure A.2: Reactor temperature profile of n-C_{16} rig. Taken from Wynne et al., 2013.

A4.3.2 Centrifugation Limitation Calculation

The centrifugation limitation was calculated using Stokes' equation as follows:

$$v = \frac{d^2(p-L)\cdot g}{18\,n} = 1.14\text{E-}04 \text{ cm/hr}$$

Where,

d = 0.00000001 cm, p = 21.45 g/cm^3, L = 1.11 g/cm^3, g = 980 cm/s^2 x 47432000 (JA-20 maximum) and n = 0.169 g/cm.s.

Appendix B

Metal Preparation Results

B.1 Statistical Analysis for PtNPs/EG Samples

A statistical analysis is conducted to quantify the variability of the following samples beyond the visual representation, as shown in Table B.1: **PtNPs/EG**, **PtNPs/EG (repeat)** and, **PtNPs/EG (Wang *et al.*, 2000)**.

A "Z" Hypothesis Test was used to compare sample means with 300 data points in each set for differences beyond **x** nm. Through iteration, the smallest x-value was determined which allows for a passed hypothesis test – giving an indication of the variability of the synthesis procedure. A two-sided test was used as the synthesis methods were identical. The Wang *et al.*, 2000 data was extracted from the particle size distribution graph presented in the paper by using a random number generator to estimate the true sample values within the given intervals.

Table B.1: Statistical Analysis for PtNPs-EG Reproducibility

	PtNPs/EG	**PtNPs/EG (repeat)**	**PtNPs/EG (Wang *et al.*, 2000)**
Mean	1.70	1.53	1.36
Known variance	0.08	0.10	0.10
Observations	300	300	300
Hypothesis Test	PtNPs/EG and PtNPs/EG (repeat)		PtNPs/EG (repeat) and PtNPs/EG (Wang *et al.*, 2000)
Hypothesised mean difference	**x = 0.2**		**x = 0.2**
z	-1.11		-1.06
P (Z≤z) two tail	0.27		0.29
z Critical two tail	1.96		1.96

The first hypothesis test is between **PtNPs/EG** and **PtNPs/EG (repeat)**, which tests the means for a difference greater than x nm. It is seen that there is not a statistically significant difference ($z = -1.11$, $P < 0.27$) when $x \geq 0.2$ nm. It is therefore concluded that the synthesis methods produce similar particle sizes with a mean difference of 0.2 nm. The second hypothesis test is between **PtNPs/EG (repeat)** and **PtNPs/EG (Wang *et al.*, 2000)**. Using the same hypothesis test, it is found that there is not a statistically significant difference ($z = -1.06$, $P < 0.29$) when $x \geq 0.2$ nm. In conclusion, the synthesis methods compared have similar particle sizes with the means within 0.2 nm.

Appendix C

C.1 PtNPs/MFI Performance in n-C_{16} Hydrocracking

Throughout the research, several of the Pt NPs synthesised were investigated in n-C_{16} hydrocracking. These results are presented with the final aim of producing active, monodisperse Pt NPs of 1-2 nm supported on the outside of the MFI micropores.

C.1.1 Summary of Catalysts Tested

Table C.1: Summary of PtNPs/MFI Prepared Catalysts

Catalyst Name	Synthesis Method	Average Particle Diameter	Metal Loading (wt. %)
PtNPs-PVP/MFI	Pre-synthesised Pt NPs by colloidal chemistry	~9.78[1]	1.0
PtNPs-OCA/MFI	Pre-synthesised Pt NPs by colloidal chemistry	~1.25[1]	1.2
PtNPs-OMCVD/MFI	Organo-metallic chemical vapour deposition	1.57±0.42[2]	0.8

[1]CO chemisorption [2]TEM

C.1.2 Activity

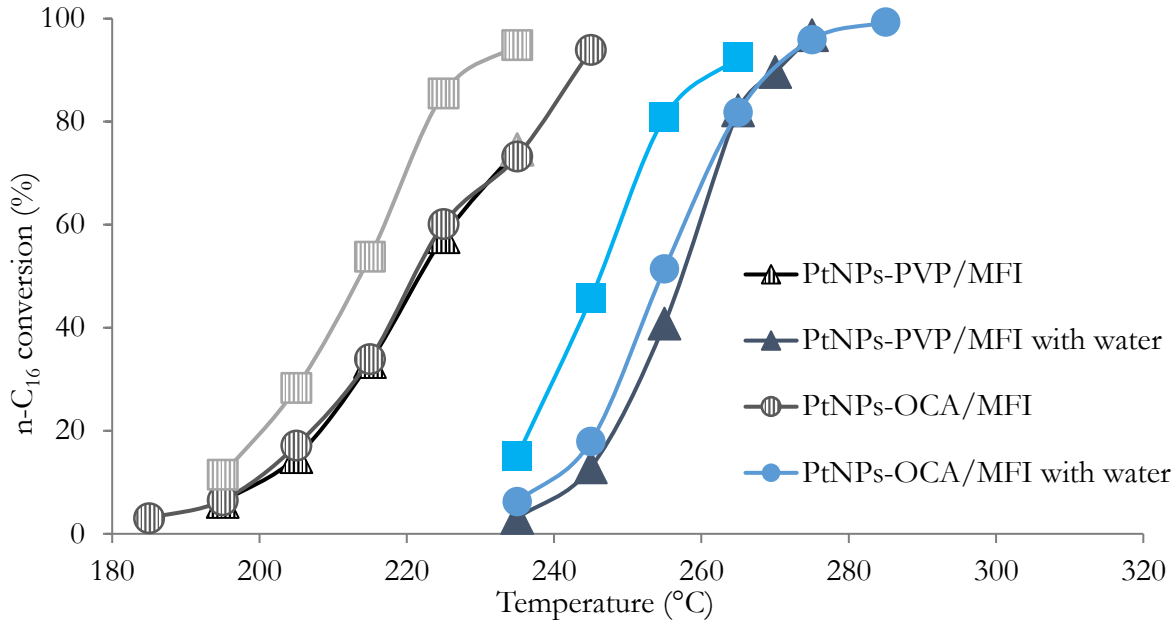

Figure C.1: *Light-off curves in the absence (grey) and presence (blue) of H_2O over PtNPs-PVP/MFI, PtNPs-OCA/MFI and, PtNPs-OMCVD/MFI.*

C.1.3 Achieving Primary Cracking

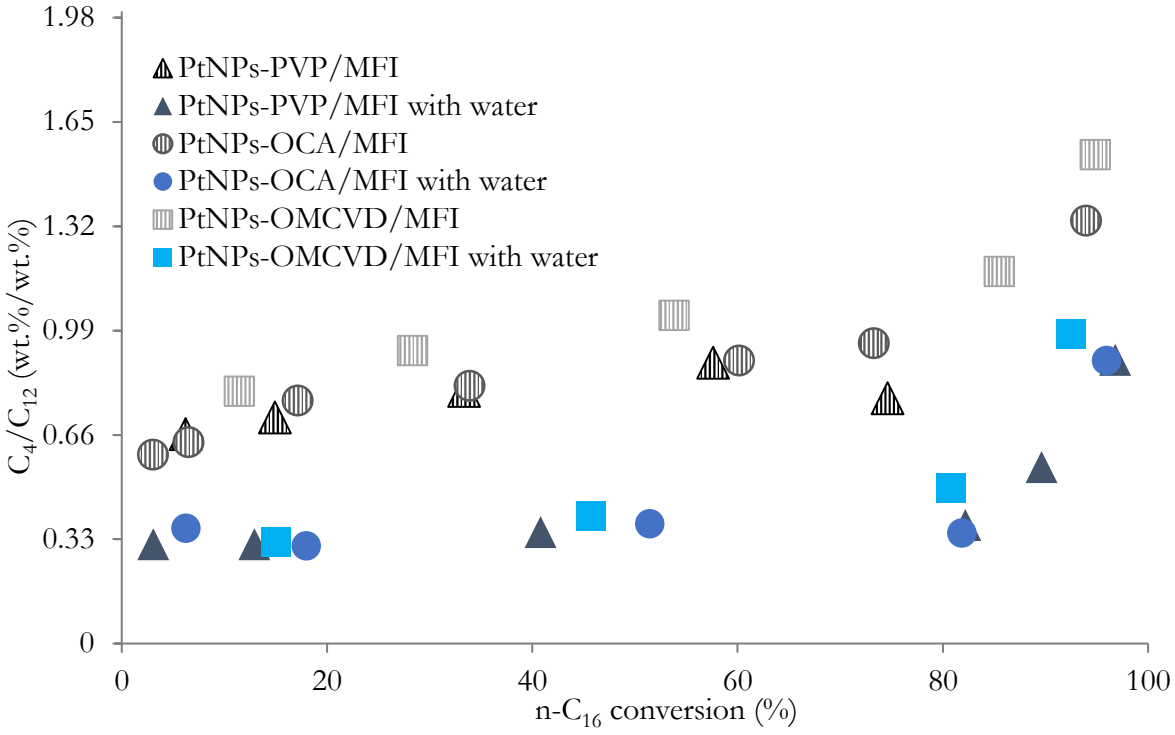

Figure C.2: Degree of secondary cracking in the absence (grey) and presence (blue) of H_2O over PtNPs-PVP/MFI, PtNPs-OCA/MFI and, PtNPs-OMCVD/MFI.

C.1.4 Secondary Isomerisation Selectivity

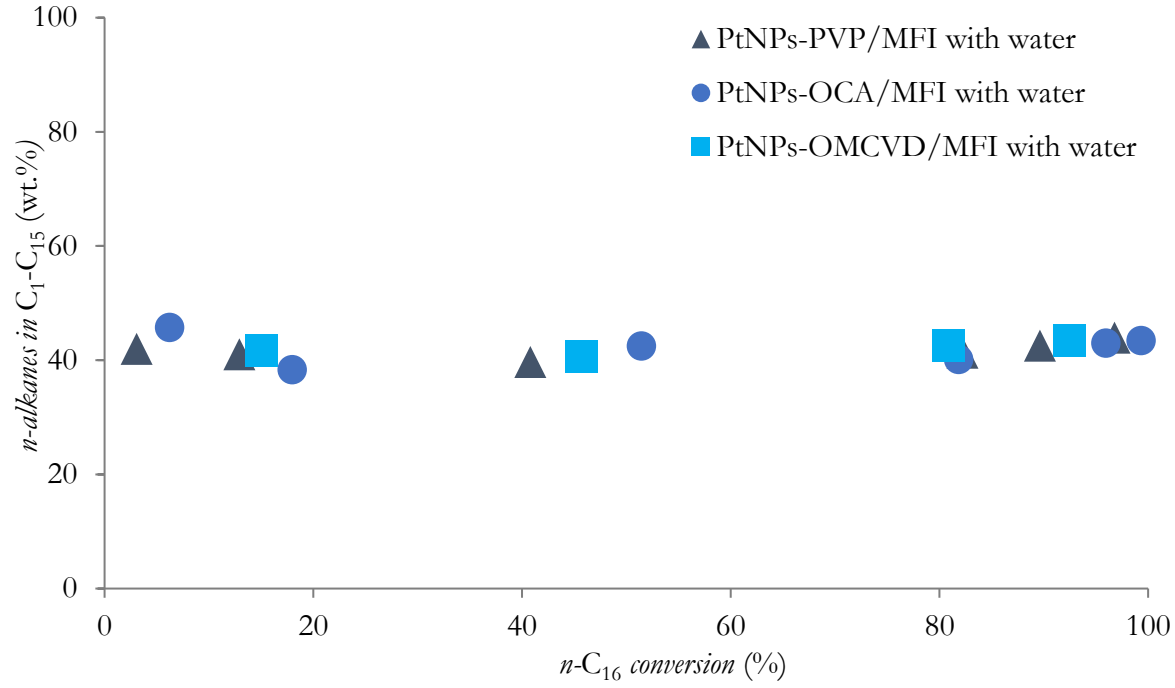

Figure C.3: Linearity of total product distribution of primary cracking in the presence of water for PtNPs-PVP/MFI, PtNPs-OCA/MFI and PtNPs-OMCVD/MFI.

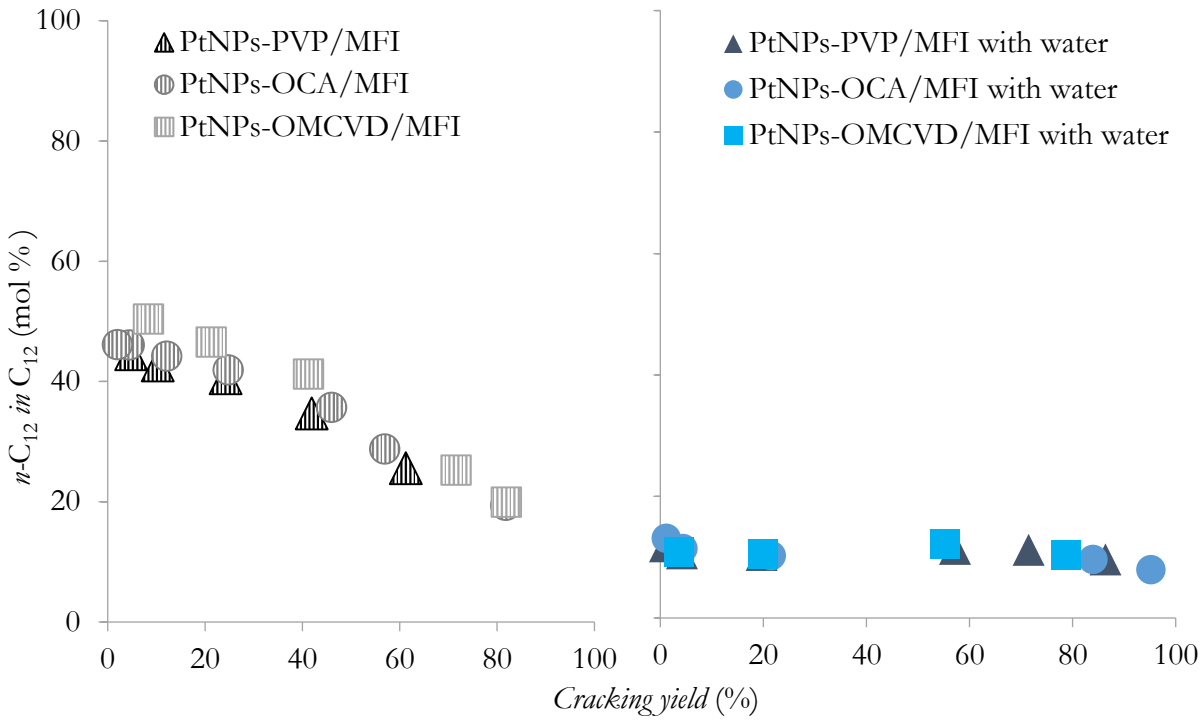

Figure C.4: Content of linear n-C_{12} in the C_{12} hydrocracking product fraction in the absence (grey) and presence (blue) of water over PtNPs-PVP/MFI, PtNPs-OCA/MFI and PtNPs-OMCVD/MFI.